

# Simulation Techniques benchmark, the test case of the November 11, 2019 Mw4.9 Le Teil earthquake



AUTHORS		REVIEW		APPROVAL	
Name	Date	Name	Date	Name	Date
<i>Elias El Haber, Chiara Smerzini, Marco Fasan, Ludivine Saint Mard, Manuela Vanini, Paola Traversa, Roberto Paolucci, Gabriele Ameri and Philippe Renault</i>	2021/10/13	Christophe MARTIN  Youssef BOZORGIA  	22/8/22	  Public-access <input checked="" type="checkbox"/> SIGMA-2 restricted <input type="checkbox"/>	

## Document history

DATE	VERSION	COMMENTS
2021/10/13	0	
2022/05/16	1	

## Executive summary

The prediction of earthquake ground motion to be expected for future earthquake scenarios is one of the key component in seismic hazard assessment. In particular, in low-to-moderate seismicity areas, ground motion recordings from earthquakes with magnitudes representative of the scenarios dominating the hazard at long return periods are rare or even absent. In these areas, the uncertainties associated with the ground motion predictions are high. Such uncertainties have a significant impact on the hazard estimates themselves, particularly for critical facilities, where the hazard is defined for longer return periods, and/or higher confidence intervals than ordinary buildings.

In recent years, the utilization of simulations to improve the understanding and the description of ground motion, particularly for magnitude-distance scenarios poorly sampled by recordings, has become a promising research area. As a matter of fact, hybrid ground motion models, constructed by integrating earthquake records with simulations, have gained popularity among the engineering seismology community (see for example many NGA-West2 models).

Physics-based simulation techniques (involving 3D Earth models), together with high-performance computing, have demonstrated to be reliable tools to assess both, median ground motion and associated variability (see for example Rodgers et al., 2019; Stupazzini et al., 2020). Within the SIGMA2 project, 3D-physics-based simulations were successfully applied to the 2016 Mw6.5 Norcia (Central Italy) earthquake (see deliverable SIGMA2-2018-D3-015), where permanent displacements provided by SAR measurements and the recorded waveforms available at accelerometric stations were simulated with satisfactory accuracy. Furthermore, in the same project, BB-SPEEDset, a dataset of broadband near-source ground motions from 3D physics-based simulations (see deliverable SIGMA2-2020-D3-051) has been constructed. BB-SPEEDset proved to provide peak values, integral ground motion parameters, features of impulsive ground motions and directionality effects, consistent on a statistical basis with near-source recordings (Paolucci et al. 2021b).

However, most of studies involving 3D physics-based simulations are carried out in high seismicity, densely instrumented areas, where the description of the seismic sources, as well as of the propagating medium is relatively exhaustive.

Several alternative ground motion simulation techniques exist. In the former SIGMA project, Empirical Green Function (EGF) based simulations were deployed (deliverable SIGMA-2013-D2-072). Although the technique was successfully applied to the Mw5.9 2012 Emilia Romagna earthquake (Northern Italy, see Dujardin et al., 2016), where simulated ground motion resulted remarkably consistent with observations, several questions still kept open at the end of the project, such as “how to select *the right EGF*”? Some limits of this technique were also pointed out, as the difficulty in simulating earthquakes with magnitudes 1 to 2 points larger than the magnitude of the EGF. On the other hand, the advantage of this technique is that independent description of the propagation medium is not necessary, since such information is carried by the Empirical Green’s Function itself.

EGF based-simulation techniques were then improved within the SINAPS@ research project founded by the French government, where the EGF technique was combined with extended rupture modeling (Dujardin et al., 2020).

The global aim of this project is to explore the potential of different ground motion simulation techniques in predicting ground motion in a low-to-moderate seismicity area, where the description of the seismic wave propagation medium is limited, the fault geometry and activity are poorly known and the earthquake records are rare.

To fulfill this objective, we take advantage of the November 11, 2019 Mw4.9 earthquake, occurred near Montélimar (South-East of France), a low seismicity region, to perform a benchmark on different ground motion simulation techniques. Four teams with different simulation techniques (3D Physics-Based, 1D Physics-Based, Empirical Green's Functions-based) took part in the exercise.

Besides quantitatively compare the performance of the different techniques in reproducing the ground motion produced by the 2019 earthquake, the objectives of the benchmark are:

- To explore the advantages and weaknesses of the different simulation techniques in low-to-moderate seismicity area context,
- To evaluate the benefit versus the cost (in terms of information needed) of performing 3D-physics-based simulations with respect to simpler techniques;
- To identify which ground motion features were realistically simulated, given the information available in such a low seismicity area.

Preliminary results highlight that EGF-based simulation techniques have the advantages that they do not need detailed information concerning the source-to-site propagation medium and the local site conditions to perform well at high frequencies with respect to PSB techniques. On the other hand, the applicability of EGF is constrained to the availability of high-quality recordings of small earthquakes, originated by the same target fault, at the target sites. For this reason, they are sensitive to local noise level, which prevents these techniques from providing realistic ground motion predictions at low frequencies (in the present case below 1 Hz).

On the contrary, 3D PBS techniques need large-scale and detailed geological and geophysical information on the propagating medium as well as of the shallow soil properties beneath the target sites, to construct and calibrate a 3D seismic wave propagation model. If source and wave propagation soil model are well-constrained, they can provide accurate predictions of ground motion at very low frequency, including static offsets on the fault and peak ground displacements, that are hardly retrieved from records because of the uncertainties associated with the post-processing procedures. Furthermore, physics-based approaches are suitable to provide spatially dense waveforms and site-specific ground shaking scenarios, accounting for the spatial variability of ground motions. The main disadvantages of these techniques is that they have a significant computational cost and they need to be combined with other ground motion evaluation methods to provide broad-band estimates.

Although very useful for sensitivity studies, particularly on the source, 1D physics-based simulation techniques appear too simplistic to provide realistic ground motion simulations in cases of a complex geology structure, as is the case of the area considered in the benchmark.

From this benchmark, it is found, from all techniques, that a well-constrained source model, with a sufficient level of complexity also at high frequencies, is fundamental to approach the recorded ground motion in a broadband sense, also for a moderate earthquake at 20-25 km distance.

The final aim of this work will be to provide recommendations on the use of simulation techniques in areas where limited information is available, on which information is essential to be collected, and accordingly to the amount of information collected, which ground motion feature will be realistically simulated.

Simulation Techniques benchmark, the test case of the November 11, 2019 Mw4.9 Le Teil earthquake

## Table of content

1	Introduction.....	10
2	Case study: Le Teil earthquake .....	12
2.1	Geographical and seismotectonics' context .....	12
2.2	Rupture mechanism of Le Teil earthquake .....	13
2.3	Scope of work and common assumptions.....	14
3	Empirical simulations.....	17
3.1	Irikura recipe .....	17
3.1.1	Methodology .....	17
3.1.2	Application to the Teil 2019 earthquake .....	20
3.1.3	Variability and uncertainty studies .....	25
3.1.4	Conclusion on Irikura recipe in low-to-moderate seismicity .....	28
3.2	Dujardin et al. (2020) modified method .....	29
3.2.1	Method overview.....	29
3.2.2	Application to Le Teil earthquake .....	31
3.2.3	Sensitivity study .....	36
3.2.4	Recap on Dujardin modified technique.....	44
4	Physics-based simulations .....	46
4.1	Finite fault 1D simulations .....	46
4.1.1	Source model.....	46
4.1.2	Wave propagation model.....	48
4.1.3	Variability from random simulations, results and discussion .....	50
4.2	3D simulations .....	56
4.2.1	The numerical code SPEED .....	56
4.2.2	Set up of a 3D model: basin shape and velocity model .....	59
4.2.3	Features of 3D numerical mesh model and computational features .....	62
4.2.4	Convergence tests in the high-frequency range.....	63
4.2.5	Verification analyses with Hisada code .....	64
4.2.6	1D and 3D point-source SPEED solutions .....	65
4.2.7	Finite-fault SPEED solutions with different slip distribution models .....	66
4.2.8	Overview of results .....	68
5	Simulation's methods and Ground motion variability .....	70
5.1	Comparison for different ground motion intensity measures.....	70
5.2	Advantages and disadvantages .....	75
6	Conclusions and perspectives .....	76
7	References .....	79
8	Appendixes.....	84
8.1	Appendix 1: Irikura recipe .....	84
8.2	Appendix 2: Dujardin modified method .....	90

8.3	Appendix 3: 3D simulations .....	91
8.4	Appendix 4: Comparison of simulation techniques between 0 and 10 Hz .....	94
8.5	Appendix 5: Comparison of simulations by using the slip distribution B (see section 3.2.2 for details) 96	

## List of figures

Figure 1: Seismotectonic map of the region where occurred the 11 November 2019 Mw 4.9 earthquake. The reverse-faulting focal mechanism is represented by the black and white circle. The red and purple circles are instrumental and historical seismicity, respectively; the yellow squares represent the Nuclear Power Plants in the region. The black lines are faults from the Aubenas geological map (Elmi et al., 1996) with the La Rouvière Fault (LRF) in red. CF Cévennes Fault, MF Marsanne Fault. The shaded DTM is from BD ALTI 25m (IGN); MC and AI in the inset are Massif Central and Alps, respectively. (Figure form Ritz et al., 2020)..... 12

Figure 2: Shear-wave velocity profile (black line indicates the best misfit profile, gray lines indicate the ensemble of inverted  $V_s$  profiles that explain dispersion data within their uncertainty bound) overlaying the geological cross-section modified from (Ritz et al., 2020) (licensed under CC BY 4.0.) (Figure 2 in Causse et al. 2021). ..... 13

Figure 3: The estimated static slip distribution over the rupture area without smoothing (upper plot) and with smoothing and tapering (lower plot) obtained from Cornou et al. (2020) and Causse et al. (2021) for the Le Teil earthquake. The red dot represents the estimated location of the hypocenter..... 14

Figure 4: Map of Le Teil area showing the slip model of the Le Teil earthquake (colorbar at the map's top left corner). The black dot refers to the epicenter location and the red triangles represent the five stations used in this study (Table 2). The blue and green dots represent the epicenter locations of the two aftershocks occurred on 13/11/2019 and 23/11/2019, respectively (the blue and black dots are almost overlapped). ..... 16

Figure 5: Division of the large fault into  $NL * NW$  subfaults associated with an EGF.  $\xi_{ij}$  is the distance from the rupture nucleation point to the (i,j)-th subfault,  $R_{ij}$  is the propagation distance and  $R_0$  is the EGF hypocentral distance. .... 17

Figure 6: Representation of fractal summation. Small subfaults (black squares) acceleration are summed up to obtain intermediate subfaults (red squares) and the process is repeated until we cover the entire fault. .... 18

Figure 7: Flowchart of source characterization following the Irikura recipe (HERP, 2017) ..... 19

Figure 8: Left figure: localization of asperities as Irikura recipe's input, from data slip distribution of  $k^2$ -model, inspired from inversion data of Cornou et al. (2020); right figure: representation of asperities in Irikura recipe code ..... 20

Figure 9: Checking the value of corner frequency and high-frequency filter (colored lines) at each station (A=ADHE, O=OGLP, C=CRU1, T=TRI2) for the Teil 2019 earthquake with the spectral ratio methodology for the three components (black lines). ..... 21

Figure 10: Checking the value of corner frequency and high-frequency filter (colored lines) at each station for the aftershock earthquake 23/11/2019 with the spectral ratio methodology for the three components (black lines). .... 22

Figure 11: GOF for PGA, FAS, PSA, AI and D595 at each station for the 3 components (NS : red points, EW : blue points, Z: green points) for both EGF 13/11/2019 and 23/11/2019. For the PSA and PGA, the GOF has been averaged over frequency broad range (1-25Hz). .... 24

Figure 12: GOF for PSA at 5 % damping for the 3 components depending on frequency averaged on all stations for both EGF. The grey area shows the validate frequency range for simulations (1-25 Hz).. 25

Figure 13 (a) Slip distribution from Cornou et al. (2020) (b) Slip distribution from Denovalis et al. (2020). Below figures are respectively each model enriched in high-frequency with  $k^2$ -model..... 26

Figure 14 Variability in Fourier Spectra due to input slip distribution variability ..... 26

Figure 15 Fourier amplitude spectra (m/s) for the 100 simulations (grey) with mean (black) compared to benchmark simulations (blue) and observed event (black) ..... 27

Figure 16 Variability study of 100 simulations on EGF parameters (blue points) and of 100 simulations on main event parameters (green points) on PGA, arias intensity and effective duration. Red points correspond to observe data and bar to mean and standard deviation..... 28

Figure 17: The frequency dependence of the Radiation Pattern Correction (RPC) function (Dujardin et al., 2020)..... 31

Figure 18: The signal over noise ratio (SNR) calculated for the two aftershocks' accelerograms recorded at five stations: ADHE in blue, CRU1 in red, TRI2 in green, OGLP in magenta and A192B in cyan.... 32

Figure 19: The static slip distribution (a) estimated by Cornou et al. (2020) and Causse et al. (2021) and (b) calculated using Eq. 3.2.4 (refer to text for details) with the corresponding moment rate amplitude (respectively, in (c) and (d)). The red dots in (a) and (b) correspond to the nucleation position on the fault. The theoretical  $\omega - 2$ spectra (Brune, 1970) computed for the medium value  $\Delta\sigma = 2.0$  MPa is represented by the red curves in (c) and (d). ..... 33

Figure 20: Comparison of the accelerograms simulated using the slip distribution estimated by Cornou et al. (2020) (in blue) and the slip distribution calculated as per Eq. 3.2.4 (in green; see text for more details) to the recorded acceleration (in red) for the three components of the five analyzed stations (ADHE, CRU1, OGLP, TRI2 and A192B)..... 34

Figure 21: The Fourier Amplitude Spectra of the accelerograms simulated using the slip distribution estimated by Cornou et al. (2020) (in blue) and the slip distribution calculated as per Eq. 3.2.4 (in green; see text for more details) and the accelerograms recorded in-situ (in red) for the three components of the five analyzed stations (ADHE, CRU1, OGLP, TRI2 and A192B). ..... 35

Figure 22: After filtering between 1 and 10 Hz, the comparison of the three ground motion intensity measures in the time domain (PGA, AI and Duration) calculated for the accelerograms simulated using the slip distribution estimated by Cornou et al. (2020) (in blue) and the slip distribution calculated as per Eq. 3.2.4 (in green; see text for more details) and the accelerograms recorded in-situ (in red) for the three components of the five analyzed stations (ADHE, CRU1, OGLP, TRI2 and A192B). ..... 36

Figure 23: The histograms of the random variables defining the source parameters of the target event: stress drop ( $\Delta\sigma$ ), rupture speed ( $V_{rup}$ ), the nucleation position on the rupture plan ( $X_{nuc}$ ,  $Y_{nuc}$ ). .... 37

Figure 24: Variability coefficient  $\alpha$  for the five ground motion intensity measures: PGA, Arias Intensity, Duration and FAS (from top to bottom) estimated for the five stations: ADHE, CRU1, OGLP, TRI2 and A192B by varying the source parameters of the target event. .... 39

Figure 25: The PGA, Arias Intensity and Duration obtained from the 100 simulations generated by varying at the same time: the stress drop, the rupture speed and the position of the nucleation on the rupture plan (for each GM intensity measure, a grey dot represents the output of one simulation, at one station and in one direction). The error bars correspond to the average  $\pm 1\sigma$  of the 100 simulations. The red dots correspond to the results of the recorded accelerograms for the Le Teil earthquake. .... 40

Figure 26: The Fourier Amplitude Spectra (FAS) calculated from the 100 simulations generated by varying at the same time: the stress drop, the rupture speed and the position of the nucleation on the rupture plan (each grey curve represents the output of one simulation, at one station and in one direction). The black curves correspond to the average  $\pm 1\sigma$  of the 100 simulations. The red curves correspond to the FAS of the recorded accelerograms for the Le Teil earthquake. .... 41

Figure 27: The static slip distribution (a) and the moment rate amplitude function (b) of the simulation that fits the best the results of the recorded accelerograms for the Le Teil earthquake. .... 42

Figure 28: The histograms of the random variables defining the EGF's properties: Magnitude ( $M_w$ ), stress drop ( $\Delta\sigma$ ), the strike and the dip. .... 43

Figure 29: By varying the EGF's properties, the variability coefficient  $\alpha$  for the five ground motion intensity measures: PGA, Arias Intensity, Duration and FAS estimated for the five stations: ADHE, CRU1, OGLP, TRI2 and A192B. .... 44

Figure 30: Simulated deterministic rupture process for the Le Teil event: a) Cornou LF, b) Cornou HF, c) DeNovellis LF, d) DeNovellis HF. The darker areas correspond to a high slip on the fault while the red dot shows the nucleation point of the rupture. The white isochrones describe the time evolution of the rupture process..... 48

Figure 31: structure adopted for CRU1 station: a) profile up to 5.5km, b) profile up to 0.5km ..... 49

Figure 32: structure adopted for OGLP station: a) profile up to 5.5km, b) profile up to 0.5km ..... 49

Figure 33: structure adopted for ADHE and TRI2 stations..... 50

Figure 34: PGA comparison. red dot represents the observed value, black dot the median from simulations, the two bars plus/minus one standard deviation, grey dots the values of each simulation ..... 51

Figure 35: Arias Intensity comparison. red dot represents the observed value, black dot the median from simulations, the two bars plus/minus one standard deviation, grey dots the values of each simulation ..... 52

Figure 36: Significant Duration (D5/95). red dot represents the observed value, black dot the median from simulations, the two bars plus/minus one standard deviation, grey dots the values of each simulation..... 52

Figure 37: Significant Duration (D7/70). red dot represents the observed value, black dot the median from simulations, the two bars plus/minus one standard deviation, grey dots the values of each simulation..... 53

Figure 38: GOF for spectral accelerations: the black line is the median value whereas the dashed lines represent the 16<sup>th</sup> and 84<sup>th</sup> percentiles (left NS component, right EW component) ..... 54

Figure 39: Workflow for 3D physics-based simulations using the SPEED code..... 57

Figure 40: View of the Rhône River Valley in the vicinity of the epicenter of the earthquake (red star) with indication of the extent of the SPEED model (see superimposed box). The location of recording stations (blue triangles) as well as the two nuclear power plants (Cruas and Tricastin, yellow squares) is shown..... 59

Figure 41: Basin model used in numerical simulations. The extent of the SPEED model is shown as a transparent yellow rectangle. Accelerometric stations of RESIF network are shown by blue triangles, yellow hexagons denote the NPPs of the area. The green dot near the epicenter is a site used for verification purposes (see section 4.2.6). Depth is measured with respect to the local topography. ... 60

Figure 42: Shear wave velocity profiles available at different sites along the Rhône River Valley. The implemented model, calibrated on the basis of OGLP and Tricastin NPP profiles, is shown in black. The crustal velocity model of Causse et al. (2020) is denoted by dashed brown line. Profiles at the border of the basin, at CRU1 and CRUAS site, to the north of the epicenter, are shown in dotted lines. .... 61

Figure 43: Numerical models built for simulations: ‘SPEED-1D’ model (left), ‘SPEED-3D model’ (right). ..... 62

Figure 44: Fourier amplitude spectra simulated for varying Spectral Degrees (SD from 1 to 5) at two positions at about 17 km from epicenter: on outcropping bedrock (to the North) and on soil (to the South), inside the basin..... 64

Figure 45: CRU1 station ( $R_{epi}=15$  km, top) and near field receiver ( $R_{epi}=1$  km, bottom). Simulated (and recorded, where available) velocity time histories and corresponding Fourier Amplitude spectra for EW component. Point source model. All time histories are low-pass filtered at 2 Hz. An exponential-type velocity slip function was used for this verification test, with a rise time of 1.2 s. .... 65

Figure 46: ADHE station ( $R_{epi}=18$  km). Simulated 1D and 3D and recorded velocity time histories, with corresponding Fourier Amplitude spectra. Point source model. All time histories are low-pass filtered at 2 Hz. .... 65

Figure 47: OGLP station ( $R_{epi}=24$  km). Simulated 1D and 3D and recorded velocity time histories, with corresponding Fourier Amplitude spectra. Point source model. All time histories are low-pass filtered at 2 Hz. .... 66

Figure 48: CRU1 station ( $R_{epi}=15$  km). Simulated 1D and 3D and recorded velocity time histories, with corresponding Fourier Amplitude spectra. Point source model. All time histories are low-pass filtered at 2 Hz. .... 66

Figure 49: Top: Slip distribution models used in the sensitivity tests. Slip is shown in meters. (a) Slip model from Cornou et al. (2021) and Causse et al. (2020). (b) Same as (a), improved in the High Frequency content (see Figure 3 of this deliverable); (c) Modified slip model from De Novellis et al. (2020), improved as well in the High Frequency range. Bottom: adopted slip function, in time and frequency domain, with a rise time of 0.5 s. .... 67

Figure 50: OGLP ( $R_{epi}=24$  km), CRU1 ( $R_{epi}=15$  km) and a near site station ( $R_{epi}=1$ km). Simulated and recorded (where available) EW velocity time histories, with corresponding Fourier amplitude spectra, for the different slip models of Figure 49: a) and b) for Cornou et al. and c) for De Novellis et al. models. All time histories have been low-passed filtered at 10 Hz. .... 68

Figure 51: Overview of the final 3D numerical model: view of basin structure, crustal layering and numerical fault (in red).....	68
Figure 52: PGA (top), PGV (middle) and PGD (bottom) maps from numerical simulation. Observations are shown with colored circles, in same palette. Le Teil earthquake fault (red rectangle) and epicenter (red star) are shown as well. (all data in maps are low-pass filtered at 10 Hz).....	69
Figure 53: The Fourier Amplitude Spectrum (FAS) of three-component (E: East-West; N: North-South; Z: Up-Down) unfiltered acceleration time histories calculated by the five different simulations (Irikura in black, Dujardin modified in cyan, PBS-1D in green and PBS-3D with finite fault in blue) and smoothed with the Konno and Ohmachi ( $b=40$ ; Konno and Ohmachi, 1998), at five stations (from top to bottom, ADHE, CRU1, OGLP, TRI2 and A192B). The red color corresponds to the recordings. ....	71
Figure 54: The ground motion intensity measures (PGA, PGV, Arias Intensity and Duration) calculated within a frequency range between 1 and 10 Hz, by using the five different simulations (Irikura in black, Dujardin modified in cyan, PBS-1D in green, PBS-3D with a point source in magenta and PBS-3D with finite fault in yellow) for the three components (E: East-West; N: North-South; Z: Up-Down), at five stations (ADHE, CRU1, OGLP, TRI2 and A192B). The red color corresponds to the recordings. ....	72

## List of tables

Table 1: General assumptions of the main rupture parameters of the Le Teil earthquake used by the several simulation's techniques.....	15
Table 2: Coordinates of the five stations used in this study and shown on Figure 4. ....	16
Table 3: Parameters for the benchmark EGFs.....	21
Table 4: Source parameters from Irikura recipe for the referenced scenario .....	23
Table 5: List of the two EGFs metadata used in the simulation of Le Teil earthquake. ....	31
Table 6: The source parameters of the simulation that fits the best the results of the recorded accelerograms for the Le Teil earthquake compared to the initial simulation of the benchmark. ....	41
Table 7: Main features of SPEED code for engineering seismology applications. ....	57
Table 8: List of simulation case studies, including validations of real earthquakes and scenario simulations, in Italy and in the rest of the world.....	58
Table 9: Crustal model. ....	61
Table 10: Parameters of the P- and S-wave velocity profiles of equation (4.2.1). ....	62
Table 11: Main computational features of the two numerical models adopted. ....	63
Table 12: Summary of performed simulations.....	63
Table 13: The Goodness of Fit (GoF) between simulated and recorded accelerograms filtered between 1 and 10 Hz and calculated for the five ground motion intensity measures (PGA, PGV, Arias Intensity, Duration and FAS) estimated by using the five simulation results. The results are sorted by station and by calculation direction. ....	73
Table 14: Comparison table between the different simulation's techniques. ....	75

## 1 Introduction

For years, earthquakes have been one of the deadliest natural hazards. Between 2000 and 2015, more than 800,000 people were killed worldwide due to earthquakes, according to the United States Geological Survey (USGS). This unavoidable risk arising from complex tectonic movement and ruptures in the Earth's crust (Reid, 1910) can cause significant economic and social losses especially in urbanized environments. Knowing that there is, currently, no possibility to predict short-term seismic events with precision in terms of location, magnitude and duration, seismic networks are installed all over the world (e.g., RESIF (France), RAN (Italy), COSMOS (San Francisco), RESORCE (Europe), Guerrero Accelerograph Network (Mexico)...) to better understand the physical processes associated to the rupture, the wave propagation in the ground, the site effects and the quantification of possible damages to structures. Thus, these recordings allowed the scientific community to concentrate efforts on the improvement of approaches and tools for the prediction of ground response during future earthquakes, with the ultimate goal of enhancing disaster risk reduction policies.

Since decades, based on recorded data collected in strong motion databases and on associated metadata, the engineering seismology community has developed an increasing number of ground motion prediction equations (GMPEs) that relate a ground motion parameter (e.g., PGV, PGA, response spectrum, Fourier Amplitude Spectrum) to a set of variables describing the source (earthquake magnitude, focal mechanism, fault geometry,...), the wave propagation through the medium and the site response (e.g. Douglas 2020). Most of these GMPEs are developed based on statistical analysis of recordings from active seismic regions and are not necessarily representative of the ground motion features observed in low-to-moderate activity regions. Indeed, earthquake recordings from moderate to large magnitude earthquake are very rare in these regions and it is now well established that dependency of ground motion on source and attenuation properties varies as a function of the regional context. Even in active regions, however, the amount of data available from earthquakes that typically dominates the seismic hazard of critical facilities (i.e., moderate to large magnitude events at short distances) is relatively limited and, therefore, GMPEs may be poorly constrained for those scenarios.

In this framework, the perspective of taking advantage of ground motion simulation techniques to improve the prediction of ground motion expected at a given site for future earthquake scenarios is very appealing. In the literature, there are different types of ground motion simulation approaches: stochastic techniques (e.g. Boore 2003), physics-based numerical simulations (Faccioli et al. 1997; Komatitsch and Vilotte 1998; Graves 1996, amongst others) and empirical/hybrid Green's function methods (Hartzell, 1978). Whatever the used technique, ground motion prediction is very sensitive to many aspects such as the earthquake source parameters, or the geophysical properties of the soil beneath at the considered site. Besides, the relevance and the performance of the different ground motion simulation techniques varies depending on the simulation configuration and on the degree of knowledge available about the whole wave propagation medium.

Mainland France is a country with a low-to-moderate seismic activity. Each year, while hundreds of small earthquakes with a magnitude smaller than 3 are recorded, only few events have a magnitude larger than 3.5. Over the period 1996-2019, the largest recorded earthquake had Mw5.0 (Traversa et al 2020). On the 11<sup>th</sup> of November 2019 (10h52 UTC), an earthquake with a local magnitude (ML) of 5.2 (RéNaSS) and a moment magnitude (Mw) of 4.9 (Cornou et al., 2021, Ritz et al., 2020) occurred in a low seismicity area of France, close to Montélimar's city. As such, the so-called Le Teil earthquake is one of the strongest earthquakes that occurred in the last decades in metropolitan France (Delouis et al., 2021). The earthquake rupture occurred on the Rouvière fault, which was not considered a potentially active fault (BDFA – Base de Données des Failles Potentiellement Actives – database, Jomard et al., 2017). Consequently, the occurrence of Le Teil earthquake was somehow surprising and also the characteristics of this earthquakes were peculiar: it was very shallow (about 1 km focal depth, e.g. Delouis et al., 2021) and produced a surface rupture with permanent displacement of about 10 to 15 cm. Moreover, the Le Teil earthquake presents another interesting feature: much fewer aftershocks than expected for an earthquake of magnitude Mw4.9 were recorded. Only two aftershocks with magnitude larger than 2.0 were recorded on the 13<sup>th</sup> and 23<sup>rd</sup> of November 2019.

The aim of this study is to carry out a benchmark exercise for earthquake ground-motion prediction with application to the Le Teil earthquake. Different research groups have participated to the benchmark to simulate ground motion on stations that recorded the main event and the aftershocks by using different simulation's techniques, namely, two empirical Green functions-based (EGF) techniques, one 1D physics-based simulation (PBS) method and one 3D PBS method. The expected outcome from this benchmark is a better understanding of the advantages and limitations of different techniques and awareness of the minimum level of input information necessary for each approach, with particular reference to low-to-moderate seismicity regions like France.

Besides comparing the ground motion intensity measures obtained from the different approaches and estimating the uncertainty due the choice of the simulation technique, several sensitivity studies were done with the different techniques to identify the input parameters controlling the most the ground motion on surface and, thus, provide insights into the key factors of the epistemic uncertainty in ground shaking prediction.

## 2 Case study: Le Teil earthquake

### 2.1 Geographical and seismotectonics' context

In the southeastern of France, an earthquake of magnitude 4.9 (Mw) occurred on the 11<sup>th</sup> of November 2019. It took place in a low-to moderate seismicity area within the lower Rhône river valley, close to Montélimar's city, an industrial region that hosts several operating nuclear power plants (Figure 1). Despite its moderate magnitude, the earthquake caused damages to residential buildings, the maximum macroseismic intensities reported in the epicentral area are between VII and VIII EMS-98 (Sira et al., 2020).

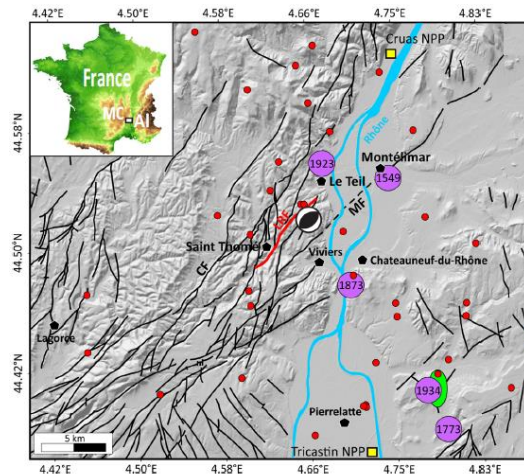


*Figure 1: Seismotectonic map of the region where occurred the 11 November 2019 Mw 4.9 earthquake. The reverse-faulting focal mechanism is represented by the black and white circle. The red and purple circles are instrumental and historical seismicity, respectively; the yellow squares represent the Nuclear Power Plants in the region. The black lines are faults from the Aubenais geological map (Elmi et al., 1996) with the La Rouvière Fault (LRF) in red. CF Cévennes Fault, MF Marsanne Fault. The shaded DTM is from BD ALTI 25m (IGN); MC and Al in the inset are Massif Central and Alps, respectively. (Figure form Ritz et al., 2020)*

The sector where the Teil earthquake occurred is located at the border of the Massif Central (MC) and the Alps (Al) (Figure 1). Its geological history is marked by at least four major deformation phases since 200 million years (Ma), responsible for the creation and reactivation of numerous faults, and other folding structures (Delouis et al., 2019).

Satellite radar interferometry images (InSAR) reveal a rupture zone along a fault listed on the geological map of Aubenais as the Rouvière fault (red line in Figure 1). This fault with a NE-SW orientation is part of the St Thomé-La Rouvière fault system located in the Cévennes fault system which marks the south-eastern edge of the Massif Central over nearly 150 km long (Delouis et al., 2019).

The Rouvière fault has a direction N030 to N050 (Figure 1). It is mapped as a fault about 8 km long dipping steeply to the SE (Elmi et al., 1996). To the south, it is intercepted by the Valgayette fault. Its northern part is more complex: it is intercepted perpendicularly by small NW-SE faults and converges with the Bayne-Roche Renard fault.

According to the BDFA (Base de Données des Failles Potentiellement Actives –Database of Potentially Active Faults) (Jomard et al., 2017), the Rouvière fault was not considered a potentially active fault, contrary to the two parallel faults oriented NE-SW and located at distance of 2.5 Km on both sides of the Rouvière fault: the St Rémèze fault on the North West (one of the segments of the Cévennes fault) and the Marsanne fault on the South-East.. Moreover, the central segment of the Marsanne fault is indicated as being active in the Quaternary on the basis of a geographical alignment of microearthquakes.

In addition, the area's geological settings (Elmi et al., 1996) and the deep boreholes in the region (see the geological logs numbered BSS002ARWX, BSS002ASXR and BSS002ASEZ and available in <http://infoterre.brgm.fr>) show a peculiar ground velocity profile. As shown in Figure 2, the analysis of seismic noise recorded at temporary stations deployed in the fault vicinity after the earthquake, shows a 1.2 km thick layer with increasing stiffness material overlaying a deposit with lower stiffness (Causse et al., 2021).

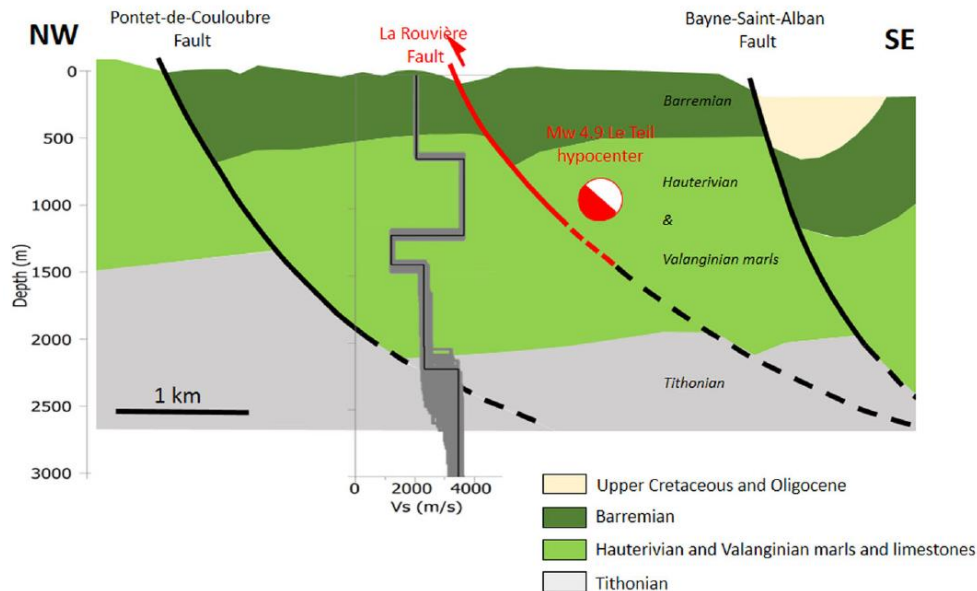


Figure 2: Shear-wave velocity profile (black line indicates the best misfit profile, gray lines indicate the ensemble of inverted  $V_s$  profiles that explain dispersion data within their uncertainty bound) overlaying the geological cross-section modified from (Ritz et al., 2020) (licensed under CC BY 4.0.) (Figure 2 in Causse et al. 2021).

## 2.2 Rupture mechanism of Le Teil earthquake

Many studies (Delouis et al., 2019, Cornou et al., 2021, Ritz et al., 2020, De Novellis et al., 2020, Mordret et al., 2020) analyzed the source of the Le Teil earthquake emerging to a detailed picture of the seismic rupture. The rupture area was very shallow, with a length of ~5km and a width of 1.75 km. The rupture reached the surface, with up to 15 cm of uplift of the SE side of the fault (Delouis et al., 2021). The slip distribution on the rupture plane has been estimated (Cornou et al., 2020; Causse et al., 2021). Based on the analysis of the permanent network records, the mainshock hypocenter was located NW of the La Rouvière fault trace (Delouis et al., 2019 and Cornou et al., 2021, Delouis et al., 2021) at a depth in the range of 1–1.5 km.

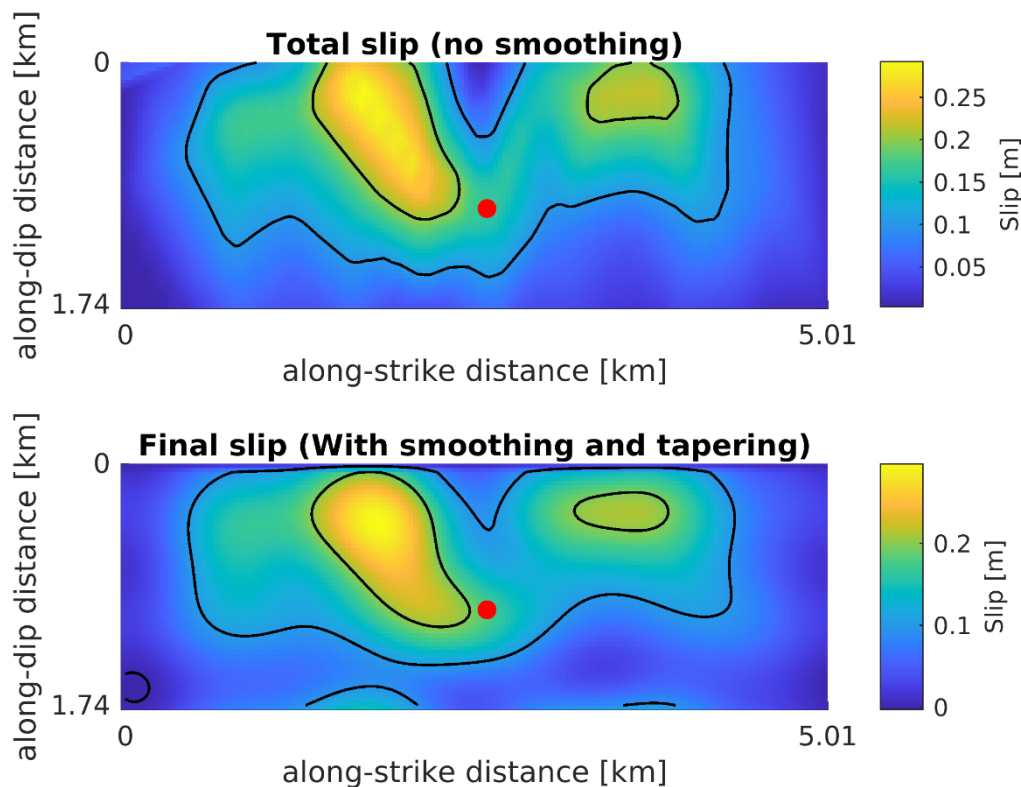


Figure 3: The estimated static slip distribution over the rupture area without smoothing (upper plot) and with smoothing and tapering (lower plot) obtained from Cornou et al. (2020) and Causse et al. (2021) for the Le Teil earthquake. The red dot represents the estimated location of the hypocenter.

Figure 3 shows the slip distribution estimated over the rupture area of the Le Teil earthquake and used in this study.

Ritz et al. (2020) used the FMNEAR method (Delouis, 2014) based on strong records' waveform inversion to determine the rupture mechanism. The retrieved solutions show a strike and a dip varying, respectively, between  $45^\circ$  and  $65^\circ$  and between  $45^\circ$  and  $50^\circ$ . The best obtained solution corresponds to strike, dip and rake equal to  $50^\circ$ ,  $58^\circ$  and  $89^\circ$ .

Knowing the hypocenter position, the duration and the dimension of the rupture, the average velocity rupture ( $V_r$ ) was estimated equal to 1800 m/s (Causse et al., 2021). It is between 50-90% of the shear wave velocity (see 1D velocity profile in Figure 2).

The stress drop that corresponds to the difference in shear stress acting on the fault plane before and after the earthquake, was estimated from the slip models resulting from InSAR data (Delouis et al., 2019). Its average value calculated from the available slip models is of the order of 2 MPa ( $2 \times 10^6$  Pa, or 20 bars). Locally, it can reach a maximum value of 4 to 5 MPa (40 to 50 bars). These are fairly standard values for earthquakes.

### 2.3 Scope of work and common assumptions

In this study, four different simulation methods (two empirical and two physics-based techniques) are used to reproduce the 11<sup>th</sup> of November earthquake occurred in Le Teil region. The aim of this study is to compare the performance of the different simulation techniques in a low-to-moderate seismicity region by quantifying the uncertainty related to each method and its input parameters. Finally, the different methods' advantages and disadvantages are discussed.

The four simulation's techniques are:

Simulation Techniques benchmark, the test case of the November 11, 2019 Mw4.9 Le Teil earthquake

- Empirical Green function based: The Irikura recipe
- Empirical Green function based: The Dujardin modified technique (Dujardin et al., 2020)
- 1D physics-based simulation
- 3D physics-based simulation

Referring to the physics-based simulation approaches, 1D and 3D nature concerns the type of modeling of the soil propagation medium: 1D, i.e. for horizontally-layered soil media, Vs 3D, i.e. for arbitrarily heterogeneous and complex media, including geological irregularities such as valleys.

In order to have a consistent comparison, common assumptions were fixed among the different simulation techniques, as summarized in Table 1. The specific assumptions for each calculation method will be defined in the sections dedicated to the methods' presentation (see sections 3 and 4).

*Table 1: General assumptions of the main rupture parameters of the Le Teil earthquake used by the several simulation's techniques.*

Rupture Parameters	Values
Earthquake magnitude	4.9 (Mw)
Epicenter location	4.6688°, 44.5208°
Hypocenter depth	1 Km
Rupture dimensions	5 x 1.75 Km <sup>2</sup>
Strike	50°
Dip	58°
Rake	89°
Stress drop	2 MPa
Rupture velocity (V <sub>r</sub> )	1800 m/s
Anelastic attenuation parameters (Q <sub>0</sub> and α)	Q <sub>0</sub> = 347 ± 4 α = 0.31 ± 0.005
Geometric spreading parameter (β)	1.02 ± 0.02

For the four techniques, the ground motion is simulated at five stations shown in Figure 4. These stations recorded both the mainshock and the two largest aftershocks. These stations are part of the RESIF network (Réseau Sismologique et géodésique Français; RESIF, 1995) and the AlpArray Seismic Network; (2015). With only 6 Km distance from the rupture zone, the station A192B is the closest station analyzed in this study. However, the recordings were clipped at this station. CRU1 station is located approximately 15Km from the rupture in the northeastern direction and the three remaining stations (ADHE, TRI2 and OGLP) are 15 to 25 Km away from the rupture zone, in the south/southeast direction. Due to this small range of distances, we do not expect to have a major contribution of anelastic attenuation to the results and thus, the corresponding parameters in Table 1 may have insignificant impact in this study.

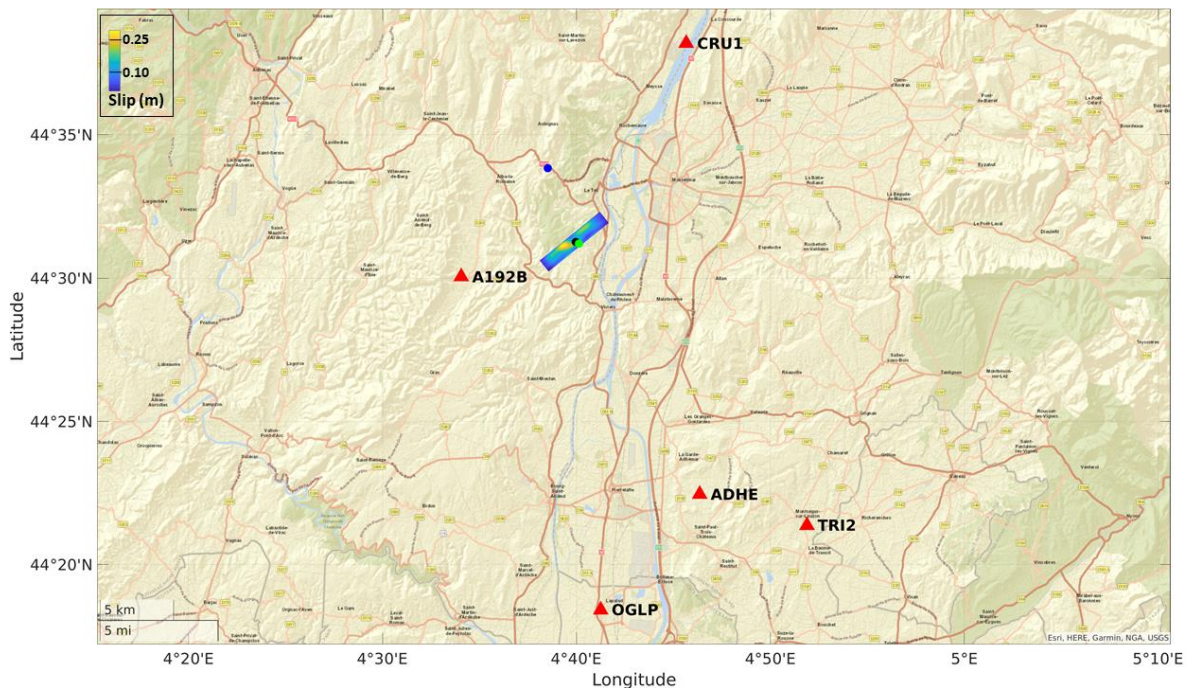


Figure 4: Map of Le Teil area showing the slip model of the Le Teil earthquake (colorbar at the map's top left corner). The black dot refers to the epicenter location and the red triangles represent the five stations used in this study (Table 2). The blue and green dots represent the epicenter locations of the two aftershocks occurred on 13/11/2019 and 23/11/2019, respectively (the blue and black dots are almost overlapped).

The simulated ground motions at these five stations will be analyzed in both, the time and the frequency domains by using different ground motion parameters: Arias Intensity (AI), Ground Motion Duration (DAI or D95), Peak Ground Acceleration (PGA) and Fourier amplitude spectrum (FAS). All the simulated

Table 2: Coordinates of the five stations used in this study and shown on Figure 4.

STATION	LAT	Lon	ELEVATION	Vs30 (m/s)	Type	Installation conditions
ADHE	44.37408	4.76974	90	~2000	High gain seismometer	Free field
CRU1	44.636253	4.758796	77	662	High gain seismometer	Free field
TRI2	44.3561	4.8572	141.2		High gain seismometer	Structure related
OGLP	44.307	4.689	46	490	Accelerometer	Free field
A192B	44.5006	4.57526	179		High gain seismometer	Structure related

To compare simulated and recorded accelerograms, the Goodness of Fit ( $GoF$ ) is calculated as follows:

$$GoF = \log_{10} \left( \frac{Simulated}{Recorded} \right) \quad Eq. 2.1.1$$

Note that a  $GoF$  equal to 0 means excellent agreement between the values and the scale is symmetric around the target value of 0. For the frequency domain parameters, the calculated  $GoF$  corresponds to the average of the values estimated within the analyzed frequency range.

### 3 Empirical simulations

#### 3.1 Irikura recipe

##### 3.1.1 Methodology

The Irikura recipe (Irikura and Miyake, 2011) is a strong ground motion methodology mainly developed and used in Japan, which is based on a kinematic description of the source. The specificity of this methodology compared to other kinematic simulation remained in the way to (1) sum up small events in order to obtain a larger event (2) characterize the source using asperities to represent source heterogeneity in slip distribution.

##### 3.1.1.1 Summation of EGF

The usual approach to produce a strong ground motion from an extended fault is to use a recorded small event called Empirical Green's Function (EGF). Indeed, a fault can be discretized in several point-sources spatially distributed (Hartzell, 1978). If we consider a short time function to be assimilated to a temporal Dirac, the signal represents the impulse response of a traversed medium: the Green function can therefore be represented by this small event.

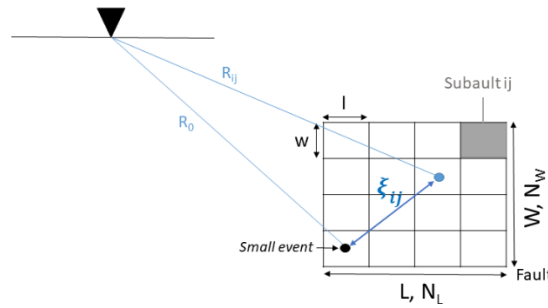


Figure 5: Division of the large fault into  $N_L * N_W$  subfaults associated with an EGF.  $\xi_{ij}$  is the distance from the rupture nucleation point to the  $(i,j)$ -th subfault,  $R_{ij}$  is the propagation distance and  $R_0$  is the EGF hypocentral distance.

The similarity assumption (i.e a small and a large earthquake are fundamentally similar, [Aki, 1967]) allows to assume that the radiation released by the large source is a superposition of the radiation of smaller sources. In the Irikura recipe, the number of summations is deduced directly from the similarity assumption, developed by Kanamori and Anderson (1975), considering that the dimensions' ratio between the large and the small event are a constant:

$$\frac{L}{l} = \frac{W}{w} = \frac{T}{\tau} = \left( \frac{M_0}{C_{sd} \cdot m_0} \right)^{1/3} = N \quad \text{Eq. 3.1.1}$$

where capital letters are parameters for the large fault, and lower letters for the subfault.  $L$  and  $l$  are length,  $W$  and  $w$  are width,  $T$  and  $\tau$  are rising time,  $M_0$  and  $m_0$  are seismic moment, and  $C_{sd}$  is the ratio of stress drop between the large and the small event.  $N$  is an integer number which represents the number of summation to realize in order to obtain the large seismic moment from the small seismic moment, according to the length  $N_L$ , the width  $N_w$ , and the dislocation  $N_D$ .

Based on early work of Hartzell (1978), we consider that the acceleration produced by a large event is the summation of accelerations from smaller events, convoluted with a slip velocity function [a box-car

function according to Haskell (1964) dislocation model] in order to account for rupture propagation delay  $t_{ij}$  and dislocation delay  $t_k$  on the fault.

$$A(t) = \sum_{i=1}^{N_W} \sum_{j=1}^{N_L} \sum_{k=1}^{N_D} a \left( t - \left( \frac{r_{ij}}{\beta} + \frac{\xi_{ij}}{V_r} \right) - \left( \frac{(k-1)T}{N_D} \right) \right) \quad \text{Eq. 3.1.2}$$

where  $\xi_{ij}$  is the distance from the rupture nucleation point to the (i,j)-th subfault,  $r_{ij}$  is the distance separating the small event nucleation point to the (i,j)-th subfault,  $V_r$  is the rupture velocity,  $\beta$  is the shear-wave velocity and  $T$  the rise time of main event. The Japanese institution Headquarters for Earthquake Research Promotion (HERP,2017) recipe considers that fault's rise time is proportional to the ratio of fault's width with rupture velocity, based on dynamic simulation results conducted by Day (1982):

$$T = \alpha \frac{W}{V_r} \quad \text{Eq. 3.1.3}$$

with  $\alpha$  a coefficient between 0.25 and 0.5 depending on the amount of heterogeneity in the slip model.

The reference technique of summation of Green functions of Irikura (1983) includes two limitations: artificial periodicity and a hole in intermediate-frequency range. Indeed, Irikura (1986) pointed out the problem to use a uniform time shift: it provokes an artificial periodicity of  $T/N_D$  in time domain, which has for consequence the appearance of secondary peaks in frequency domain. Therefore, Irikura (1986) introduced an integer  $n'$  in order to shift the periodicity to higher frequency range, which is outside from our range of interest. The difficulty of this solution is the under estimation of high frequency. Hence, the summation synthesis is divided into two terms: one for low-frequency and one for high-frequency, so the scaling law is respected for both frequency ranges. Also, later Irikura et al. (1997) improved the slip velocity function from a box car function to an exponential decaying function to obtain a smoother spectrum in the intermediate-frequency range.

$$A(t) = \sum_{i=1}^{N_W} \sum_{j=1}^{N_L} a_{ij}(t - t_{ij}) + \frac{1}{n'(1 - \exp(-1))} \sum_{i=1}^{N_W} \sum_{j=1}^{N_L} \sum_{k=1}^{(N_D-1)n'} \exp\left(-\frac{k-1}{(N_D-1)}\right) a_{ij} \left( t - t_{ij} - \frac{(k-1)T}{(N_D-1)n'} \right) \quad \text{Eq. 3.1.4}$$

Moreover, it appears that a gap in the energy content appears in the intermediate-frequency range with an increasing subfaults number. To overcome this issue, we developed a fractal summation: rather than performing one single summation following the similarity relation between the large event and the EGF, we sum up small events with intermediate subfaults, following the similarity relation between the intermediate subfaults and the small event.

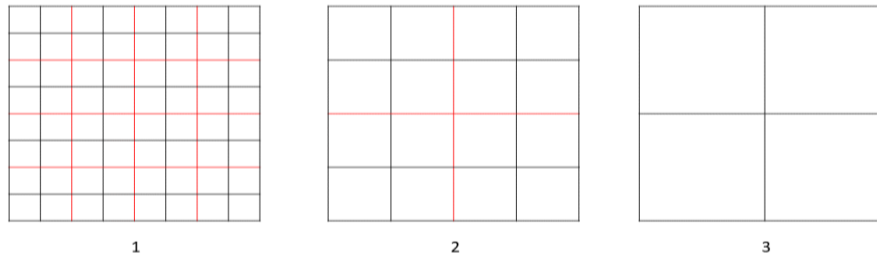


Figure 6: Representation of fractal summation. Small subfaults (black squares) acceleration are summed up to obtain intermediate subfaults (red squares) and the process is repeated until we cover the entire fault.

### 3.1.1.2 Source characterization

With the recent records of strong ground motions -such as 2000 Tottori, 2004 Niigata Chuetsu and 2007 Niigata-ken Chuetsu-Oki etc.- seismologists have been able to characterize the source using waveform inversion. They concluded that (1) within the fault plane there are areas where the slip is larger than the overall average slip; these areas are called asperities (Somerville et al. 1999) (2) asperity areas produce higher stress release compared to the average stress drop (Miyake et al. 2001, 2003) (3) asperity areas correspond to areas that generate strong ground motion (Miyake et al. 2001, 2003). In order to represent in a realistic way the simulated ground motion, variable stress drop need to be considered over the source.

In the Irikura recipe, we introduce a parameter referenced as “inner parameter” which defines the slip heterogeneity by characterizing the total asperity surface, asperity stress drop *etc.* Therefore, the source is decomposed in subfault which are identified as either background or asperity. Somerville et al. (1999) found that asperity parameters scale with the total seismic moment, just as the entire fault. Hence, they determine the scaling relation between the total asperity area and the seismic moment. Based on this scaling relation and on multiple-asperity model –which is an extension of single-asperity model given by Das and Kostrov (1986)– Irikura and Miyake (2011) proposed a recipe to determine asperity parameters, which is illustrated in the following flowchart. The single-asperity model is the general methodology to determine asperity and background parameters. If there are several asperities, then parameters of each asperity are determined from results of the single-asperity model.

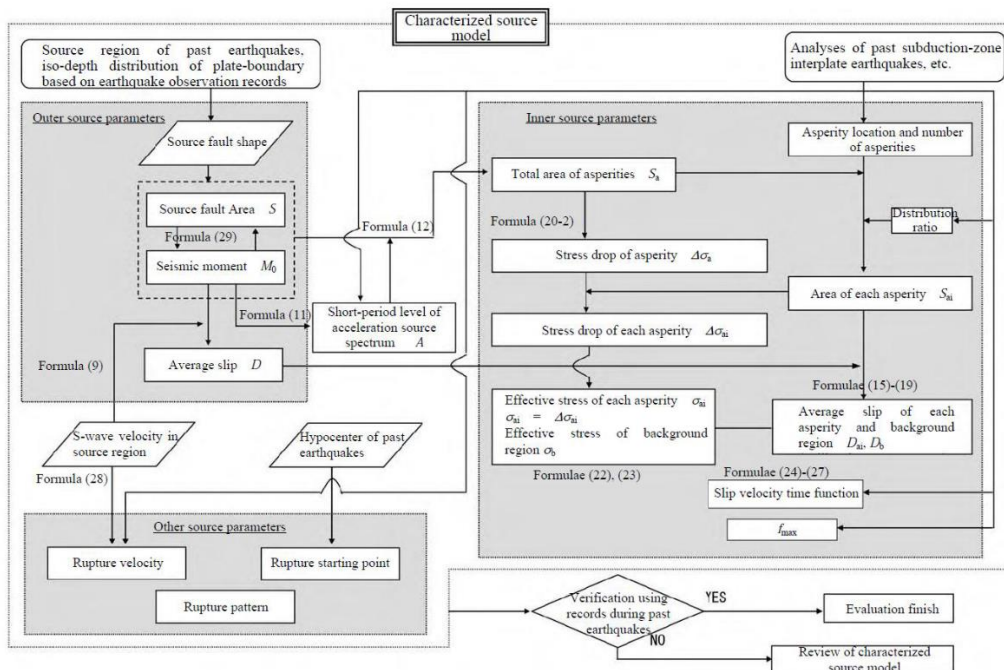


Figure 7: Flowchart of source Area characterization following the Irikura recipe (HERP, 2017)

Somerville et al. (1999) found that the ratio of the asperity area over the total fault area  $S_a/S$  is constant regardless of the rupture area and is equal to 0.22 for inland earthquakes and to 0.25 for subduction earthquakes. The stress drop on asperities is estimated following Madariaga (1979) by multiplying the average stress drop over the fault  $\Delta\sigma$  with the ratio of the total surface  $S$  over the total asperity surface  $S_a$ :

$$\Delta\sigma_a = \Delta\sigma \cdot \frac{S}{S_a} \quad \text{Eq. 3.1.5}$$

The stress drop on each asperity  $\Delta\sigma_{ai}$  is considered to be equal to the total asperity stress drop ( $\Delta\sigma_a$ ) according to the multiple-asperity model and the stress drop on one asperity subfault is equal to the

stress drop of the asperity. The average slip on asperity is considered to be twice the slip on the fault, based on Somerville *et al.* (1999).

### 3.1.2 Application to the Teil 2019 earthquake

#### 3.1.2.1 Parameters of main event

Parameters of the main event are set according to the benchmark case (moment magnitude, stress drop, surface, nucleation localization, strike, dip, and rupture velocity). From the Interferometric SAR, the co-seismic displacement field is mapped and with an inversion process, Cornou *et al.* (2020) estimated the slip distribution. We deduced the localization and surface ratio of asperities from these data.

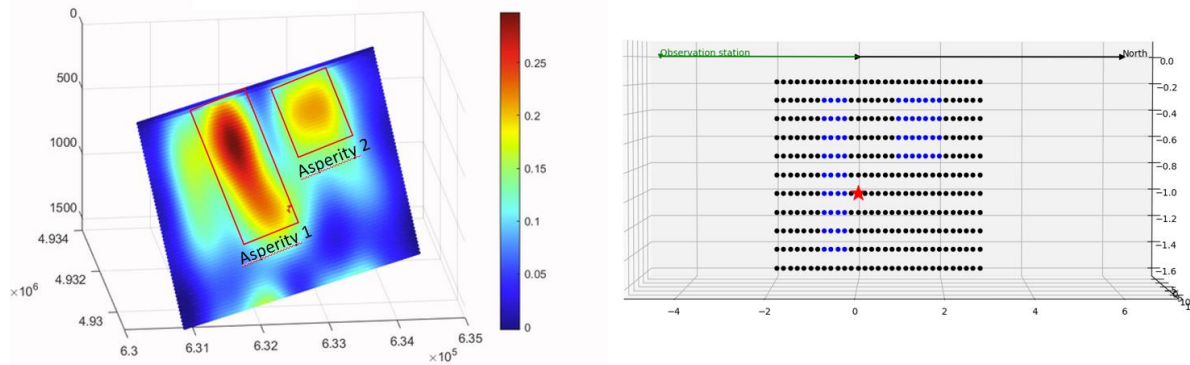


Figure 8: Left figure: localization of asperities as Irikura recipe's input, from data slip distribution of  $k^2$ -model, inspired from inversion data of Cornou *et al.* (2020); right figure: representation of asperities in Irikura recipe code

The underlying assumption is that Fourier spectrum of seismic motion follows the  $\omega^2$ -model developed by Aki (1967). This model predicts the rise of acceleration spectra with a slope in  $\omega^2$  until the corner frequency, and a flat spectra above, i.e in high-frequency. Based on observed data, Hanks (1982) showed that in reality the Fourier acceleration spectra decays with increasing frequency above a certain frequency called cut-off frequency  $f_{max}$ . The origin of this parameter, either it is a source-origin, path-origin or near-source-origin, is still debated. Hanks (1982), Anderson and Hough (1984) suggest that  $f_{max}$  has a path/near-site origin. However, studies of Fujiwara *et al.* (1989), Faccioli (1986), Umeda *et al.* (1984), Aki and Papageorgiou (1988) and Fujiwara and Irikura (1991) suggest that  $f_{max}$  is due to source processes. HERP (2017) proposes to apply a  $f_{max}$  correction (or  $f_{max}$  filter) when performing the simulation. HERP (2017) explains that in the strong motion evaluation section of the Earthquake Research Committee (2001), two values of  $f_{max}$  were assumed and compared: [1]  $f_{max} = 6\text{Hz}$  (Tsurugi *et al.*, 1997) ; [2]  $f_{max} = 13.5\text{Hz}$  (Sato *et al.*, 1994). As a result, the case of  $f_{max} = 6\text{Hz}$  was found to correspond better to the existing distance attenuation formula, so  $f_{max} = 6\text{Hz}$  is used for the large event. Also, we consider a filter slope  $s = 2$ .

Here, we want to determine corner frequency to validate stress drop value used within the benchmark, and check the high-frequency earthquake filter  $f_{max}$  to set the correction, and to compare this value to the one recommended by HERP (2017) in predictive case. To do it, at each stations we perform a spectral ratio with propagation and site theoretical spectra to obtain the source spectra only, and making fit the  $\omega^2$ -model and a Butterworth filter, respectively.

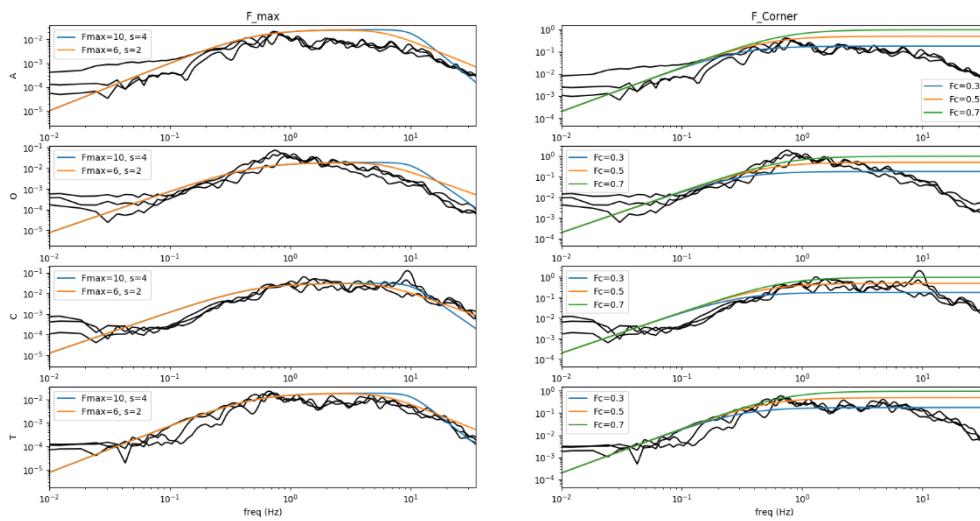


Figure 9: Checking the value of corner frequency and high-frequency filter (colored lines) at each station (A=ADHE, O=OGLP, C=CRU1, T=TRI2) for the Teil 2019 earthquake with the spectral ratio methodology for the three components (black lines).

We found that the best value for corner frequency is  $f_c = 0.5 \text{ hz}$ , corresponding to a stress drop of about 20 bar (Boore, 2009). Hence, it confirms the stress drop value set for the benchmark. It also gave framing value of corner frequency, values which will be used for uncertainty propagation in the last part of this report.

We determine that for high-frequency filter, the best parameter is  $F_{max} = 6 \text{ hz}$  with a slope of 2. These values are coherent with recommendation given by HERP (2017). It suggests that the Irikura recipe is, on this point, usable as it is in a country with low-to-moderate seismicity.

### 3.1.2.2 Parameters of EGFs

For the benchmark, two EGFs are selected which occurred on 13 November 2019 and 23 November 2019, where their parameters are given in the following table. The EGF\_23112019 presents the same focal mechanism than main event, at the contrary of EGF\_13112019. Therefore, we can expect that simulation with EGF\_23112019 will give results closer from observed data than EGF\_13112019.

Table 3: Parameters for the benchmark EGFs

Date	13/11/2019	23/11/2019
Hour	14h42	23h14
Magnitude	2.2 MLv	2.8 ML
Latitude	44.56°	44.5198°
Longitude	4.65°	4.6713°
Depth	2 km	1.8 km
Parameters source	ReNaSS	Delouis et al. (2021)

For the moment magnitude, we took the reference value given by the ReNaSS from conversion equation of  $ML_v$ , hence  $M_w = 2.1$  for both events.

As for the main event, we also check values for corner frequency and high-frequency filter. We found that the best corner frequency is about 3 to 5 Hz, corresponding to a stress drop of less than 1 bar. This value is abnormally low, but the low energy of both events does not give much confidence about the used methodology. For this reason, we decided to take a generic value for the area of  $\Delta\sigma = 9 \text{ bar}$  following regional inversion in Drouet et al. (2010).

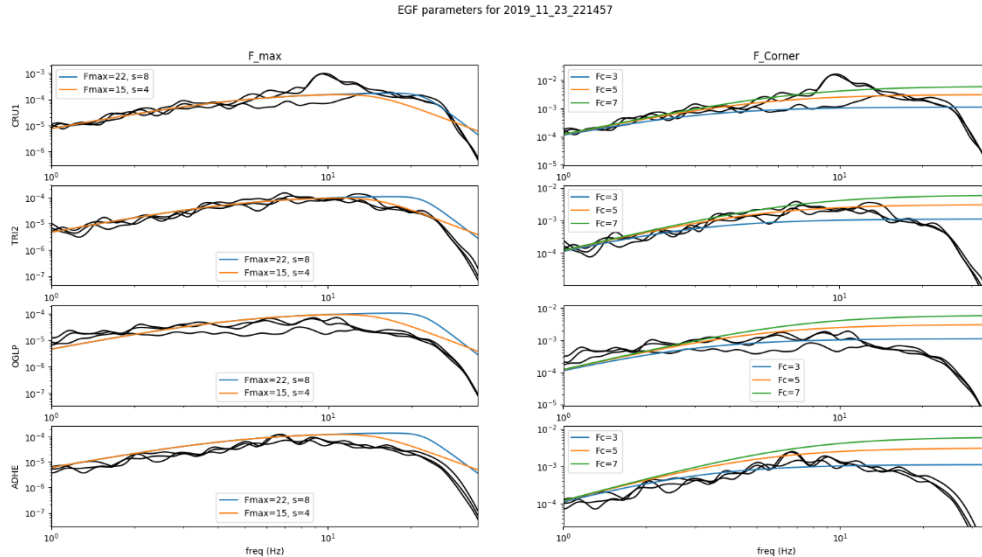


Figure 10: Checking the value of corner frequency and high-frequency filter (colored lines) at each station for the aftershock earthquake 23/11/2019 with the spectral ratio methodology for the three components (black lines).

About high-frequency filter, we found that the slope is 8 for both EGF, and  $F_{\max 23112019} = 22 \text{ Hz}$  and  $F_{\max 13112019} = 20 \text{ Hz}$ .

We also corrected the EGFs to fit subfaults parameters, according to:

- **Stress drop:** the EGF presents a stress drop of 9 bar, whereas subfaults stress drop present different values depending on their nature (background or asperity). We correct it with a simple stress drop ratio.
- **Geometrical attenuation:** following results of SIGMA project, we use a value of  $\Upsilon = 1.02$ .
- **Anelastic attenuation:** following results of SIGMA project, we use a value of  $Q_0 = 347$  and  $\alpha = 0.31$ .

### 3.1.2.3 Simulation results

Table 4 gives the source parameters estimated from Irikura recipe for the benchmark reference scenario.

Table 4: Source parameters from Irikura recipe for the referenced scenario

	<b>M0</b> (dyn.cm)	<b>S</b> (km <sup>2</sup> )	<b>Δσ</b> (bar)	<b>D</b> (km)	<b>T</b> (s)	<b>N<sub>L</sub>*N<sub>w</sub></b>	<b>N<sub>D</sub></b>
<b>Total fault</b>	2.51 <sup>e</sup> 23	8.75	20	0.170	0.24	341	21
<b>Background</b>	1.4 <sup>e</sup> 23	6.825	12.67	0.122	0.18	277	23
<b>Asp. 1</b>	7.92 <sup>e</sup> 22	1.25	90.90	0.375	0.22	36	13
<b>Asp. 2</b>	3.13 <sup>e</sup> 22	0.67	90.90	0.275	0.08	28	6

The results of the performed simulations are given in Appendix 1. Simulation results are post-processed with a correction of high-frequency filter  $f_{max}$  by realizing a simple ratio between both mainshock and EGF high-frequency filter. Then, the signal of the three components are filtered between 1 and 25 Hz because of the low signal-to-noise ratio (SNR must be superior to 1) of the EGF under 1 Hz.

The displacement values estimated from Irikura recipe on background and asperities are similar to the observed values shown in Figure 3. This observation is one point to validate the use of Irikura recipe in low-to-moderate seismic area.

From waveforms results given in Appendix 1, we observe that in general the waveform shape, duration, and amplitude is well reproduced by simulations. We quantify the adequacy of our simulations to observed data by using the Goodness-Of-Fit (GOF) (Anderson 2004) methodology for different criteria  $C$ .

$$GOF(C) = \log_{10} \left( \frac{C_{sim}}{C_{obs}} \right) \quad Eq. 3.1.6$$

We select as ground motion intensity measure the Peak Ground Acceleration PGA, Fourier Amplitude Spectra FAS (averaged on all validated frequency-range), Pseudo-Spectral Acceleration PSA at 5% damping (averaged on all validated frequency-range), the Arias Intensity AI and the effective/significant duration (from 5% to 95%). The following figure shows the GOF for PGA, FAS, PSA, AI and D595 at each station for the 3 components and for both EGFs:

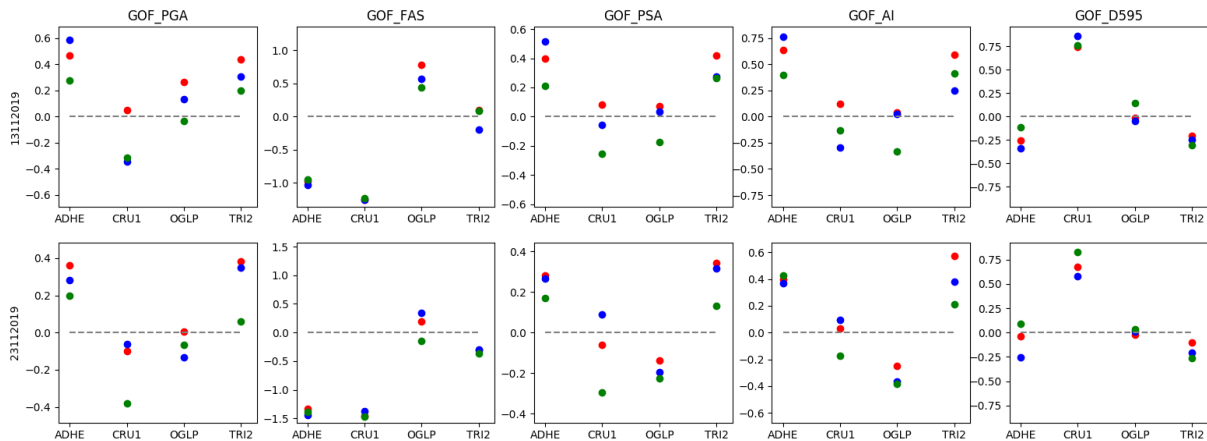


Figure 11: GOF for PGA, FAS, PSA, AI and D595 at each station for the 3 components (NS : red points, EW : blue points, Z: green points) for both EGF 13/11/2019 and 23/11/2019. For the PSA and PGA, the GOF has been averaged over frequency broad range (1-25Hz).

We observe from Figure 11 that the GOF is generally between -1 to 1, which means that simulations present good adequacy with observed data. We also note that results depend strongly on direction, station, and ground motion intensity measure. Also, the average of total GOF for all stations and for all criteria gives respectively 0.376 and 0.363 for EGF\_13112019 and EGF\_23112019. Because of the difference of focal mechanism between mainshock and EGF\_13112019, we would have expected that results would be more different for this EGF than with EGF\_23112019, but this is not the case. We can suppose that moment magnitudes of EGFs are so low that focal mechanism does not have so much impact on simulations. If this assumption is verified, it will allow to select any aftershocks in low-to-moderate seismic area to realize strong ground motion simulation, independently of their focal mechanism.

We take a look to the GOF of PSA 5% at all stations on Figure 12. We observe that the largest discrepancy is in the frequency range of about 4 to 10 Hz. One assumption to justify the large discrepancy in this frequency range is site effect. Indeed, site effects such as non-linearity is not represented in Irikura recipe methodology. Ground motions produced by the two considered EGFs are not sufficiently strong to activate non-linearity effects in the soil. Site effects are therefore not totally represented using this methodology. Finally, the vertical component presents a low GOF in PGA frequency range, suggesting a good fit in high frequency.

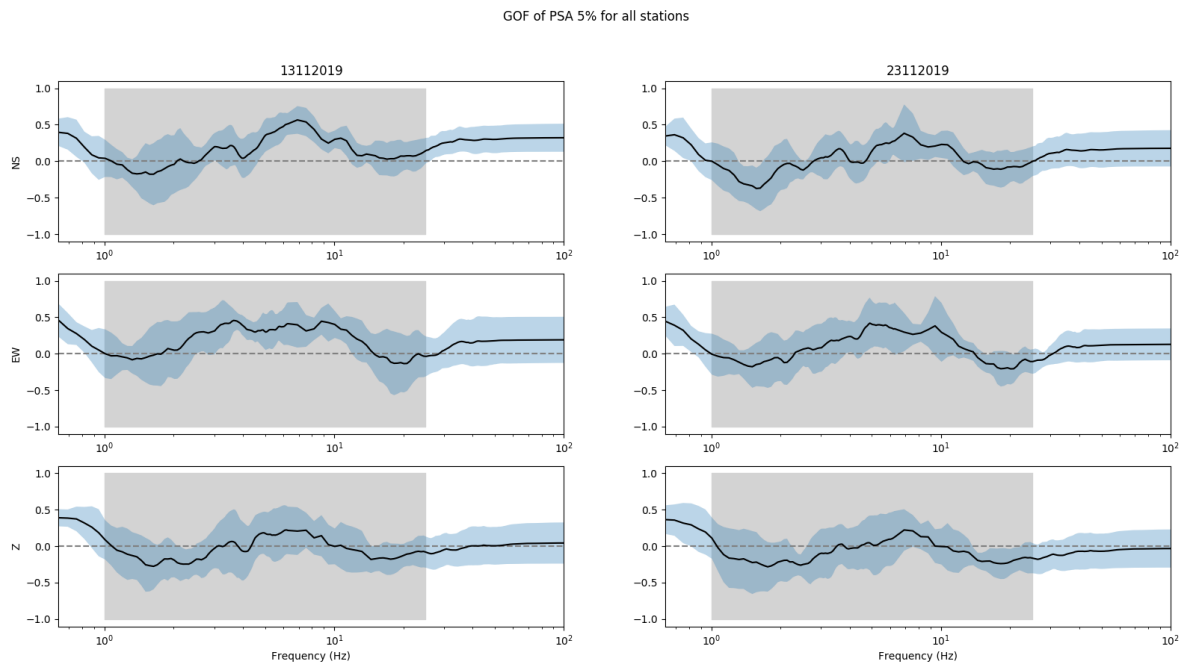


Figure 12: GOF for PSA at 5 % damping for the 3 components depending on frequency averaged on all stations for both EGF. The grey area shows the validate frequency range for simulations (1-25 Hz).

### 3.1.3 Variability and uncertainty studies

The variability/uncertainty study allows to assess and quantify the impact of natural variability and uncertainties of source input parameters on simulation results, considering all possible scenarios. Here we are interested in the comparison between uncertainties in the main event parameters with EGF uncertainties. Indeed, in low-to-moderate seismicity area, EGFs are very small, leading to large uncertainties in the assessment of its parameters. Hence, we can wonder how much EGF uncertainties can overcome main event's uncertainties. To realize the variability study, we use only the EGF which occurred on 23/11/2019.

#### 3.1.3.1 Uncertainty/variability of slip distribution

The slip distribution presents some uncertainties. Indeed, we find several models in the literature, depending on used assumptions and methodologies. In this study, we use 2 models, one from Cornou et al. (2020) and the other from Denoalis et al. (2020). Both models have been enriched in high frequency with the  $k^2$ -model. From Figure 13 we can see that both models from Cornou et al. (2020) leads to same input parameters in Irikura recipe simulation. Hence, in the end we compare simulations results from 3 models: Cornou et al. (2020), Denoalis et al. (2020) and Denoalis et al. (2020) enriched in high-frequency. The differences in input parameter remains in the number of asperities, localization and shape.

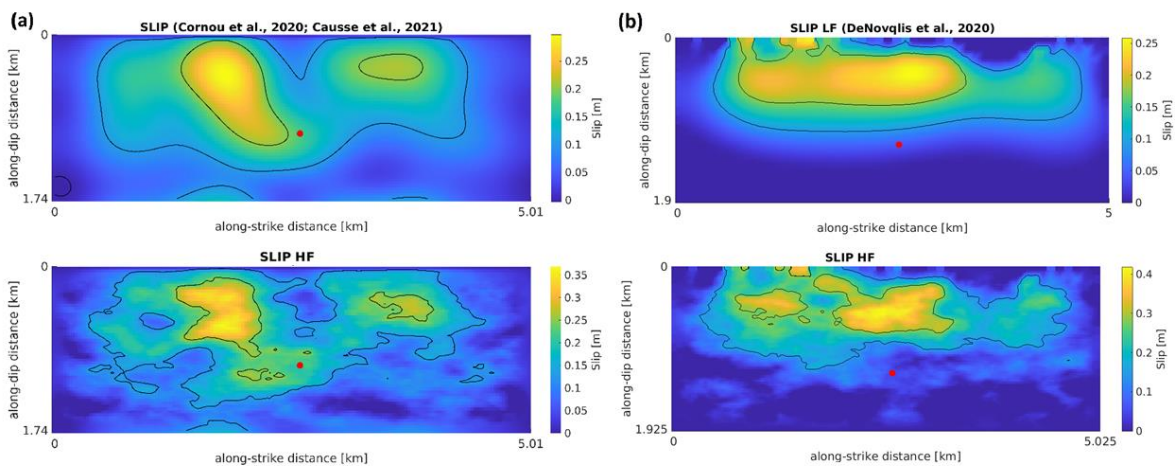


Figure 13 (a) Slip distribution from Cornou et al. (2020) (b) Slip distribution from Denoqlis et al. (2020). Below figures are respectively each model enriched in high-frequency with  $k^2$ -model.

Here, by presenting the Fourier spectrum of the results of the different simulations (Figure 14) from different slip models, we realize that the variability is rather low. The slipping models being originally rather similar (same zone of asperity, same maximum slip, only the number of asperities and their shapes change): it shows that the slip model can be defined in a rough way and that it is not necessary to detail it finely because the variability generated by these details is relatively low.

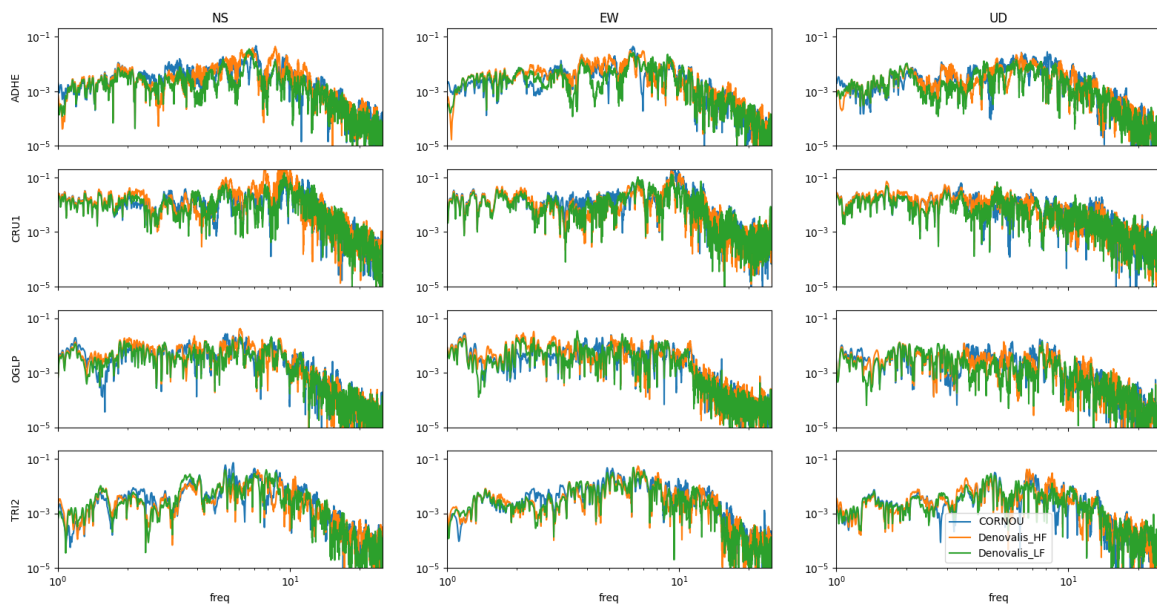


Figure 14 Variability in Fourier Spectra due to input slip distribution variability

### 3.1.3.2 Comparison of variability/uncertainty of main event with EGF

For a same rupture scenario (same moment magnitude, surface, strike, dip, nucleation position), we want to study the impact of uncertainty on source parameters of the main event: stress drop, rupture velocity and rise time. To do this, we realize 100 simulations at each station with a random parameter value generator which follows a uniform distribution. For stress drop distribution we set the possible values between 3 to 50 bar (according to the framing values of corner frequencies of main event, Figure

9),  $\alpha$  for rise time between 0.25 and 0.5 (according to framing value of HERP 2017), and a ratio velocity between 0.6 and 0.8 (according to usual values met in literature).

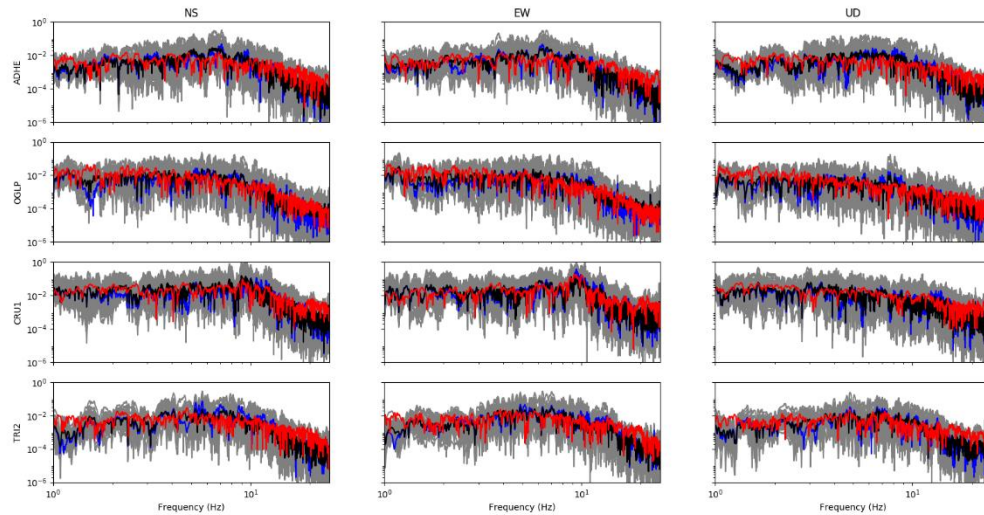


Figure 15 Fourier amplitude spectra (m/s) for the 100 simulations (grey) with mean (black) compared to benchmark simulations (blue) and observed event (black)

We observe that propagation of uncertainty of the source parameters for the target event leads to a large variability in simulated ground motion. The high-frequency content of observed data are located in the top simulations framing, suggesting that higher values of stress drop, rise time or rupture velocity can be used to have a better fit in high-frequency.

We want to compare the uncertainties of main event with uncertainties of EGF. Based on same process as variability of main event, we realize 100 simulations at each station with a random parameter value generator which follows a uniform distribution. In the EGF case, we consider that main uncertainties come from moment magnitude and stress drop. Indeed, the EGF is so small that moment magnitude and stress drop presents large uncertainties. As we have no indications for uncertainty on moment magnitude and stress drop, we decide to:

- consider an uncertainty of +/- 0.3 in the determination of EGF's moment magnitude based on Pavic et al. (2000). Therefore, the moment magnitude range is [1.8-2.4].
- The study of corner frequency shows a very low stress drop of maximum 1 bar. Even if the methodology presents large uncertainty in this case, we consider this value in the variability study as the minimum value. Therefore, we fix the stress drop value within [1-9] bar.

The variability of these two parameters will lead to variation in EGF's rupture surface estimation and hence on the number of events to sum up. Figure 16 shows results. In general, the effective duration is the measurement that presents the least variability, while the Arias intensity presents a variability similar to that of the PGA. Also, in our study conditions, the variability generated by the uncertainty on the EGF and the uncertainty on the main event are similar. Therefore, reducing the uncertainty of the EGFs is as important as reducing the source parameters uncertainties of the large earthquake.

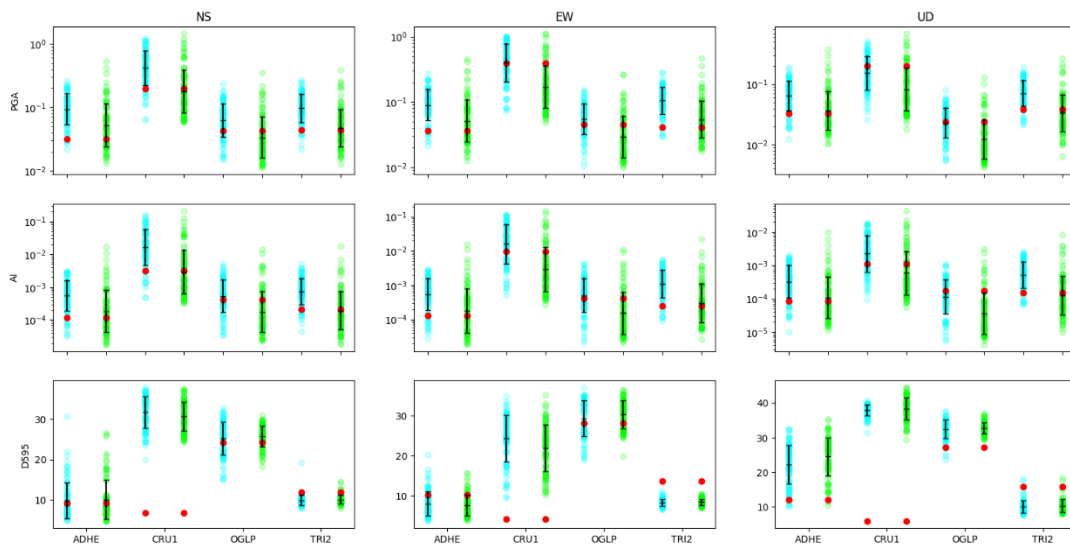


Figure 16 Variability study of 100 simulations on EGF parameters (blue points) and of 100 simulations on main event parameters (green points) on PGA, arias intensity and effective duration. Red points correspond to observe data and bar to mean and standard deviation.

### 3.1.4 Conclusion on Irikura recipe in low-to-moderate seismicity

The Irikura recipe is a methodology based on EGF summation and stress drop variability on the fault. As indicated by its name, this is a recipe which allow to estimate the source parameters for ground motion prediction, from either theoretical or empirical relations. Empirical relations are built with earthquake data from high-seismicity area. Because of that, we can question the validity of Irikura recipe in a low-to-moderate seismic area. Also, the Irikura recipe has been verified and validated in high-seismicity areas, but not in low-to-moderate seismicity areas.

Here we check the validity of Irikura recipe on the Teil 2019 earthquake. The records of aftershocks allow to use the technique of EGFs. We saw that the EGF low amount of energy implies that (1) the SNR does not allow to perform simulation below 1Hz (2) their focal mechanism does not matter. We also observed that Irikura recipe predicts well the slip distribution and gives results with good adequacy with observed data in terms of waveform's shape, duration, and amplitude. The GOF is relatively small ( $<1$ ) for the different used criteria (PGA, FAS, PSA, AI and D595), but is strongly depends on direction, station and used criteria. The main differences between simulations and observed data comes from intermediate frequency, probably due to site effects not represented in the EGFs and not modeled in the EGF methodology such as non-linearity. One suggestion to improve the EGF methodology is to integrate such effects in simulations.

Based on all these results and observation, we validate the Irikura recipe for the Teil 2019 earthquake. Simulations on other moderate earthquakes should be performed to fully validate the Irikura recipe in low-to-moderate seismicity area. One suggestion is the 1996 Epagny/Annecy earthquake as main shock. Indeed, the Annecy earthquake presents similarities with the Le Teil earthquake, shallow rupture ( $z=2\text{km}$ ), moderate magnitude ( $M_L = 5.2$ ;  $M_W = 4.9$ ). One candidate for the EGF is the 2013 Meythet earthquake ( $M_W = 2.9$ ).

The variability/uncertainty propagation study on stress drop, rise time and rupture velocity shows the large impact of these 3 parameters on simulated ground motion. Such variability should be considered when performing blind simulations for future earthquake scenarios, and additional studies should be undertaken to better understand and assess these parameters. We saw that slip distribution uncertainty deduced from different models based on observed data has no important impact on simulations, hence the slip distribution does not need to be finely detailed. However, the parameters uncertainty of very

small EGF leads to as much variation on simulations as parameters uncertainty of main event. Therefore it is as much important to characterize well EGF parameters as main event parameters, especially in low-to-moderate seismic area where the EGF energy is too low and so with large uncertainty.

## 3.2 Dujardin et al. (2020) modified method

### 3.2.1 Method overview

The Dujardin et al. (2020) method is a ground motion simulation technique combining the generation of  $k^2$  extended sources with the use of Empirical Green's Functions (EGFs). This technique was adapted to low-to-moderate seismicity regions and was applied to the Moyenne Durance Fault in France (Dujardin et al., 2020).

In this technique, the time series  $U(\vec{s}, t)$  (acceleration in our case) at a specific station  $\vec{s}$  is generated using the discrete representation theorem (Aki & Richards, 2002), as follows:

$$U(\vec{s}, t) = \int_0^L \int_0^W R(x, y; t) \cdot FG_{xy}(\vec{s}, t) dx dy \quad \text{Eq. 3.2.1}$$

where  $R(x, y; t)$  is the contribution to the total moment rate function at position  $(x, y)$  of the rupture zone,  $x$  and  $y$  denote, respectively, the along-strike ( $L$ ) and along-dip ( $W$ ) directions and  $FG_{xy}(\vec{s}, t)$  is the Green's function obtained for the position  $(x, y)$ . The generation of the moment rate function and  $FG_{xy}(\vec{s}, t)$  is briefly explained hereafter (for more details, refer to Dujardin et al. (2020)).

#### 3.2.1.1 Fault rupture generation

In the method developed by Dujardin et al. (2020) and based on the proposition of Herrero and Bernard (1994), the rupture area dimensions are calculated from the seismic moment ( $\overline{M0}$ ) and the rupture stress drop ( $\Delta\sigma$ ) of the simulated event. In our case study, the method has been modified to have constant rupture area dimensions. As per section 2,  $L$  and  $W$  are, respectively, equal to 5000 m and 1750 m.

The moment rate function ( $M_0(t)$ ) is defined as follows:

$$M_0(t) = \int_0^L \int_0^W R(x, y; t) dx dy = \mu \int_0^L \int_0^W D(x, y) \cdot [SRF(t) * \delta(t - T(x, y))] dx dy \quad \text{Eq. 3.2.2}$$

where  $\mu$  is the rigidity ( $\mu = \rho V_s^2$  where  $\rho$  is the density and  $V_s$  is the S-wave velocity),  $D(x, y)$  and  $T(x, y)$  are, respectively, the static slip and the rupture time at position  $(x, y)$  and  $SRF(t)$  is the Slip Rate Function. The  $M_0(t)$  can also be defined in the frequency domain as follows (see Eq. 3 in Hisada (2001)):

$$M_0(f) = \mu \int_0^L \int_0^W D(x, y) \cdot [SRF(f) \cdot e^{i\omega T(x, y)}] dx dy \quad \text{Eq. 3.2.3}$$

If the slip distribution is not defined,  $D(x, y)$  can be generated randomly, by separating the slip at low and high frequencies, as follows:

$$D(x, y) = \frac{\overline{M0}}{\mu A} + FT^{-1}(D(k_x, k_y)) \quad \text{Eq. 3.2.4}$$

where  $A$  is the rupture area ( $A = L \cdot W$ ),  $FT^{-1}$  denotes the inverse Fourier Transform operator and  $D(k_x, k_y)$  is the displacement spectrum. For a rectangular fault plane,  $D(k_x, k_y)$  is defined based on Somerville et al. (1999) and Gallovič and Brokešová (2004), as follows:

$$D(k_x, k_y) = \frac{\overline{M0}}{\mu \sqrt{1 + \left[ \left( \frac{k_x}{k_{Cx}} \right)^2 + \left( \frac{k_y}{k_{Cy}} \right)^2 \right]^2}} e^{i\phi(k_x, k_y)} \quad \text{Eq. 3.2.5}$$

where  $k_x$  and  $k_y$  are the wavenumbers, respectively, along-strike and along-dip directions,  $\phi(k_x, k_y)$  is the phase spectrum generated randomly and  $k_x$  and  $k_y$ , the corner wavenumbers, are equal,

respectively, to  $kC \frac{W}{L}$  and  $kC \frac{L}{W}$  (where  $kC = \frac{fc}{V_R}$  (Hanks (1979) and Hanks and McGuire (1981)));  $fc$  are  $V_R$ , respectively, the corner frequency and the rupture speed of the target event).

In our study, the slip rate function ( $SRF(t)$ ) is obtained by the isosceles triangles summation proposed by Hisada (2001). Instead of using the Somerville et al. (1999) definition of the rise time, the duration of the SRF ( $\tau_{rise}$ ; similar to  $\tau_{max}$  in Hisada (2001)) is defined, in this study, according to the HERP (2008) recommendation, as follows:

$$\tau_{rise} = \alpha \frac{W}{V_r} \text{ avec } \alpha = 0.30 \quad \text{Eq. 3.2.6}$$

In our study, the SRF's input parameters,  $Nv$  and  $Ar$  (the number of summed triangles and Aspect ratio, respectively; see Hisada (2001)) are taken equal to 4 and  $\sqrt{2}$ , respectively.

The rupture time at position  $(x, y)$  of the fault is given by:

$$T(x, y) = \frac{D_{nuc}(x, y)}{V_R} [1 + \Delta T_R(x, y)] \quad \text{Eq. 3.2.7}$$

where  $V_R$  is the rupture speed,  $D_{nuc}(x, y)$  is the distance between the position  $(x, y)$  and the nucleation's position and  $\Delta T_R(x, y)$  is determined, similarly to  $D(k_x, k_y)$  (Eq. 3.2.5), as follows:

$$\Delta T_R(x, y) = \frac{1}{\sqrt{1 + \left[ \left( \frac{k_x}{kC_{Tx}} \right)^2 + \left( \frac{k_y}{kC_{Ty}} \right)^2 \right]^2}} \quad \text{Eq. 3.2.7}$$

If the rupture time on the fault is constant,  $\Delta T_R(x, y)$  is equal to 0 and  $V_R$  is considered constant.

### 3.2.1.2 Green's functions generation

The  $FG_{xy}(\vec{s}, t)$  at position  $(x, y)$  in Eq. 3.2.1 is approximated using the nearest available EGF. To be considered as Green's function, the chosen EGF at position  $(x, y)$  is deconvolved, in the frequency domain, from its theoretical source spectrum  $S(m_0, f_c^*)$ . The EGF's source spectrum is estimated according to the  $\omega^{-2}$  source model defined by Brune (1970), as follows:

$$S(m_0, f_c^*) = \frac{m_0}{\left[ 1 + \left( \frac{f}{f_c^*} \right)^2 \right]} \quad \text{Eq. 3.2.8}$$

where  $m_0$  and  $f_c^*$  are, respectively, the seismic moment and corner frequency of the EGF.

After the deconvolution of the EGF, many corrections are applied on the initial Green's function  $FG_0(\vec{s}, t)$ .

First, a correction of the travel-time between the initial and new position of the Green's function is applied:

$$FG_{xy}^{adj,1}(\vec{s}, t) = FG_0(\vec{s}, t) * \delta \left( t - \frac{R_{STA(\vec{s})}^{SF_{xy}} - R_{STA(\vec{s})}^{FG_0}}{V_s} \right) \quad \text{Eq. 3.2.9}$$

where  $R_{STA(\vec{s})}^{SF_{xy}}$  is the distance between the station  $STA(\vec{s})$  and the position  $(x, y)$  on the fault and  $R_{STA(\vec{s})}^{FG_0}$  is the distance between the station  $STA(\vec{s})$  and the position of the EGF.

Then, a correction due to the difference in the geometrical spreading is done:

$$FG_{xy}^{adj,2}(\vec{s}, t) = FG_{xy}^{adj,1}(\vec{s}, t) \times \left( \frac{R_{STA(\vec{s})}^{FG_0}}{R_{STA(\vec{s})}^{SF_{xy}}} \right)^y \quad \text{Eq. 3.2.10}$$

where  $\gamma$  is the spreading coefficient and is taken equal to 1.03 in our study (deliverable SIGMA2-2021-D3-065).

Besides, the anelastic attenuation is also corrected between the old and new position of the Green's function. This correction is done in the frequency domain as follows:

$$FG_{xy}^{adj,3}(\vec{s}, t) = FT^{-1} \left( FT \left( FG_{xy}^{adj,2}(\vec{s}, t) \right) \cdot e^{\frac{-\pi f \left( R_{STA(\vec{s})}^{SFxy} - R_{STA(\vec{s})}^{FG0} \right)}{Qs \cdot f^{\alpha} \times Vs}} \right) \quad Eq. 3.2.11$$

where  $FT$  denotes the Fourier transform operator and  $Qs$  and  $\alpha$  are the attenuation parameters taken in our study equal to 347 and 0.32, respectively.

Finally, we implemented in the code proposed by Dujardin et al. (2020) a frequency depended radiation pattern correction (Pitarka et al., 2000). After passing from the ENZ coordinates system to the local system  $(r, \theta, \phi)$ , the coefficients  $A^r$ ,  $A^\theta$  and  $A^\phi$  are determined from Aki and Richards (2002). The radiation pattern correction can be expressed as follows:

$$FG_{xy}^{adj,4}(\vec{s}, t) = ROT^{r\theta\phi \rightarrow ENZ} \left[ FT^{-1} \left( FT \left( ROT^{ENZ \rightarrow r\theta\phi} \left[ FG_{xy}^{adj,3}(\vec{s}, t) \right] \right) \cdot RPC_{r\theta\phi} \right) \right] \quad Eq. 3.2.12$$

where  $ROT^{ENZ \rightarrow r\theta\phi}$  and  $ROT^{r\theta\phi \rightarrow ENZ}$  are, respectively, the rotation operators to pass from the ENZ coordinates system to the local system and vice versa, and  $RPC_{r\theta\phi}$  is the correction function shown in Figure 17.

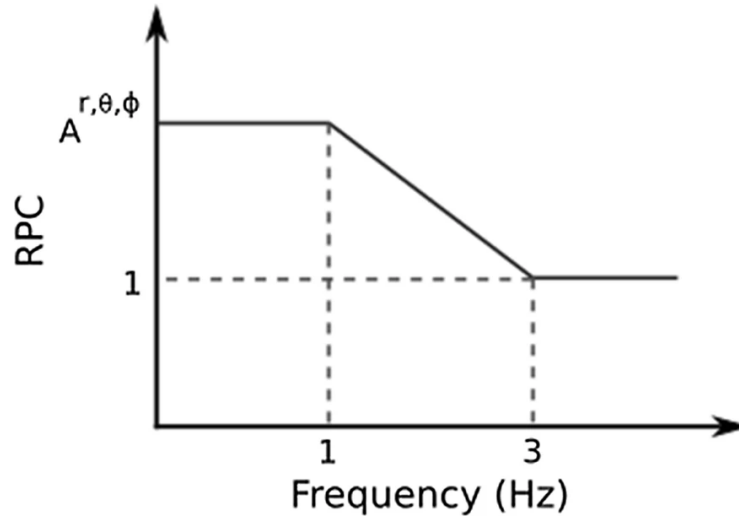


Figure 17: The frequency dependence of the Radiation Pattern Correction (RPC) function (Dujardin et al., 2020).

### 3.2.2 Application to Le Teil earthquake

As mentioned before, the “La Rouviere’s” fault was considered as an inactive fault till the Le Teil's earthquake. After the main event on the 11<sup>th</sup> of November 2019, only two aftershocks with a magnitude larger than two were recorded. Table 5 shows the metadata of the two EGFs that can be potentially used to simulate the Le Teil earthquake using the empirical method described in the previous section.

Table 5: List of the two EGFs metadata used in the simulation of Le Teil earthquake.

Event	Latitude (°N)	Longitude (°E)	Depth (Km)	Strike (°)	Dip (°)	Rake (°)	M <sub>L</sub>	Mo (Nm)	$f_c^*$ (Hz)
13/11/19	44.5637	4.6458	2.00	---	---	---	2.1	1.5849e+12	10.09
23/11/19	44.5198	4.6713	1.80	~50	~45	~89	2.1	1.5849e+12	10.09

For the two aftershocks, Figure 18 shows the signal over noise ratios (SNRs) calculated for the accelerograms recorded at five stations (ADHE, CRU1, TRI2, OGLP and A192B) where ground motions will be simulated using the Dujardin et al. (2020) modified method for a hypothetical event similar to Le Teil earthquake. The calculated SNRs show that ADHE and TRI2 (for the two aftershocks) and A192B (for the first aftershock) have a good SNR ( $>3$ ) in the three directions for frequencies larger than 1 Hz. For the second aftershock (23/11/2019), A192B has a lower SNR especially for the EW and UD directions. However, for CRU1 and OGLP, the quality of the recordings is lower than the other stations. Between 1 and 10 Hz, all the stations have a SNR larger than 1 in the three directions.

Although the mainshock was widely studied by the scientific community, the number of studies focusing on defining the rupture mechanism of the aftershocks is not exhaustive. The strike, dip and rake for the event of the 23th of November were estimated to be similar to the one of the main event (Delouis et al., 2021). The locations of the two aftershocks are shown in Figure 4 in blue and green dots. The epicenter location (Figure 4) and the rupture mechanism (Table 5) of the second aftershock are similar to the one of the main event. For this part of the study, only the second aftershock is used to simulate ground motion on surface.

Since the first aftershock has a larger SNR than the second one, the results obtained using the first aftershock only are presented in Appendix 2 and the results are discussed at the end of section 3.2.2.

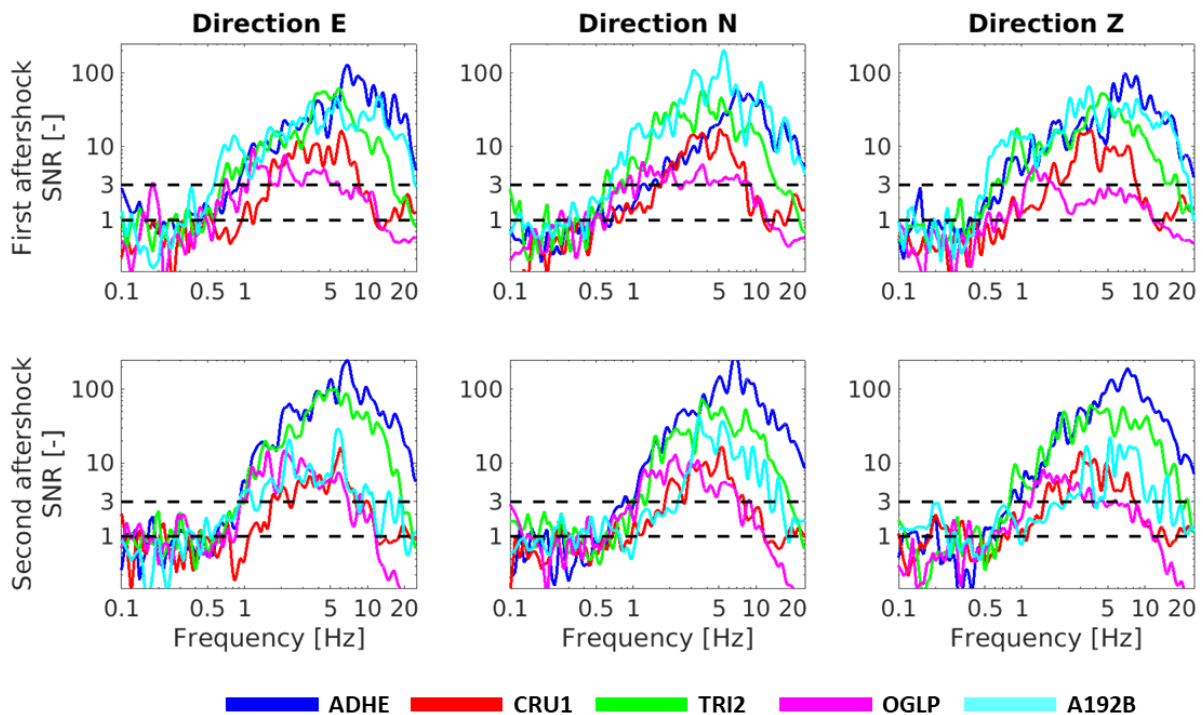


Figure 18: The signal over noise ratio (SNR) calculated for the two aftershocks' accelerograms recorded at five stations: ADHE in blue, CRU1 in red, TRI2 in green, OGLP in magenta and A192B in cyan.

In this application, the moment rate function is calculated, as per Eq. 3.2.2, using the slip distribution ( $D(x, y)$ ) estimated by Cornou et al. (2020) and Causse et al. (2021) (Figure 19a; hereafter named Slip distribution A). Figure 19c shows the amplitude of the obtained moment rate ( $M_0(f)$ ) and the theoretical  $\omega^{-2}$  spectra (Brune, 1970) computed for  $\Delta\sigma = 2.0$  MPa. The obtained  $M_0(f)$  is not in agreement with the Brune (1970) model: the slope of the amplitude beyond the corner frequency (estimated to 0.62 Hz) is not -2. Thus, a new slip distribution is calculated using Eq. 3.2.4: in the equation,  $\overline{M_0}/\mu A$  is replaced by the original slip in Figure 19a. The new slip model (Figure 19b; hereafter named Slip distribution B) generates a moment rate in agreement with Brune model (1970) (Figure 19d).

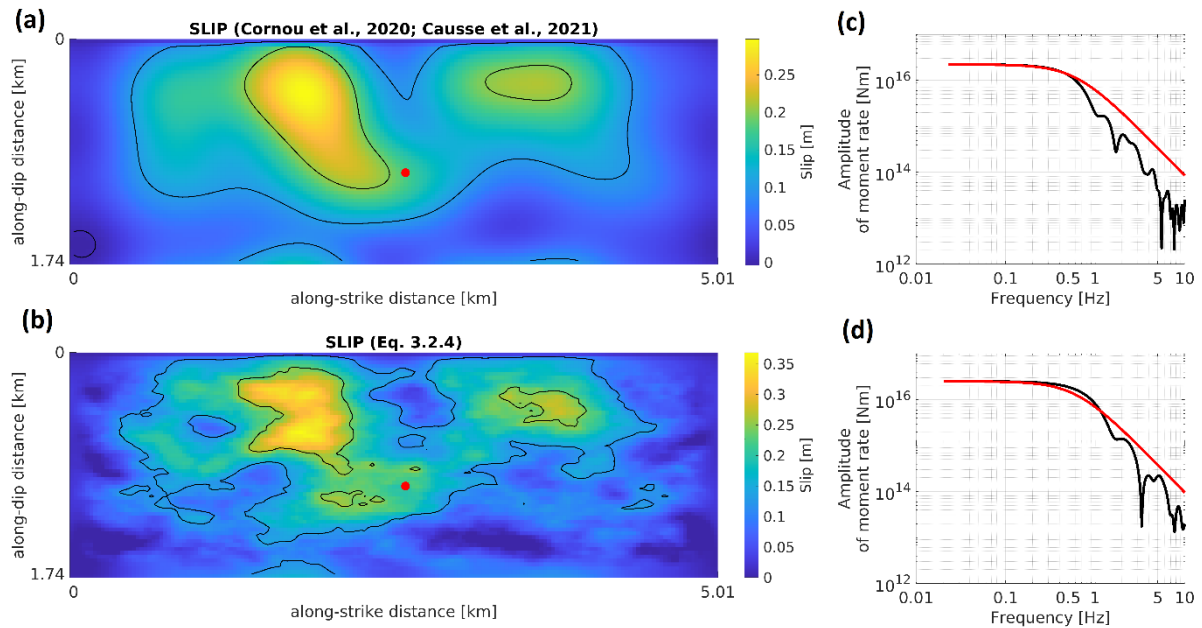


Figure 19: The static slip distribution (a) estimated by Cornou et al. (2020) and Causse et al. (2021) and (b) calculated using Eq. 3.2.4 (refer to text for details) with the corresponding moment rate amplitude (respectively, in (c) and (d)). The red dots in (a) and (b) correspond to the nucleation position on the fault. The theoretical  $\omega^{-2}$  spectra (Brune, 1970) computed for the medium value  $\Delta\sigma = 2.0$  MPa is represented by the red curves in (c) and (d).

The two slip models (Figure 19) are used to generate ground motion at the surface for the five stations, using the Dujardin et al. (2020) modified technique. Within a frequency range between 1 and 10 Hz (range where the two EGF have SNR larger than one for all stations and directions), Figure 20 compares the calculated time series to the one recorded in-situ for the Le Teil 4.9Mw earthquake. The slip distribution B (Figure 19b) seems to better reproduce the waveforms recorded on station than the slip distribution A (Figure 19a). The similarity between the recorded and the simulated accelerograms seems to depend on the considered station. For example, the accelerograms simulated for stations CRU1 and OGLP using the slip distribution B (green curves in Figure 20) are very close to the one recorded in situ. Even though the peak accelerations are close, the accelerations simulated for station ADHE and TRI2 are different from the one recorded. The arrival time of S wave and the duration of the signals are different. As it can be seen on the bottom of Figure 20, the velocimetric sensor of station A192B, the closest station to the rupture zone, saturated during the shaking and the waveform at this station is therefore clipped. In the following, this station will be shown in the future analysis and figures but omitted from any interpretation or conclusion.

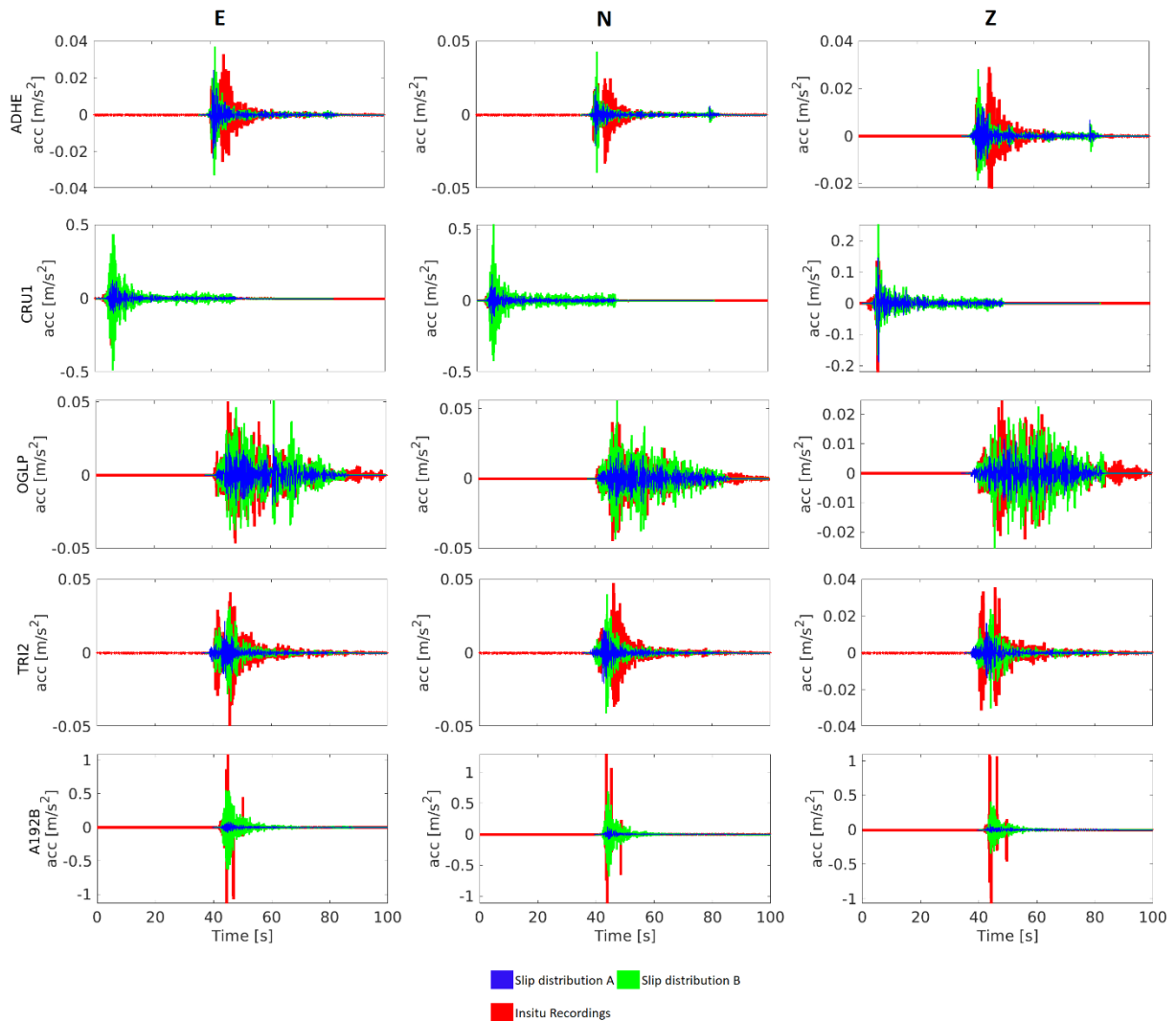


Figure 20: Comparison of the accelerograms simulated using the slip distribution estimated by Cornou et al. (2020) (in blue) and the slip distribution calculated as per Eq. 3.2.4 (in green; see text for more details) to the recorded acceleration (in red) for the three components of the five analyzed stations (ADHE, CRU1, OGLP, TRI2 and A192B).

Figure 21 represents the Fourier Amplitude Spectra (FAS) of the empirical simulations obtained with the two different slip distributions and the waveforms recorded by the five stations for the mainshock. At low frequencies ( $<2.5$  Hz), the results obtained from slip distribution A and slip distribution B are similar. This was expected since the moment rate functions (Figure 19c and d) are very similar at low frequencies. However, slip distribution B (Figure 19b) allows to better reproduce the FAS of the recorded accelerograms especially at high frequencies.

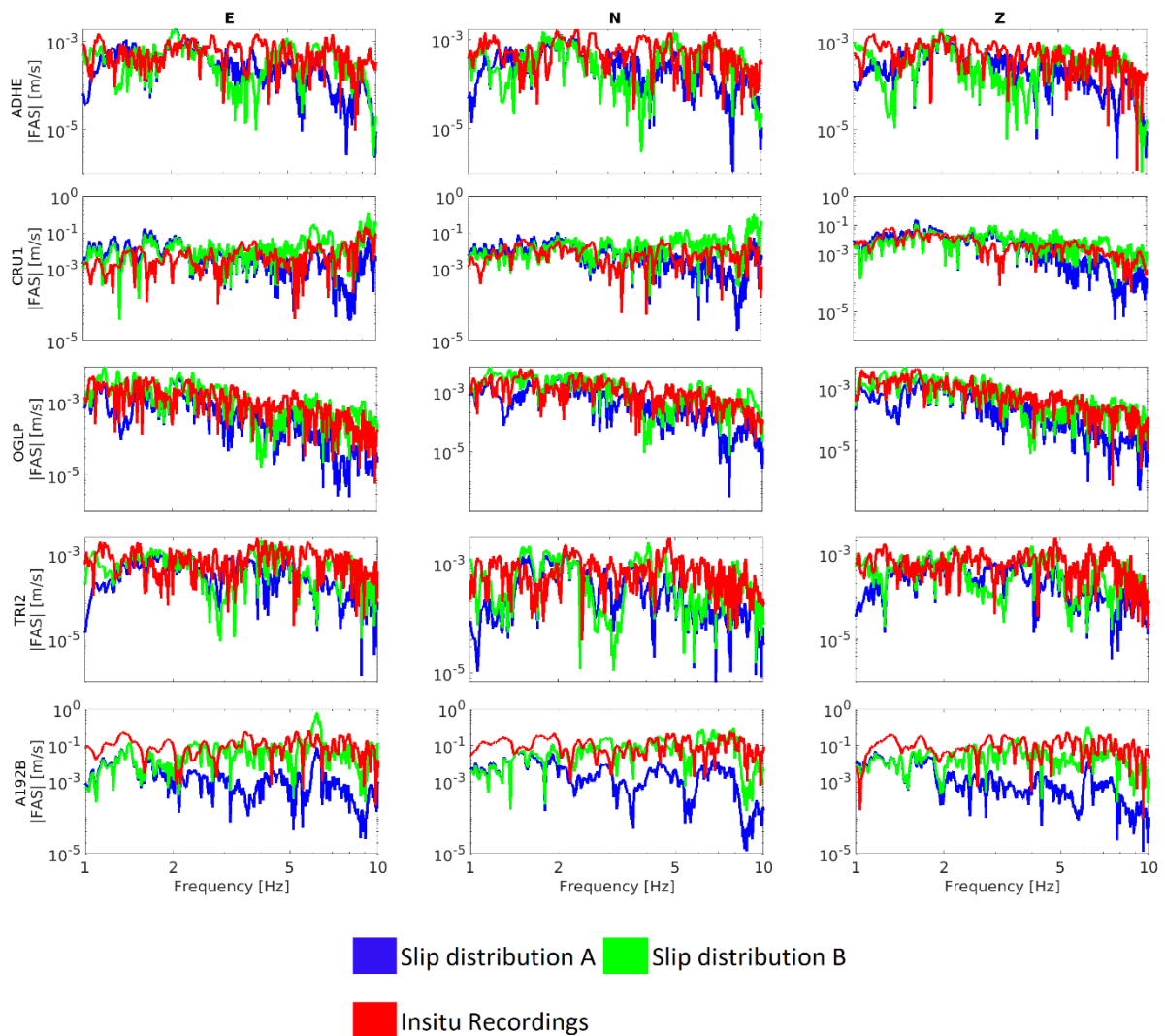


Figure 21: The Fourier Amplitude Spectra of the accelerograms simulated using the slip distribution estimated by Cornou *et al.* (2020) (in blue) and the slip distribution calculated as per Eq. 3.2.4 (in green; see text for more details) and the accelerograms recorded in-situ (in red) for the three components of the five analyzed stations (ADHE, CRU1, OGLP, TRI2 and A192B).

In the time domain, three ground motion (GM) intensity measures (PGA, Arias Intensity and Duration) are used to compare the simulated and observed results of the Le Teil earthquake. The results, plotted in Figure 22, show again the outputs dependency on the analyzed direction, station and ground motion intensity measure. Overall, the PGA is better estimated than the other GM intensity measures. This can be explained by the fact that PGA is more sensitive to the high frequencies (Kramer, 1996) and the comparison between simulated and recorded data is better for high frequencies than low frequencies (Figure 21).

Finally, the differences observed between the simulation and the recorded data may be due to: the frequency content of the EGF's recordings, the source parameters (and/or the rupture mechanism) of the Le Teil earthquake and/or the aftershocks used as EGFs.

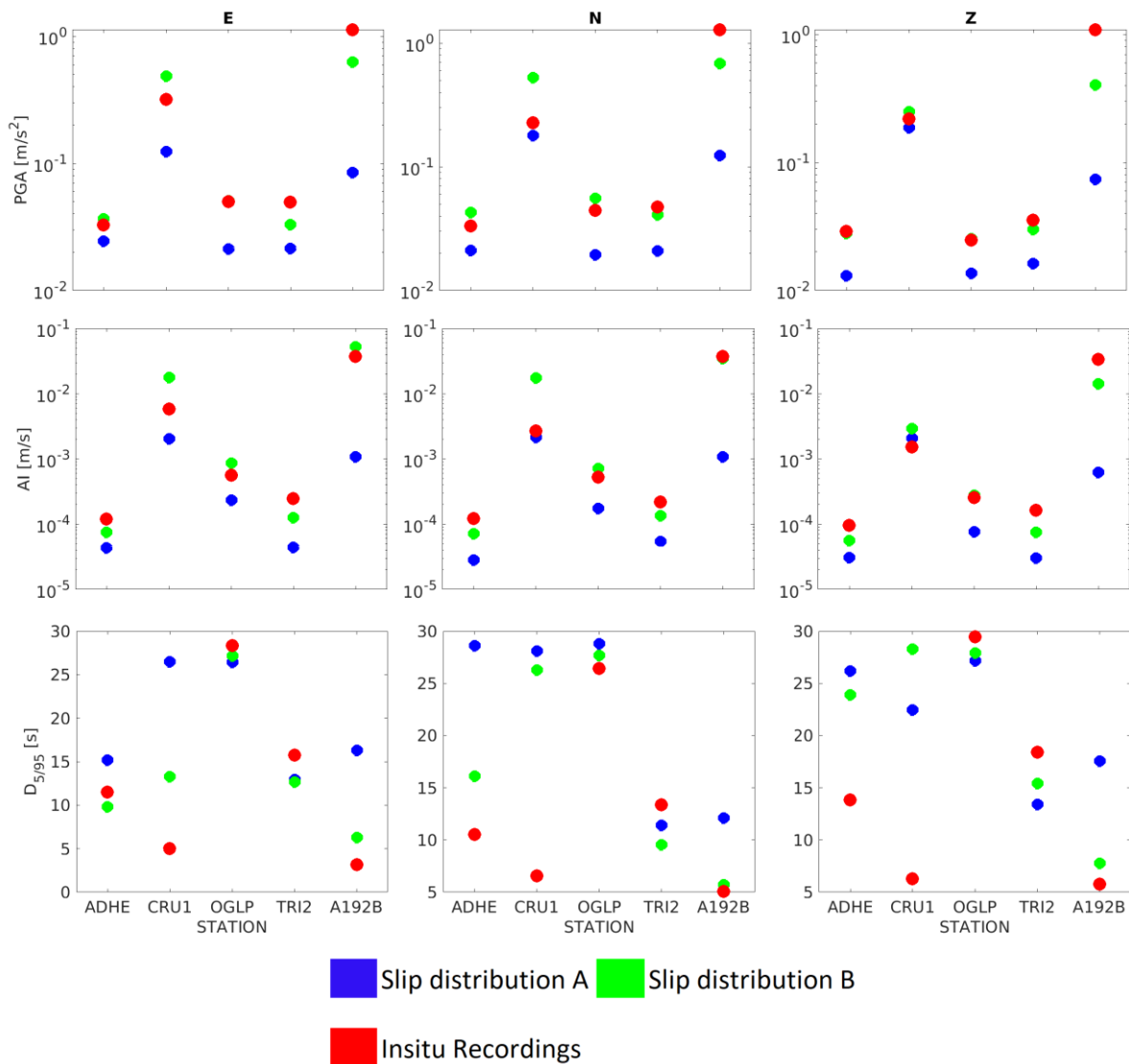


Figure 22: After filtering between 1 and 10 Hz, the comparison of the three ground motion intensity measures in the time domain (PGA, AI and Duration) calculated for the accelerograms simulated using the slip distribution estimated by Cornou et al. (2020) (in blue) and the slip distribution calculated as per Eq. 3.2.4 (in green; see text for more details) and the accelerograms recorded in-situ (in red) for the three components of the five analyzed stations (ADHE, CRU1, OGLP, TRI2 and A192B).

The results shown in this section are obtained using only the aftershock of the 23<sup>rd</sup> of November 2019 as EGF. The figures in Appendix 2 show the results obtained by using only the aftershock of the 13<sup>th</sup> of November 2019 as EGF. Even though this EGF is located farther from the rupture zone and its properties are not well defined, the results are almost similar.

### 3.2.3 Sensitivity study

In order to understand the impact of input uncertainties on the ground motion variability on ground motion simulated at the surface using the Dujardin modified method, two sensitivity studies are realized:

- Variability of target event source parameters
- Variability of the EGF input parameters

For each of the two sensitivity study, a set of four input parameters are modeled as random variables. The impact of the input variability on the output variability is evaluated by estimating, for each input and each output, the variability coefficient  $\alpha$  calculated as follows:

$$\alpha = \frac{COV_{output}}{COV_{input}} = \frac{[prctl(output, 84\%) - prctl(output, 16\%)]/prctl(output, 50\%)}{[prctl(input, 84\%) - prctl(input, 16\%)]/prctl(input, 50\%)} \quad Eq. 3.2.13$$

where  $prctl$  is the percentile operator.

For the frequency dependent parameter (ex: FAS), the variability coefficient  $\alpha$  is calculated by averaging the ratio in Eq. 3.2.13 between 1 and 10 Hz.

### 3.2.3.1 Source parameters' variability

In this sensitivity study, four input source parameters are analyzed independently as random variables: the stress drop ( $\Delta\sigma$ ), the rupture speed ( $V_{rup}$ ) and the position of the nucleation on the rupture plan (2 parameters:  $X_{nuc}$  and  $Y_{nuc}$ ). For each parameter, 100 simulations are generated while all the three other parameters are considered constant equal to the median value. For each simulation, ground motion is calculated using the Dujardin modified technique for the five stations: ADHE, CRU1, OGLP, TRI2 and A192B.

Figure 23 represents the histogram of the four random variables analyzed in this part. The stress drop ( $\Delta\sigma$ )  $pdf$  is considered a normal distribution with an average value of 2 MPa and a CoV of 20%. The rupture speed  $pdf$  is considered a uniform distribution with minimum and maximum values, respectively equal to 1500 and 2500 m/s. For the nucleation position, a uniform distribution is used for both  $X_{nuc}$  and  $Y_{nuc}$  with minimum and maximum respectively equal to (10%, 90%) and (60%, 90%).

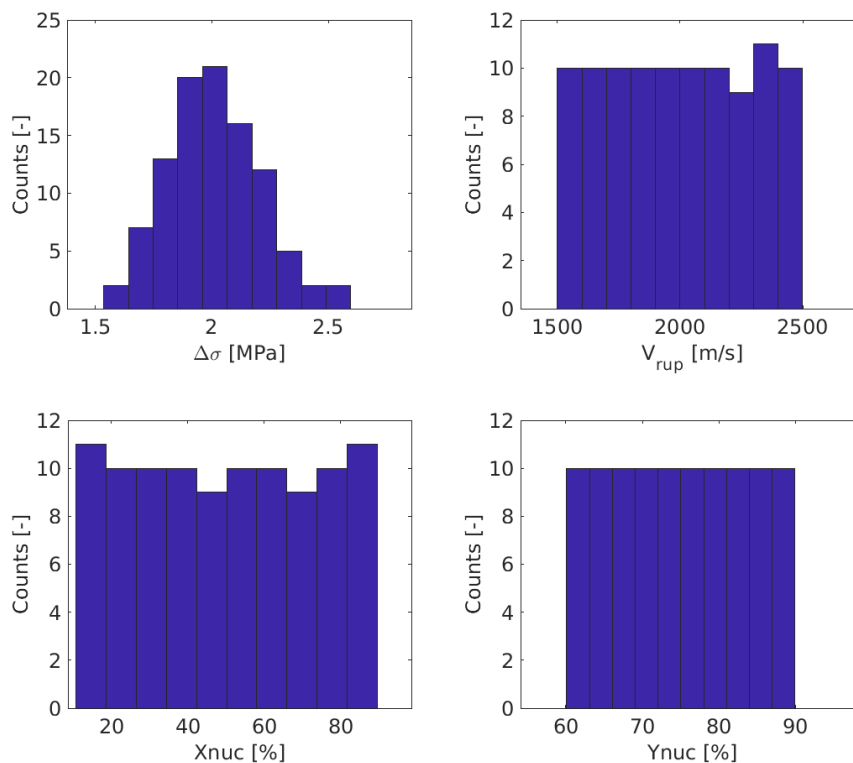


Figure 23: The histograms of the random variables defining the source parameters of the target event: stress drop ( $\Delta\sigma$ ), rupture speed ( $V_{rup}$ ), the nucleation position on the rupture plan ( $X_{nuc}$ ,  $Y_{nuc}$ ).

Figure 24 shows the variability coefficient  $\alpha$  calculated for the four random inputs:  $\Delta\sigma$ ,  $Vrup$ ,  $Xnuc$  and  $Ynuc$ . Unlike the variability coefficient of FAS ( $\alpha(FAS)$ ), the variability coefficient for the GM intensity measures in the time domain depends on the analyzed station and direction. As mentioned before, the GM intensity measures in the time domain may be sensitive to a very specific frequency band. However,  $\alpha(FAS)$  is calculated by averaging between 1 and 10 Hz which leads to a more stable results.

The variability analysis of the different outputs shows that the stress drop of the target event (black dots in Figure 24) is the input parameter that most controls the results. On the other hand, the nucleation position along the strike (defined by  $Xnuc$ ) is the parameter with the lowest impact in the sensitivity analysis among the four varied parameters.

Figure 24 also shows that the Arias Intensity is more sensitive to the variability of the input source parameters of the target event than the other GM intensity measures. The coefficient  $\alpha(AI)$  is almost two times larger than the coefficients of the other analyzed outputs.

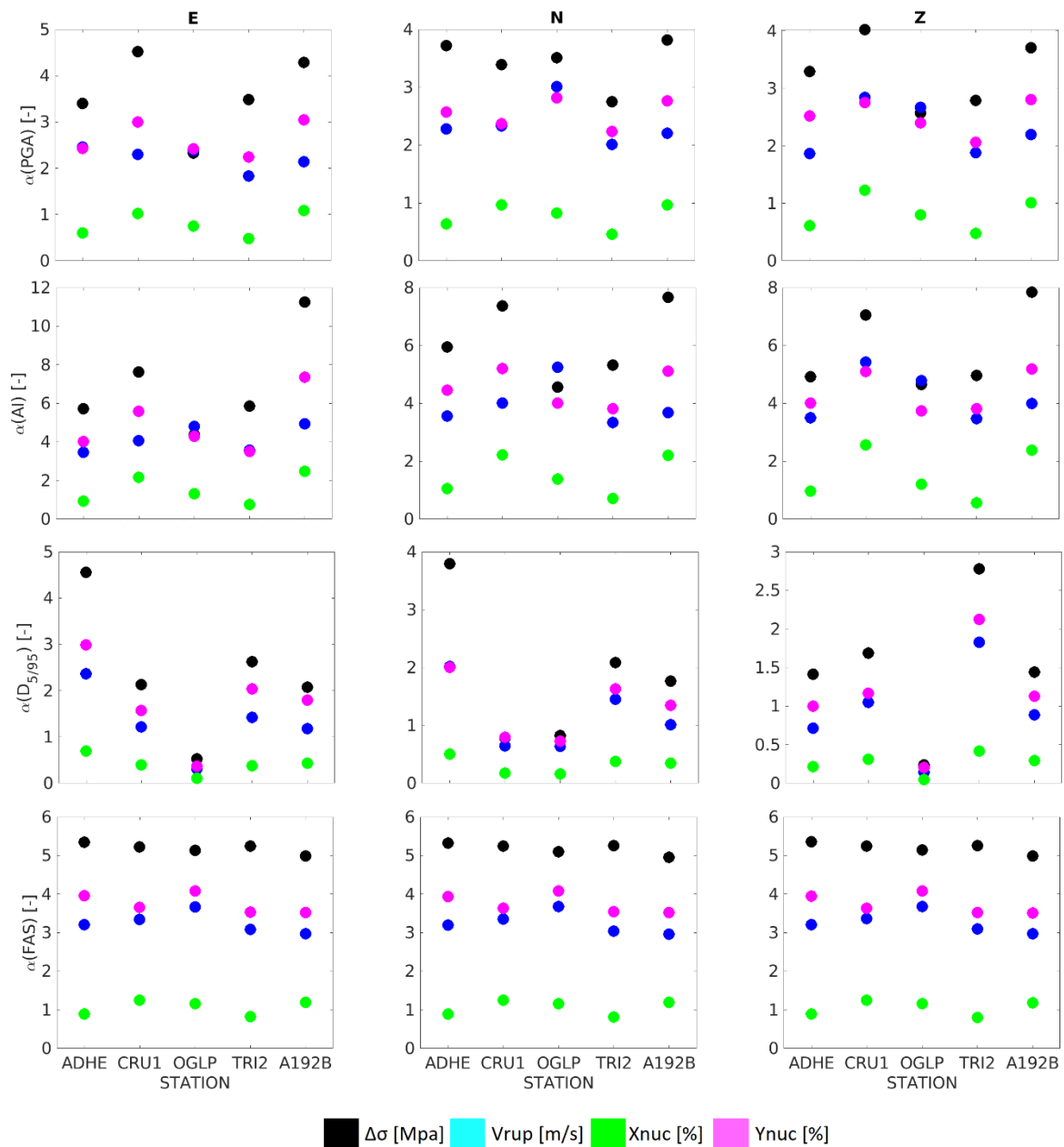


Figure 24: Variability coefficient  $\alpha$  for the five ground motion intensity measures: PGA, Arias Intensity, Duration and FAS (from top to bottom) estimated for the five stations: ADHE, CRU1, OGLP, TRI2 and A192B by varying the source parameters of the target event.

To complete this sensitivity study, the four input parameters defining the source of the target event have been varied at the same time. From the 100 simulations, an average value  $\pm$  one std is estimated for the four GM intensity measures (PGA, Arias Intensity, Duration and FAS) at each station and each component. Figure 25 and Figure 26 show the results obtained for the 100 simulations (in grey) and allow to compare the corresponding average value  $\pm$  one std (in black) to the results of the recorded data in-situ (in red).

Among the considered ground motion parameters, the PGA is the parameters best represented by the average of the 100 simulations; for the majority of the stations and the components, the black dots are close to the red dots (Figure 25). In the frequency domain (Figure 26), the FAS of the recorded data (red curve) is located between the  $\pm$  one std obtained from the 100 simulations (dashed black curves).

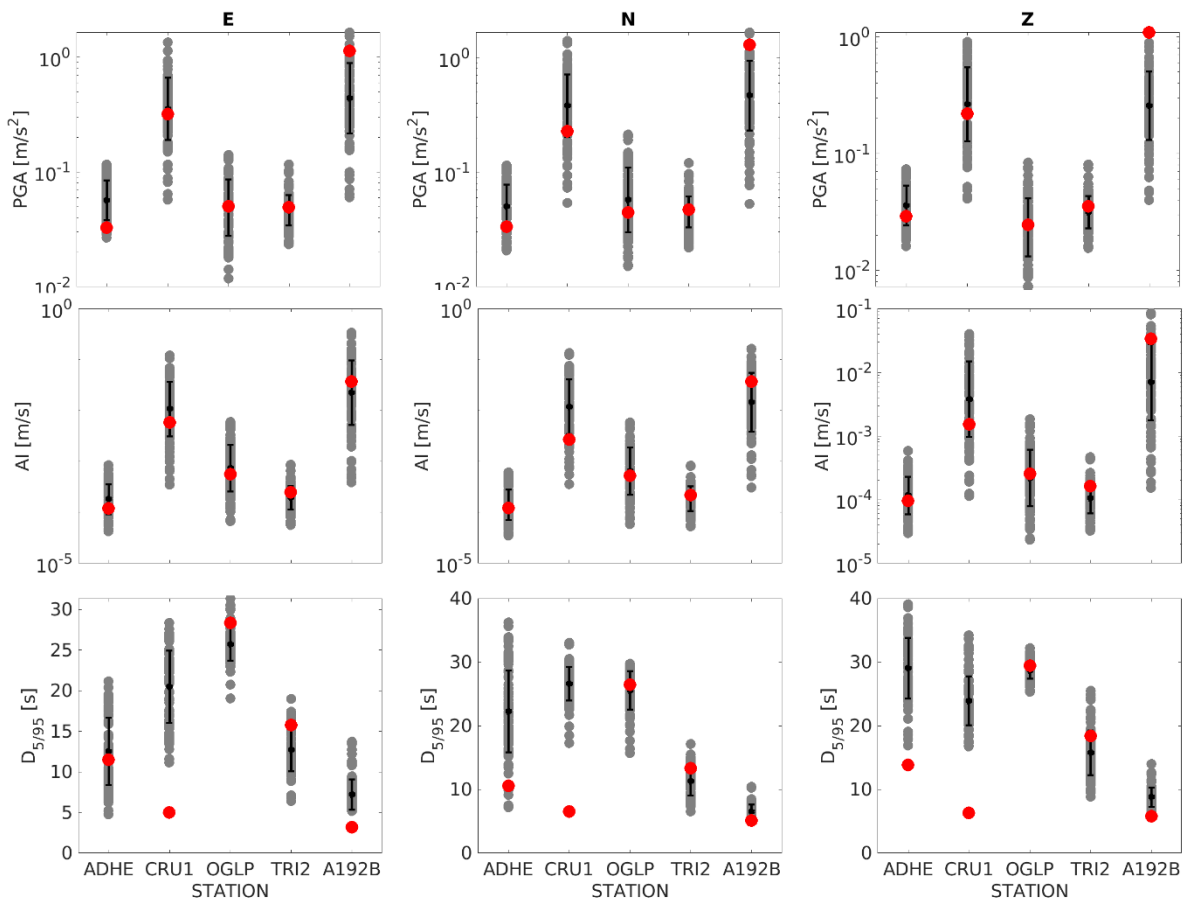


Figure 25: The PGA, Arias Intensity and Duration obtained from the 100 simulations generated by varying at the same time: the stress drop, the rupture speed and the position of the nucleation on the rupture plan (for each GM intensity measure, a grey dot represents the output of one simulation, at one station and in one direction). The error bars correspond to the average  $\pm 1\sigma$  of the 100 simulations. The red dots correspond to the results of the recorded accelerograms for the Le Teil earthquake.

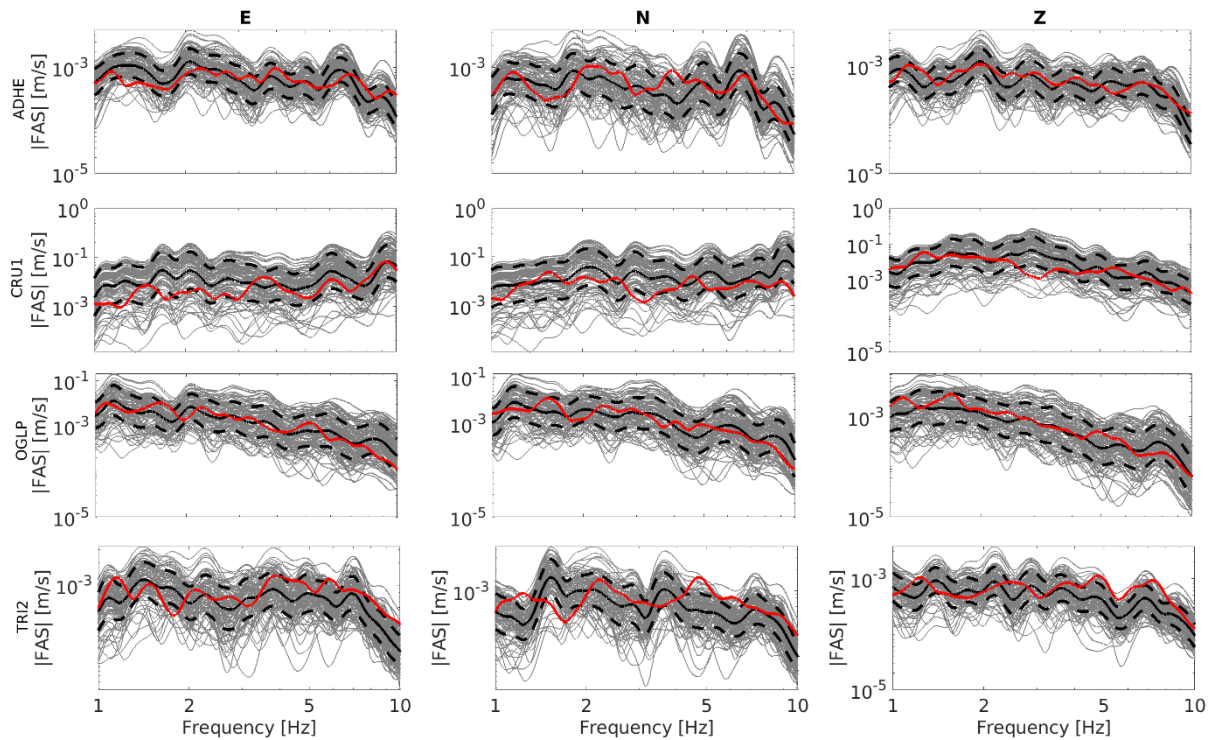


Figure 26: The Fourier Amplitude Spectra (FAS) calculated from the 100 simulations generated by varying at the same time: the stress drop, the rupture speed and the position of the nucleation on the rupture plan (each grey curve represents the output of one simulation, at one station and in one direction). The black curves correspond to the average  $\pm 1\sigma$  of the 100 simulations. The red curves correspond to the FAS of the recorded accelerograms for the Le Teil earthquake.

From the 100 simulations, we chose the simulation corresponding to the minimum misfit between the simulated and recorded outputs. The source input parameters of the chosen simulation are listed in Table 6. Compared to the benchmark simulation, the stress drop is almost the same, however, the rupture velocity shall be 1600 m/s instead of 1800 m/s to have a better prediction of the Le Teil earthquake.

Table 6: The source parameters of the simulation that fits the best the results of the recorded accelerograms for the Le Teil earthquake compared to the initial simulation of the benchmark.

Input parameters	Minimum misfit simulation	Benchmark simulation
Stress drop ( $\Delta\sigma$ )	1.9 MPa	2 MPa
Rupture speed ( $V_{rup}$ )	1600 m/s	1800 m/s
Xnuc	69%	51%
Ynuc	88%	59%

Figure 27 shows the static slip distribution and the moment rate amplitude function of the simulation that fits the best the recorded data. Compared to the benchmark simulation, the slip distribution is globally the same: two slip patches with a maximum slip of almost 30 cm. However, the nucleation position in the new simulation is shifted slightly toward the lower right corner of the rupture area.

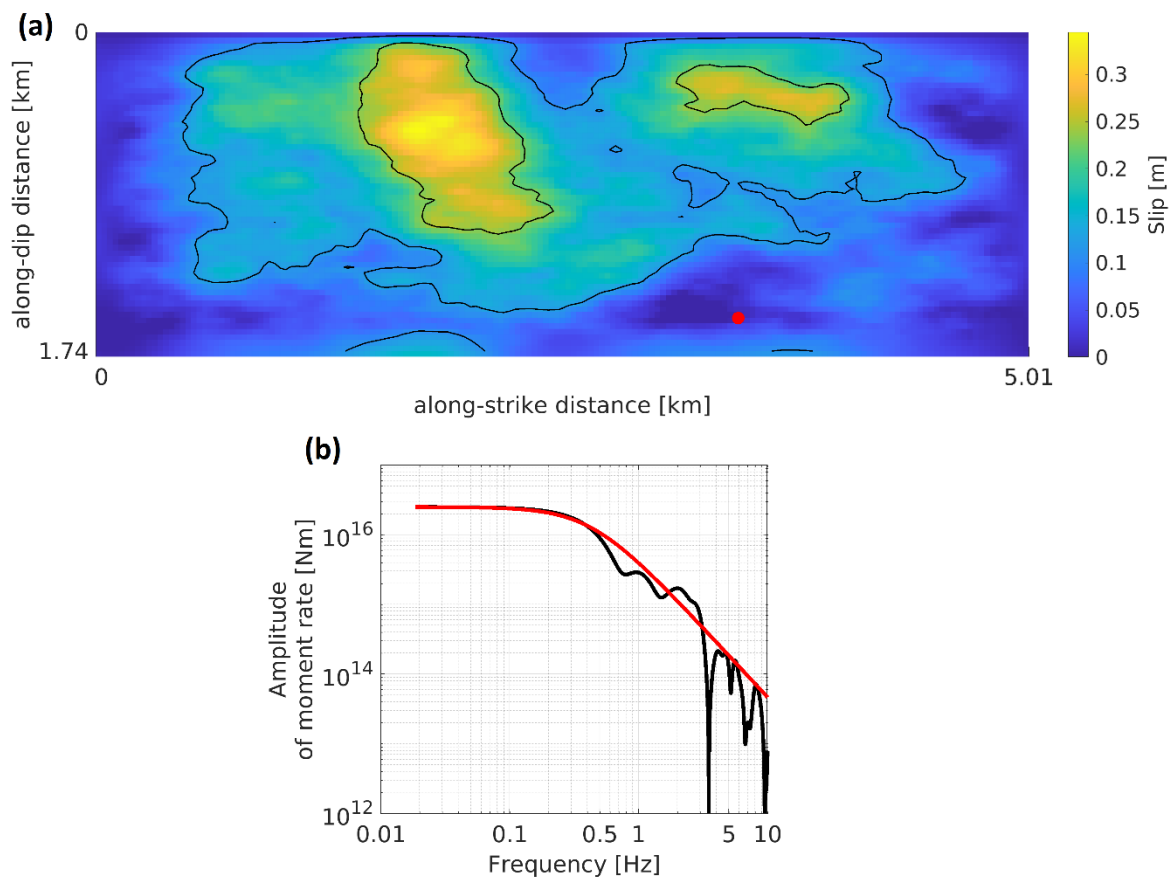


Figure 27: The static slip distribution (a) and the moment rate amplitude function (b) of the simulation that fits the best the results of the recorded accelerograms for the Le Teil earthquake.

### 3.2.3.2 EGF characteristics' variability

In this sensitivity study, the impact of EGF's properties on the output parameters is analyzed. To do so, four parameters defining the EGF are modeled as random variables: The magnitude of the EGF defined by  $M_w$ , the stress drop of the EGF ( $\Delta\sigma$ ), the strike and the dip. The histograms of the four EGF's parameters are represented in Figure 28. Except for the stress drop, a uniform distribution is used to define  $M_w$ , strike and Dip of the EGF.

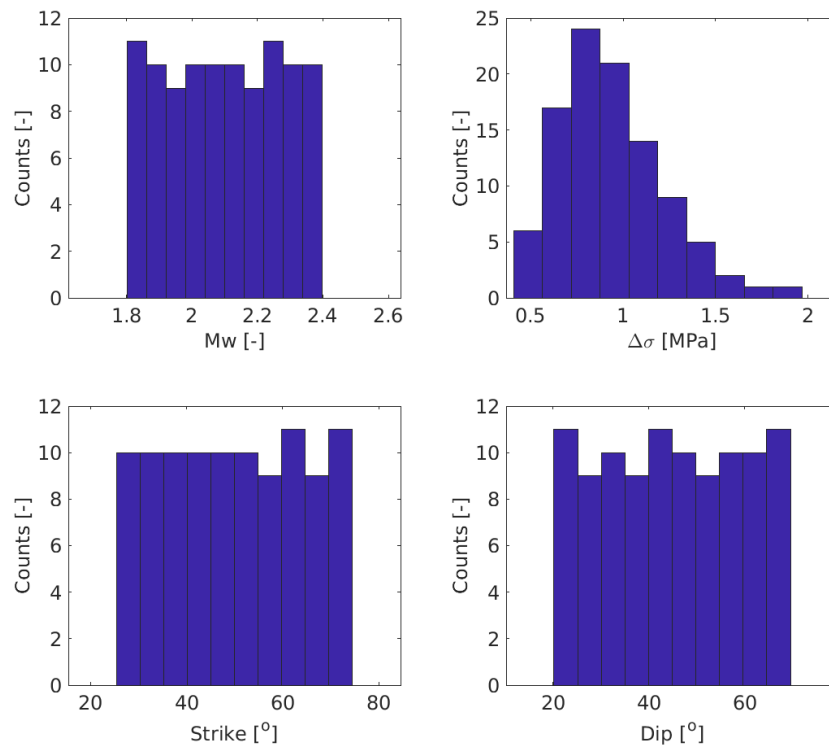


Figure 28: The histograms of the random variables defining the EGF's properties: Magnitude ( $M_w$ ), stress drop ( $\Delta\sigma$ ), the strike and the dip.

Similarly to the previous sensitivity study, the variability coefficient  $\alpha$  is calculated for the four GM intensity measures at five stations and for the three components (Figure 29). The results show that the magnitude of the EGF's is the input parameter controlling the simulations results. Besides, the Arias Intensity is the ground motion parameter with the highest sensitivity to the variability of the EGF source parameters.

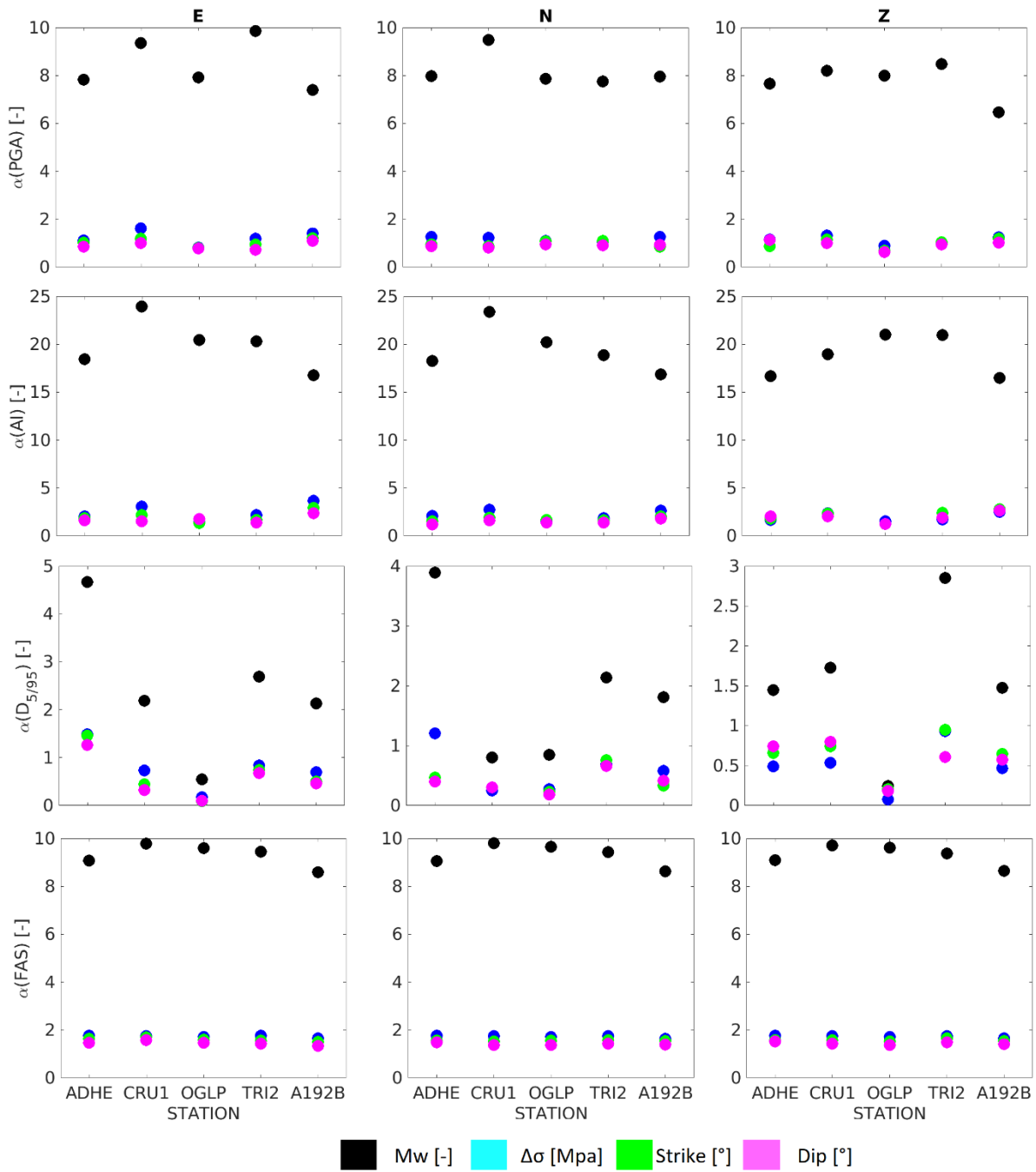


Figure 29: By varying the EGF's properties, the variability coefficient  $\alpha$  for the five ground motion intensity measures: PGA, Arias Intensity, Duration and FAS estimated for the five stations: ADHE, CRU1, OGLP, TRI2 and A192B.

### 3.2.4 Recap on Dujardin modified technique

The Dujardin et al (2020) modified method is an empirical simulation technique that generates static slip distribution and moment rate function for a target event and predict the ground motion at a specific location by convolving the moment rate with a local Green's Function. The Green' function is estimated (i) using the recordings of small earthquakes occurred in the same region of target event; (ii) deconvolving by a theoretical source function and (iii) applying attenuation, geometry and radiations corrections.

For the Le Teil earthquake case study, the two aftershocks with a magnitude larger than two are used to simulate the ground motion at five stations. These stations are stations that recorded the main event and the two aftershocks.

The results show that the slip distribution estimated by Cornou et al. (2020) doesn't fit a Brune (1970) model and doesn't allow to reproduce the main event especially for high frequencies. The slip distribution fitting the theoretical Brune (1970) model allows to better predict the ground motion parameters. However, the results depend on the analyzed output parameter, station and direction. The Signal to Noise Ratio and the frequency contents of the used EGFs have an impact on the output. Further analyses are needed to understand the impact of the EGFs choice and EGFs properties on the results.

Moreover, the impacts of the source parameters' variability and the EGFs properties' variability are analyzed by doing two sensitivity studies. The stress drop of the target event and the Magnitude of the EGFs are the parameters controlling the most the simulation's output. Thus, the magnitude of the small events shall be well defined to obtain a better ground motion prediction by using this type of techniques. Besides, some parameters are more sensitive than others to the variability of the input. For example, the Arias Intensity exhibits a larger sensitivity compared to the sensitivity of the PGA, Duration and FAS.

Finally, even though the results obtained for the Le Teil case study are interesting, this simulation's technique has many weaknesses that will be discussed in section 5 of this study.

## 4 Physics-based simulations

### 4.1 Finite fault 1D simulations

In this part, ground shaking is calculated through the tensor product between the tensors of the earthquake source and the Green's function of the medium (including the soil layers) crossed by the seismic waves (Fasan, 2017; Magrin, 2012; Panza et al., 2012). Seismic waves are modelled starting from the knowledge of the seismic source and of the structural properties of the earth's lithosphere, allowing to take into account the kinematic complexity of the rupture process of the seismic source as well as site and path effects and, thus, considering the intra and inter-event spatial variability of the ground motion. The technique herein presented has been successfully applied and validated against past events and available ground motion prediction equations (Fasan, 2017; Fasan et al., 2016; Hassan et al., 2020; Magrin et al., 2016; Panza et al., 2012).

In order to assess the ground shaking associated with the Le Teil seismic scenario, the calculation of synthetic accelerograms is done in two phases:

1. simulation of the fault rupture process on the fault plane;
2. simulation of wave propagation and calculation of synthetic accelerograms for the sites of interest.

In this technique, it is therefore necessary to know accurately:

- the properties of the seismic source;
- the deep structure (crustal model) of the medium interposed between the fault and the sites of interest;
- the local soil stratigraphy;
- the attenuation (quality factor  $q$ ) of the above mentioned structures.

#### 4.1.1 Source model

To calculate realistic accelerograms, in particular in the near fault zone, a finite-fault simulation is needed. An extended source (ES) model allows to catch the effects related to the kinematic rupture process (i.e. directivity) and, in the near field, to the dislocation (i.e. static displacement - fling step).

When the extended model is used, the source of the earthquake is considered a relative slip field distributed on the fault surface, on which the rupture process is presumed to occur.

In this part the simulation of the fault rupture is first performed by the algorithm PULSYN as implemented by Gusev (Gusev, 2011).

The fault surface is modelled as a grid of point sub-sources, whose seismic moment is calculated by considering each of them as a component of a realization of a non-stationary random process. Assuming a realistic kinematic description of the rupture process, the extended seismic source model allows to generate a spectrum (in amplitude and phase) of the temporal function of the source that takes into account both the rupture process and the effects of directivity.

For the purpose of the benchmark, as described in section 3.1.3.1, four slip distributions were derived from Cornou et al. 2021 and DeNovellis et al. 2021, namely Cornou LF, Cornou HF, DeNovellis LF and DeNovellis HF. The deterministic source parameters adopted for Cornou models are described in section 2.2 and includes: moment magnitude, fault dimensions and position, mean rupture velocity, nucleation point position. Differently from Cornou models, in the DeNovellis models the fault has a length a 5km and a width of 1.9km. The moment magnitude, nucleation point location and mean rupture velocity are assumed to be the same as in the Cornou models whereas strike, dip and rake were taken as: 50°, 62° and 116°. The simulated slip distribution are shown in Figure 30.

When modelling possible future seismic scenarios, no reasonable deterministic prediction for many details of a future fault motion can be expected. Therefore, the variability of the space and time evolution of the rupture can be treated in practice only from a statistical viewpoint. Correspondingly, the simulation

of the fault rupture can be performed by the algorithm PULSYN through a Monte-Carlo approach as implemented by Gusev (Gusev, 2011). The methodology applied is a broadband kinematic stochastic simulation of the earthquake source. At low frequency the fault process is described deterministically, in terms of fault slip rate as a function of time and position on a fault. At higher frequencies (HF), which are mostly controlled by details of the propagating rupture, the fault process is treated in a stochastic manner.

For the chosen scenario, different possible realizations of the rupture process can be considered. Each realization is characterized by a different slip distribution on the fault plane, nucleation point and time evolution. In this way the stochastic nature of the fault rupture is accounted.

The simulation of the detailed space-time history of the source performed by the PULSYN algorithm can be briefly described as follows (Gusev, 2011; Magrin, 2012):

1. For a given moment magnitude  $M_w$ , the seismic moment value  $M_0$ , the length and width of the source rectangle, and mean rupture velocity (that defines the duration) are selected following average observed trends (Kanamori and Anderson, 1975; Wells and Coppersmith, 1994). In case of a deterministic simulation these parameters are fixed;
2. Step 1 guarantees that the low-frequency part of the source spectrum will have a realistic corner frequency, and that the far-field body-wave source signal will have realistic duration. Non-standard stress-drop values can be consistently accounted for. The simulated sub-sources are positioned in a grid pattern over the rectangle. Amplitudes of sub-sources are selected following a simulated distribution of the final slip. This 2D slip function is assumed to be a realization (sample function) of a 2D random process with an appropriate (power-law) power spectrum. In a deterministic simulation the slip distribution can be imposed.
3. A predetermined nucleation/starting point ("hypocentre") within the rectangle is set, and the rupture front is assumed to propagate from this point, with a given velocity field for its kinematic simulation (e.g. unilateral, symmetric bilateral). The rupture front velocity is assumed to vary randomly along the distance from the hypocentre. The successive velocity values are randomly distributed, with predetermined mean and dispersion. The arrival of the front at a sub-source switches it on;
4. Each sub-source is assumed to slip (that is, to have non-zero slip velocity) only during its "active" time interval, with its duration comparable to the standard "rise time" parameter of Haskell-Aki-Heaton model (Aki, 1967; Haskell, 1964; Heaton, 1990). The rise time is assumed to be similar in all points over the source rectangle and it is selected following Heaton's result that the width of the slipping part of the fault is approximately the 10% of its length. Thus, the rise time is set as a fraction (like 0.10) of the total rupture propagation time for the unilateral rupture case. To account for finiteness of sub-sources, this "ideal" rise time is then somewhat increased. The complete solution of the entire problem is reduced now to the construction of appropriate time functions of moment rate for each sub-source.
5. The "target" amplitude source spectrum is defined on the basis of a preferred theoretical or empirical spectral scaling law. The aim of the subsequent calculations is to construct a signal whose spectrum is close to the target one. Let us consider the "skeleton source", or the space-time object that consists of all white-noise sequences present in each sub-source. The far-field radiation of this source will have quite realistic spectral properties at low frequencies, because the general style of the space-time source behaviour and its numerical parameters are chosen to be realistic. At high frequencies (HF), however, the signal will be too rich in high frequency energy. To fit the HF part of the target spectrum, smoothing of the "skeleton" signal must be performed. A simple way to do such a smoothing is to convolve the white-noise sequences with a pulse of an appropriate shape. To determine such a shape function we compare the far-field amplitude spectral shape of the "skeleton" signal generated by the complete set of white-noise signals, on one side, and the realistic "target" amplitude spectral shape on the other side. Roughly speaking, the ratio of these spectra is calculated and then transformed to the time

domain, yielding the appropriate pulse shape. The actual procedure is more complicated, since it includes the smoothing of the high-frequency part of the “skeleton” spectrum, and the accurate selection of the phase spectrum of the unit pulse. The resulting smoothing kernel represents a relatively short “unit pulse”.

6. As a final step, for each sub-source its skeleton time history is shifted in time, by a delay corresponding to the rupture propagation kinematics, and then convolved with the common unit pulse, to produce the moment rate time function of this sub-source.

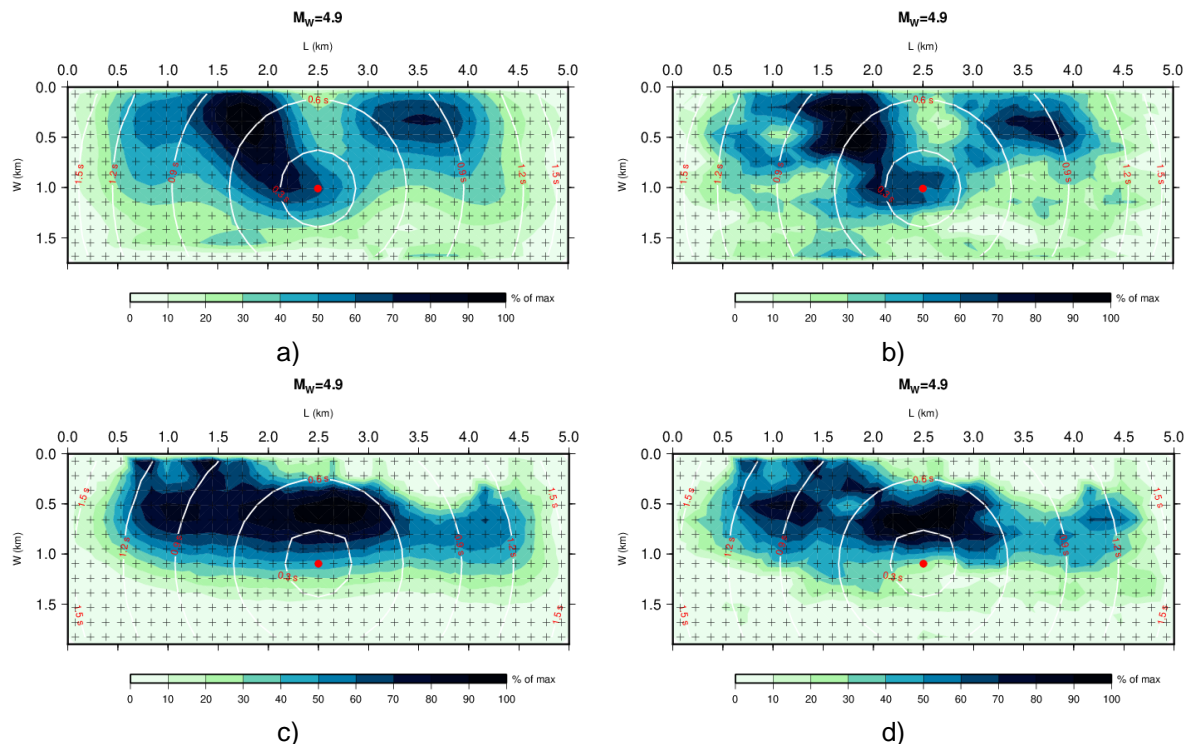


Figure 30: Simulated deterministic rupture process for the Le Teil event: a) Cornou LF, b) Cornou HF, c) DeNovellis LF, d) DeNovellis HF. The darker areas correspond to a high slip on the fault while the red dot shows the nucleation point of the rupture. The white isochores describe the time evolution of the rupture process.

#### 4.1.2 Wave propagation model

The seismograms calculation is conducted in laterally homogeneous media, i.e. the bedrock-soil structural model is represented by a semi-infinite space in plane and parallel inelastic layers, up to a frequency of 10 Hz and using two different techniques: the MS - modal summation technique (Panza, 2001; Panza et al., 2012) and the DWN - discrete wavenumber technique, following the implementation of Pavlov (Pavlov, 2009). The modal summation technique (MS) is very fast and provide an accurate simulation of ground motion in far field condition, but it can be applied only when the epicentral distance is greater than the focal depth. The DWN gives the full wave field, including all body waves and near field ground motion and is applied when MS is not applicable.

Propagation modelling needs to account for path and site effects. In order to accurately account for these effects the medium crossed by waves and the local soil stratigraphy should be provided. The structures assumed to be representative of the four recording stations (CRU1, OGLP, ADHE, TRI2) recording stations are shown from Figure 31 to Figure 33. **Erreur ! Source du renvoi introuvable.** For each layer the information needed are:

- density;
- shear and longitudinal velocities;
- attenuation factor;

- thickness.

The crustal model proposed by Causse et al. (2021) was assumed. As for the superficial layers, details are lacking. Few information has been obtained only for CRU1 and OGLP stations. For ADHE and TRI2 the crustal model has been assumed representative of the whole structure beneath the stations. For the attenuation model the quality factor was assumed to be 1/10 of the shear wave velocity.

It is clear that an accurate description of the soil structure plays a crucial role on the accuracy of physics-based simulations since, even at short distances from the fault, important features of the ground motion such as amplified frequencies, amplitudes, duration depends strongly on these parameters. This is particularly important at high frequency.

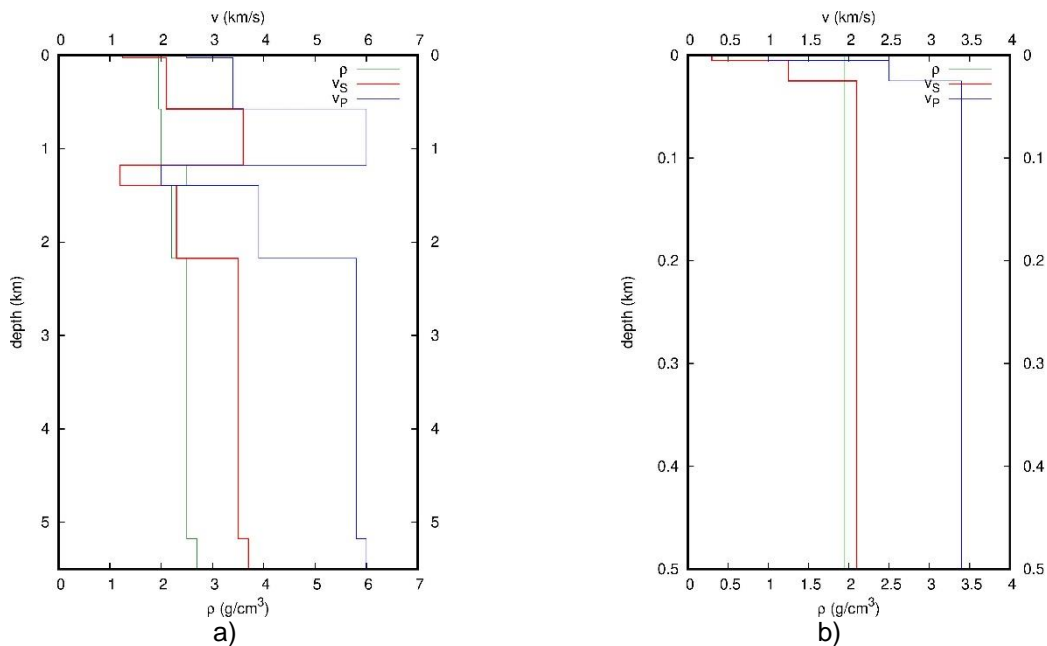


Figure 31: structure adopted for CRU1 station: a) profile up to 5.5km, b) profile up to 0.5km

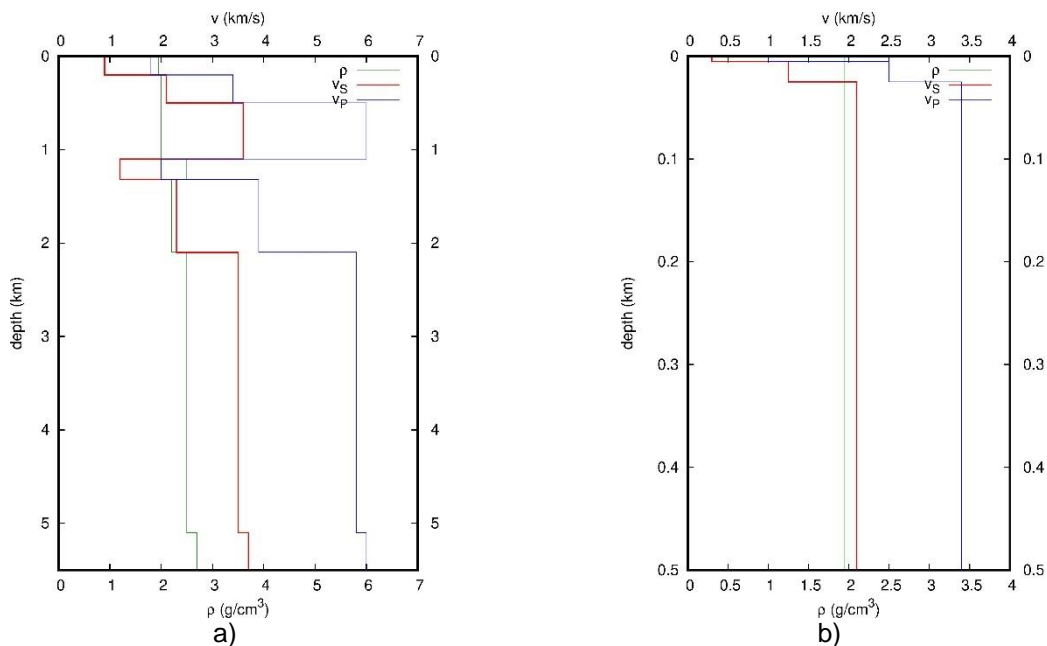


Figure 32: structure adopted for OGLP station: a) profile up to 5.5km, b) profile up to 0.5km

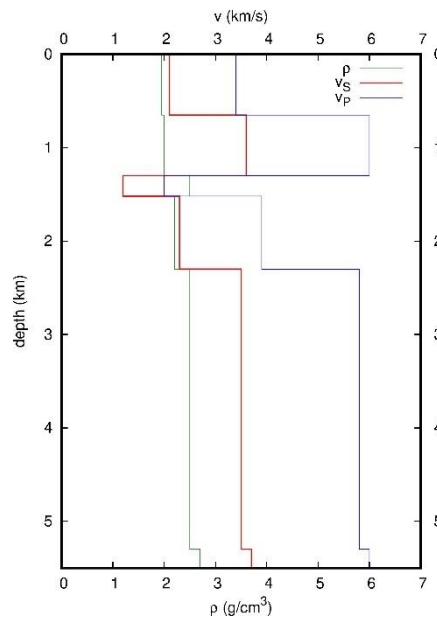


Figure 33: structure adopted for ADHE and TRI2 stations.

#### 4.1.3 Variability from random simulations, results and discussion

The results for the deterministic simulation and comparisons between different techniques are presented in section 5. Here only results for five hundred stochastic simulations of the rupture process are presented. Varying parameters are: slip distribution, mean rupture velocity, nucleation point, rupture front evolution. Moment magnitude and fault dimensions were set as described in section 2.1 according to the Cornou model. Soil structures for the different recording stations are those shown from Figure 31 to Figure 33.

Comparison between observed and simulated values are reported for PGA, arias intensity AI, significant duration (D95 and D70, respectively the time from 5% to 95% and to 5% to 70% of Arias Intensity) are shown from Figure 34 to Figure 37. The comparisons are reported for the three ground motion components and for the RotD100 component (here called res). In the comparisons observed signals are filtered to a maximum frequency of 10Hz. Comparisons are also reported for spectral accelerations reporting the GOF, evaluated as in equation 3.1.6, between simulated and recorded values at different periods. Spectral acceleration comparisons are shown in

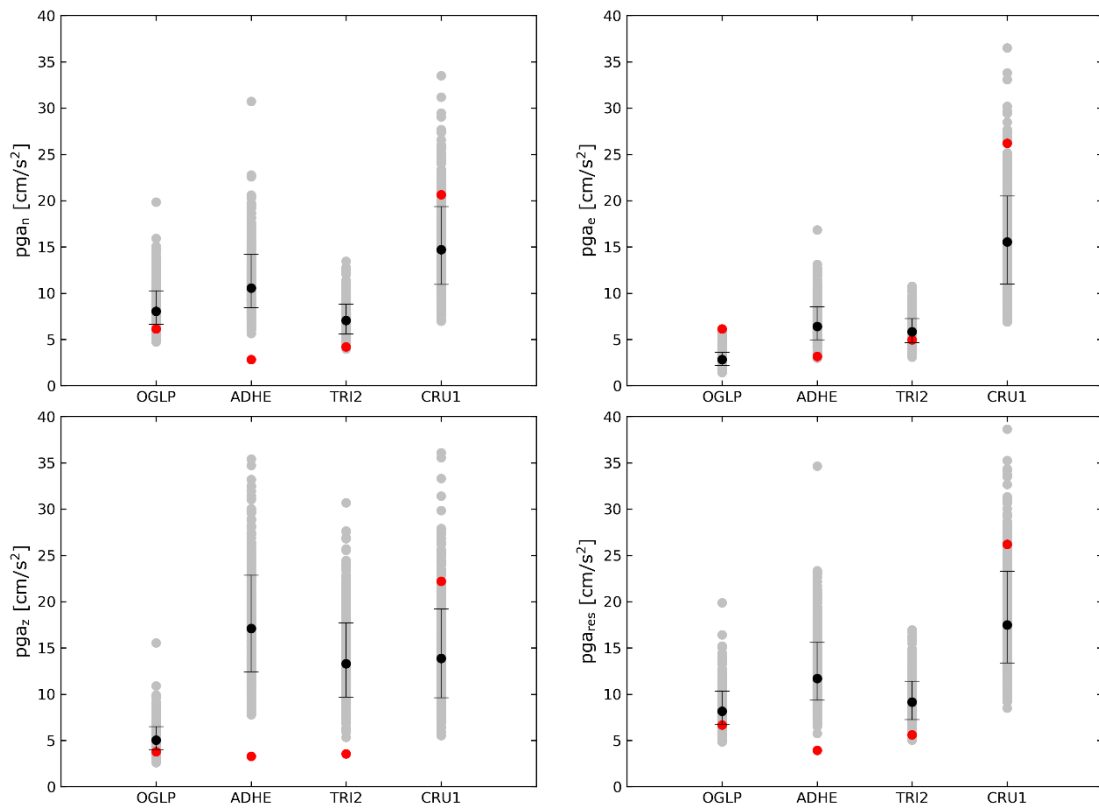


Figure 34: PGA comparison. red dot represents the observed value, black dot the median from simulations, the two bars plus/minus one standard deviation, grey dots the values of each simulation

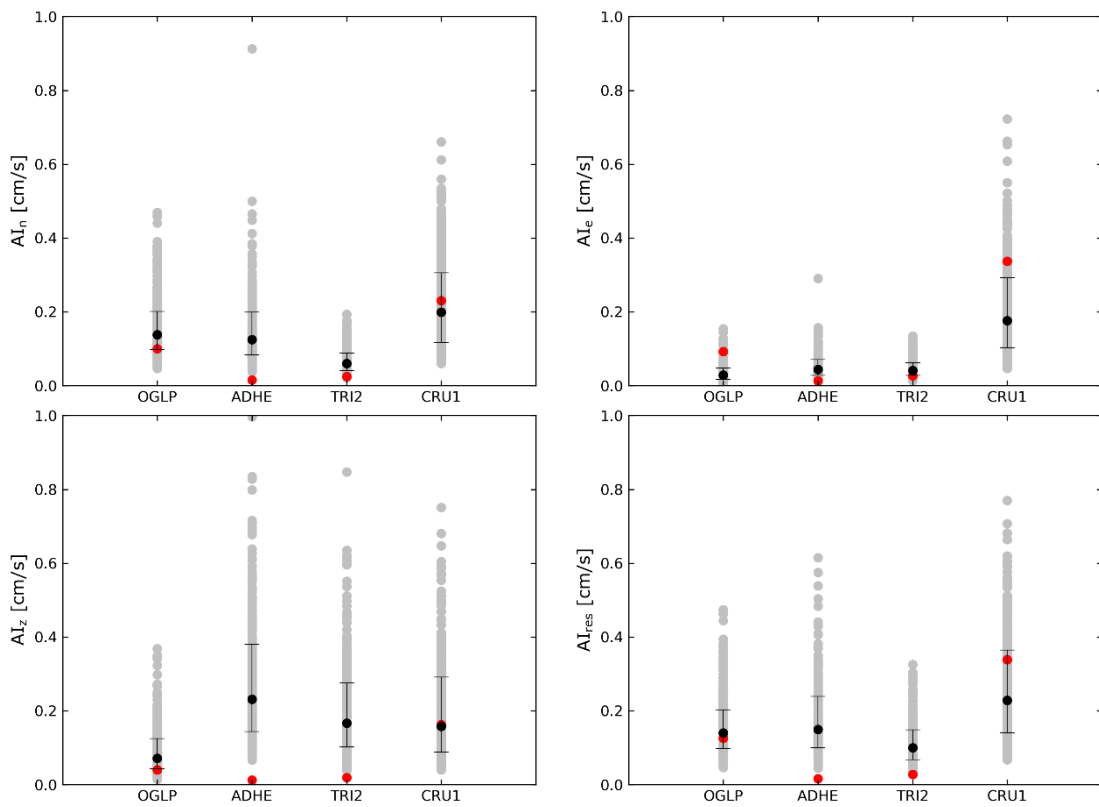


Figure 35: Arias Intensity comparison. red dot represents the observed value, black dot the median from simulations, the two bars plus/minus one standard deviation, grey dots the values of each simulation

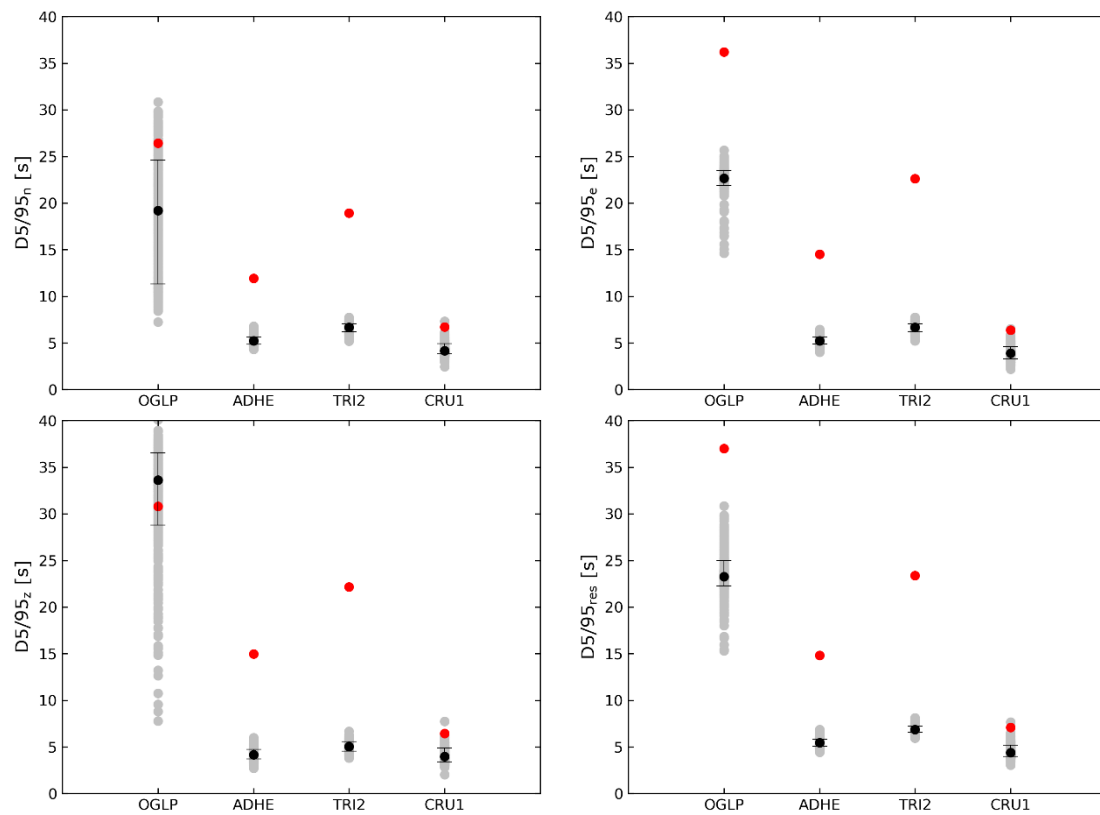


Figure 36: Significant Duration (D5/95). red dot represents the observed value, black dot the median from simulations, the two bars plus/minus one standard deviation, grey dots the values of each simulation.

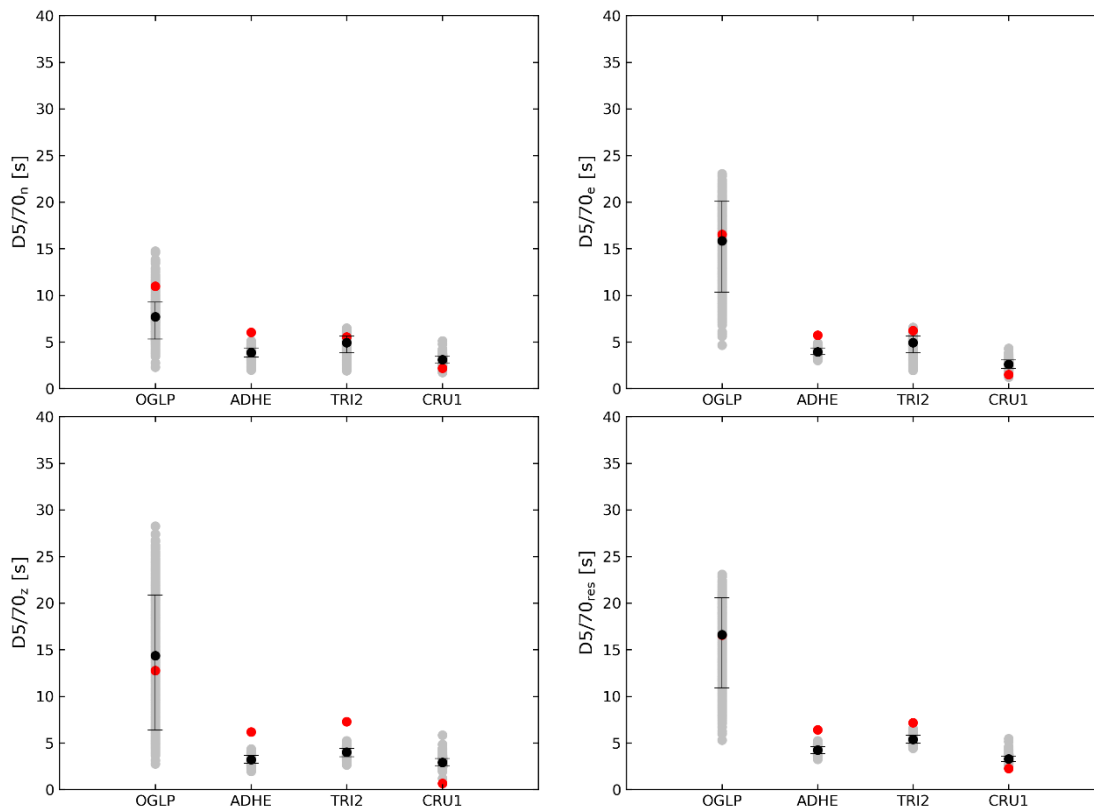


Figure 37: Significant Duration ( $D7/70$ ). red dot represents the observed value, black dot the median from simulations, the two bars plus/minus one standard deviation, grey dots the values of each simulation.

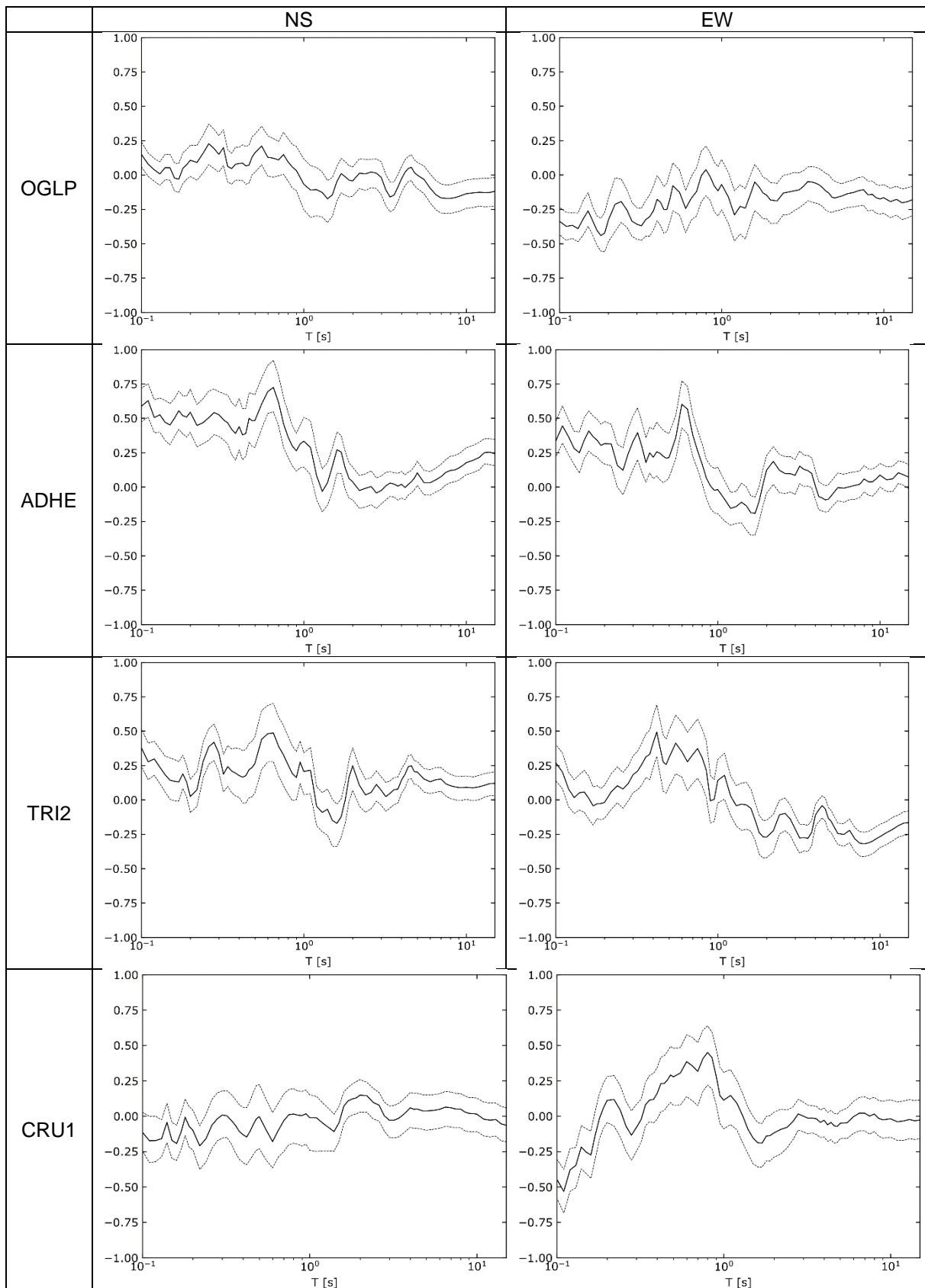


Figure 38: GOF for spectral accelerations: the black line is the median value whereas the dashed lines represent the 16<sup>th</sup> and 84<sup>th</sup> percentiles (left NS component, right EW component)

From the comparisons it can be seen that the rupture processes (the only source of variability considered here) have a significant impact on results. The comparisons show good performances for OGLP and CRU1 stations whereas the discrepancies with observed values are higher for TRI2 and ADHE stations. Arias Intensity and D5/70 show a good match with observations implying that the energy content of the simulated accelerograms is compatible with the event characteristics.

The worse performances of TRI2 and ADHE could be due to the lack of an accurate estimation of the medium parameters, in particular thin superficial soil layers with low velocity and high attenuation could be responsible of some local effects (long duration and low amplitudes with dispersion of energy). This seems to be confirmed by the fact that stations where data on stratigraphy are available (OGLP and CRU1) are those where results are more accurate. Moreover, GOF for spectral accelerations show that performances are better at long periods where local details about soil stratigraphy play a less crucial role.

Furthermore, compared to the fault position, OGLP and CRU1 are the ones where the hypothesis of a laterally homogeneous medium seems to be more realistic. In fact, TRI1 and ADHE are placed on the other side of the basin with respect to the fault position and therefore these stations could suffer more from 3D propagation effects due to lateral heterogeneities that cannot be accounted for by 1D simulations.

## 4.2 3D simulations

The 3D physics-based simulations of the  $M_w$  4.9 Le Teil earthquake have been carried out using the open-source high-performance computer code SPEED (<http://speed.mox.polimi.it/>, Mazzieri et al., 2013).

The set-up of a 3D numerical model requires the knowledge of the main geological, geotechnical and geophysical information of the region to be investigated (in this case, an area of about 50 x 70 km, centered around the epicenter of the event) as well as the characterization of the seismo-tectonic setting (active seismic sources). A high frequency resolution numerical model was built in order to propagate frequencies up to about 8 Hz. Such high resolution was tested with SPEED, varying the spectral degree order of the polynomials.

This chapter, after a brief introduction of the numerical approach used in SPEED, shows the set-up of the model, including the reconstruction of the 3D geometry of the Rhône river valley and the definition of the velocity model, and the main computational features of the simulation. Then, main results are presented by addressing the following aspects: (i) testing of model high frequency resolution; (ii) verification of SPEED model against an independent code (Hisada); (iii) sensitivity analyses with respect to the subsoil model (1D Vs 3D) as well as to the source model; (iv) validation of simulations against the available recordings.

### 4.2.1 The numerical code SPEED

SPEED - SPectral Elements in Elastodynamics with Discontinuous Galerkin (<http://speed.mox.polimi.it/>) - is an open-source high-performance computer code, jointly developed at Politecnico di Milano by the Department of Civil and Environmental Engineering and the Department of Mathematics. It belongs to the class of highly-accurate numerical methods for the solution of elastodynamics problems in heterogeneous media.

SPEED is designed to perform the large-scale numerical simulation of three-dimensional seismic wave propagation including, in a single computational domain, the seismic source, the propagation path and local site response features (Mazzieri et al. 2013).

Based on the Discontinuous Galerkin Spectral Element (DGSE) formulation for space discretization (Antonietti et al. 2012), the code enjoys the accuracy features of Spectral Elements (Faccioli et al. 1997) and the flexibility of Discontinuous Galerkin approaches to handle non-matching grids (h-adaptivity) as well as variable approximation orders (N-adaptivity). SPEED heavily exploits parallelism in the framework of explicit time integration and features optimal scalability properties making use of the open-source libraries METIS and MPI for mesh partitioning and message passing.

The main features of the code SPEED, relevant for earthquake seismology applications (such as those related to the source representation, soil constitutive models, amongst others), are summarized in

Table 7.

SPEED is equipped with pre- and post- processing tools (3PTOOL) suitable, on one side, to generate the input files for arbitrary finite-fault earthquake scenarios and, on the other side, to post-process the SPEED results, limited to the low-frequency range (typically below 2 Hz), to produce broadband ground motions and shaking maps, according to the workflow presented in Figure 39. Broadband ground motions can be generated by means of a technique which relies on Artificial Neural Networks (ANN2BB), trained on strong ground motion recordings, in order to provide a correlation between long and short period spectral ordinates (Paolucci et al., 2018).

The code has been verified over different benchmarks, including that of Grenoble (Stupazzini et al., 2009) and the SCEC benchmarks, as well as validated thoroughly against Italian and worldwide earthquakes. An overview of the most relevant applications of SPEED is provided in Table 8. Very recently, a dataset of broadband ground motions from SPEED simulations has been published (Paolucci et al. 2021b, see <http://speed.mox.polimi.it/bb-speedset/>).

Table 7: Main features of SPEED code for engineering seismology applications.

<b>Mesh strategy</b>	Conforming (SEM) or non-conforming (DGSEM) with first-order absorbing paraxial boundary conditions
<b>Time integration</b>	<ul style="list-style-type: none"> <li>- explicit second-order accurate leap-frog scheme</li> <li>- explicit fourth-order accurate Runge-Kutta method</li> </ul>
<b>3D material discontinuities</b>	Not-Honoring approach (node-by-node) or DG approach
<b>Soil constitutive models</b>	Linear and non-linear visco-elastic behavior with damping models: (a) <ul style="list-style-type: none"> <li>- Hysteretic (frequency independent);</li> <li>- frequency-proportional</li> <li>- Rayleigh damping.</li> </ul> Non-linear visco-elastic model described by modulus reduction and damping curves.
<b>Source representation</b>	<ul style="list-style-type: none"> <li>- Plane wave propagation</li> <li>- Kinematic finite-fault modelling with two rupture generators (Herrero and Bernard 1994; Schmedes et al. 2012) for both simple (planar, one-segment) and complex (multi-segment, non-planar) fault systems</li> <li>- Dynamic finite-fault rupture modelling</li> <li>- Travelling point loads (train-induced vibrations)</li> </ul>

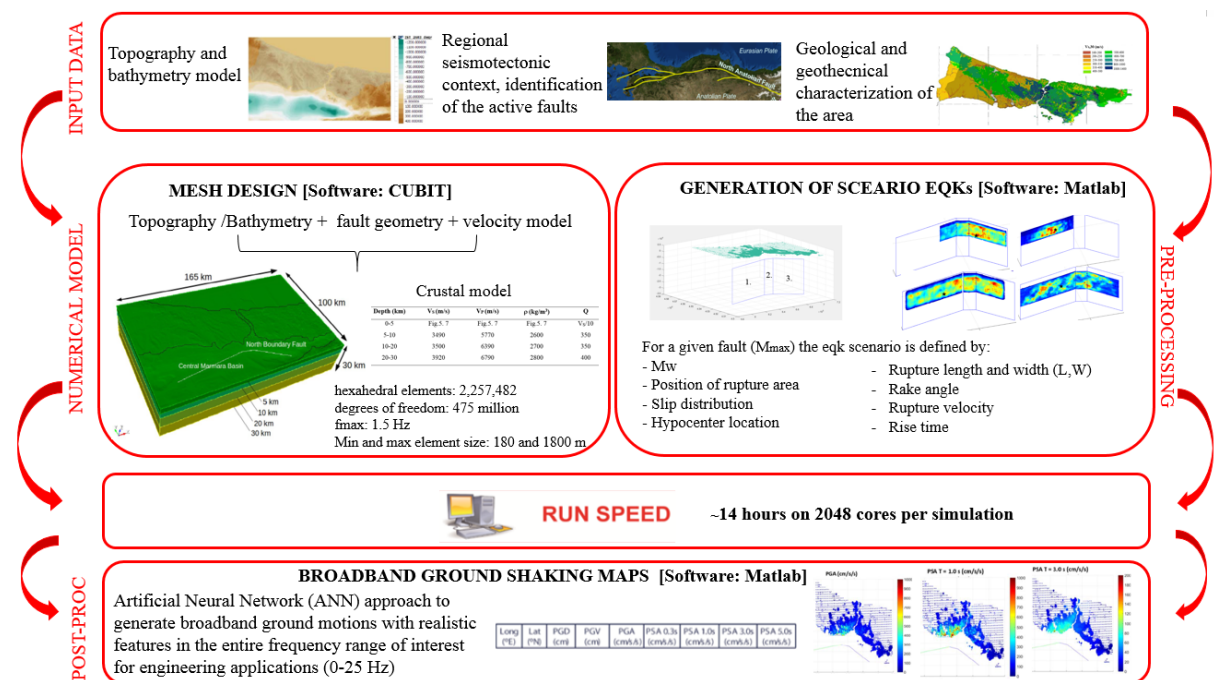


Figure 39: Workflow for 3D physics-based simulations using the SPEED code.

Table 8: List of simulation case studies, including validations of real earthquakes and scenario simulations, in Italy and in the rest of the world.

Case Study	Fault (SoF)	Mw	Model size (km <sup>3</sup> )	f <sub>max</sub> (Hz)	Validation (V)/Scenario(S)	References
Grenoble, France	Belledonne (SS)	6.0	41x50x8	3	V: Benchmark	Stupazzini et al. (2009)
Gubbio plain, Italy	Colfiorito (NF)	6.0	85x62x10	3	V: 26 Sept 1997	Smerzini et al. (2011)
Tagliamento plain, Italy	Gemona Faults (TF)	6.1	57x53x12	2.5	V: 15 Sept 1976	Smerzini (2010)
L'Aquila, Italy	Paganica (NF)	6.2	58x58x20	2.0	V: 6 Apr 2009	Evangelista et al. (2017)
Sulmona, Italy	Mt. Morrone (NF)	6.0	49x42x13	2.5	S(#10)	Villani et al. (2014)
		6.5			S(#10)	
Christchurch, New Zealand	Lyttelton (TF)	6.3	60x60x20	2.0	V: 22 Feb 2011	Guidotti et al. (2011)
Po Plain, Italy	Mirandola (TF)	6.0	74x51x20	1.5	V: 29 May 2012	Paolucci et al. (2015)
Marsica, Italy	Fucino (NF)	6.7	56x46x20	2.0	V: 13 Jan 1915	Paolucci et al. (2016)
Thessaloniki, Greece	Gerakarou (NF)	6.5	82x64x31	1.5	V: 20 Jun 1978	Smerzini et al. (2017)
	Anthemountas (NF)	7.0			S(#1)	Smerzini et al. (2018)
Norcia, Italy	Mt. Vettore-Mt. Bove (NF)	6.5	50x40x21	1.5	30 Oct 2016 + S(#7)	Özcebe et al. (2019)
		5.8			S(#1)	
		5.5			S(#1)	
Wellington, New Zealand	Wellington–Hutt (SS)	7.1-7.2	60x56x26	1.5	S(#40 -#42)	On-going
		7.4-7.4			S(#25 - #14)	
Mexico City	NF	3.2	60x60x10	1	V: 17 July 2019	On-going
Santiago, Chile	San Ramon (TF)	5.2	97x77x19	2.0	V: 1 Apr 2010	Pilz et al. (2011)
		6.0			S(#1)	
		6.5			S(#1)	
		7.0			S(#1)	
Istanbul, Turkey	North Anatolian Fault Marmara Sea (SS)	5.7	165x100x30	1.5	V: 26 Sept 2019	Infantino et al. (2021); Stupazzini et al. (2021)
		7.0			S (#25)	
		7.2			S (#21)	
		7.4			S (#20)	
Beijing, China	Shunyi-Qianmen-Liangxiang (TF)	6.5	70x70x30	1.5	S (#15)	Antonietti et al. (2020)
		6.9			S (#10)	
		7.3			S (#5)	
Groningen, the Netherlands	NF (induced seismicity)	3.4	20x20x5	10	V: 8 Jan 2018	Paolucci et al. (2021a)
Kumamoto, Japan	Hinagu-Futagawa-Aso Caldera (SS)	7.0	53x46x22	1.5	V: 15 Apr 2016	Sangaraju et al. (2021)
	Hinagu-Futagawa (SS)	6.1			V: 14 Apr 2016	
	Aso Caldera (SS)	5.5			V: 15 Apr 2016	

#### 4.2.2 Set up of a 3D model: basin shape and velocity model

The construction of the 3D numerical model of the Montelimar area implied some preliminary analyses, in order to properly define the 3D geological model of the Rhône River Valley and the seismic wave velocity model of the valley sediments and of the crustal layers. An overview of the main assumptions behind the 3D model is given herein.

##### Geometry of the Rhône River Valley and set up a 3D basin shape

The numerical 3D model covers an area of about 50 km x 70 km around the epicenter of the earthquake, as indicated in Figure 40. The figure presents also the position of the accelerometric stations of the RESIF network (<http://seismology.resif.fr/>), falling inside the SPEED model, as well as of the two nuclear power plants, namely, Cruas plant (near the CRU1 accelerometric station), North to the epicenter, and the Tricastin plant, south to the epicenter. Information on the shape of the sediments inside the Rhône River Valley comes mainly from an available cross-section of the Valley, near the Tricastin NPP.

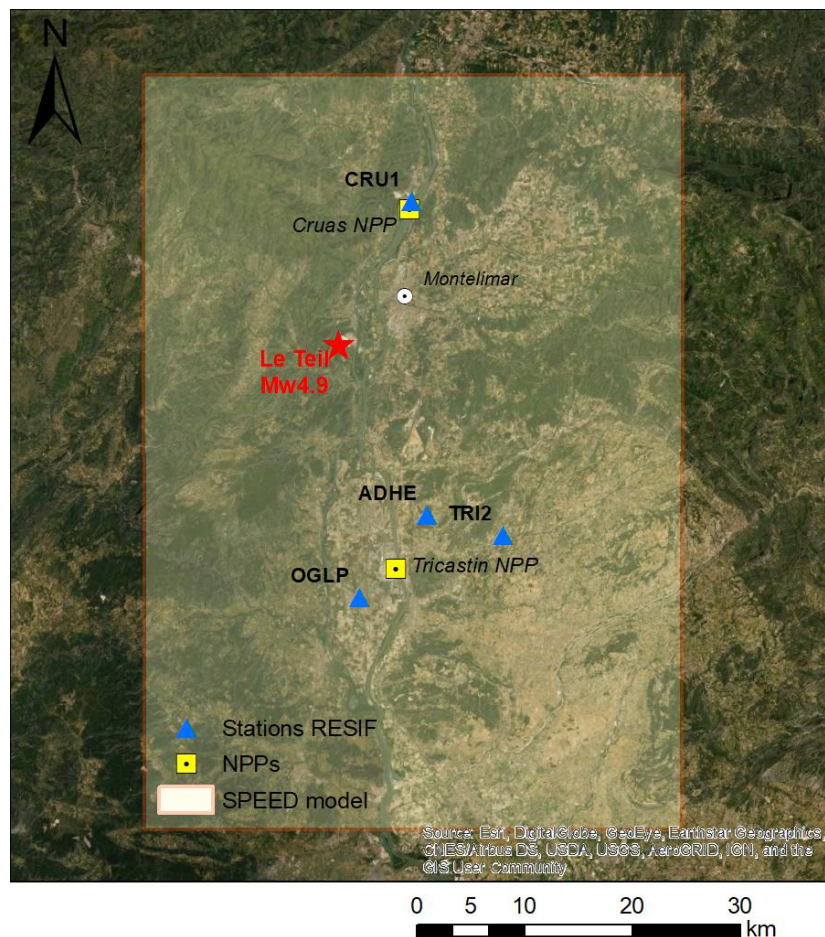


Figure 40: View of the Rhône River Valley in the vicinity of the epicenter of the earthquake (red star) with indication of the extent of the SPEED model (see superimposed box). The location of recording stations (blue triangles) as well as the two nuclear power plants (Cruas and Tricastin, yellow squares) is shown.

The 3D model of the shape of the Rhône River valley has been constructed from numerical processing of the information included in the DEM (Digital Elevation Model) of the area, available at <https://download.gebco.net/>, with a resolution of 300 m. To compute the depth of the Rhone Valley sediments, an ad-hoc algorithm was developed based on the equilibrium equation of an elastic and

homogeneous membrane (i.e., Poisson equation). The main steps of the algorithm can be summarized as follows:

- definition of a contour of the Rhone valley based on the morphology of the surrounding hills;
- creation of a polygonal domain starting from this boundary, meshed using triangular elements;
- computation of the distance to the boundary, for each internal grid point;
- solution of the Poisson equation using as a forcing term a distributed load inversely proportional to the boundary-point distance and setting as a Dirichlet boundary condition the point elevation.

The shape of the valley has been checked and refined using additional constraints, such as the maximum depth of the sediments (inferred from the available cross-section near Tricastin NPP) and a map of the sediments susceptible of site amplification (P. Traversa personal communication, May 2021). Figure 41 shows the final shape of the basin, adopted in the numerical model: note how the basin shape changes along the valley, being quite large and relatively deep near the Tricastin NPP and very narrow and shallow at the North, near the Cruas NPP. In the same figure, the area modelled in SPEED is also shown, together with the epicenter of the earthquake and the reference accelerometric stations.

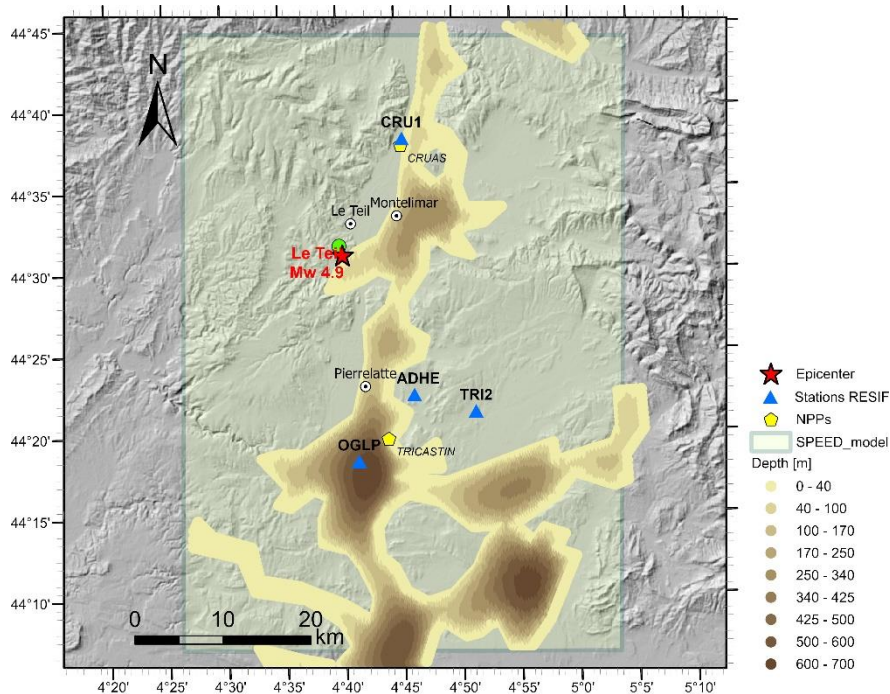


Figure 41: Basin model used in numerical simulations. The extent of the SPEED model is shown as a transparent yellow rectangle. Accelerometric stations of RESIF network are shown by blue triangles, yellow hexagons denote the NPPs of the area. The green dot near the epicenter is a site used for verification purposes (see section 4.2.6). Depth is measured with respect to the local topography.

#### Velocity model for crustal layers and basin sediments

Concerning the velocity model of the deep crustal layers, Table 9 shows the adopted geotechnical parameters, borrowed from Causse et al. (2020). These authors performed a set of numerical simulations of the Montélimar earthquake and characterized for that purpose the 1D structure of the earth crust using seismic noise recorded at temporary seismological stations installed after the earthquake in the fault vicinity. These profiles, in the epicentral area, exhibit materials with increasing stiffness from the surface to 1.2 km depth overlaying less competent deposits. As remarked by Causse et al. (2020), this peculiar ground velocity profile with the presence at depth of softer material is consistent with the geological settings of the area (Elmi et al., 1996) and deep boreholes in the region.

Table 9: Crustal model.

Mass density (t/m <sup>3</sup> )	Vp (m/s)	Vs (m/s)	Thickness (m)
2	3400	2100	600
2.5	5800	3500	600
2.2	2000	1200	220
2.4	3900	2300	780
2.5	5800	3500	-

Concerning the basin infill sediments, we defined models for the P- and S- wave propagation velocity, based on the measured profiles available at the following sites (see Figure 42):

- the stations OGLP and CRU1, located along the Rhône River Valley;
- nuclear power plant sites TRICASTIN and CRUAS.

The adopted model for the shear wave velocity is shown in Figure 42 (black line, 'model'), together with the available profiles and the crustal model of Causse. The model was calibrated on the velocity profiles available at OGLP and TRICASTIN, mainly representative of the portion of the basin with the deepest depths (OGLP in particular). Profiles at CRU1 and CRUAS (NPP), located at the basin edge, were used for verification only.

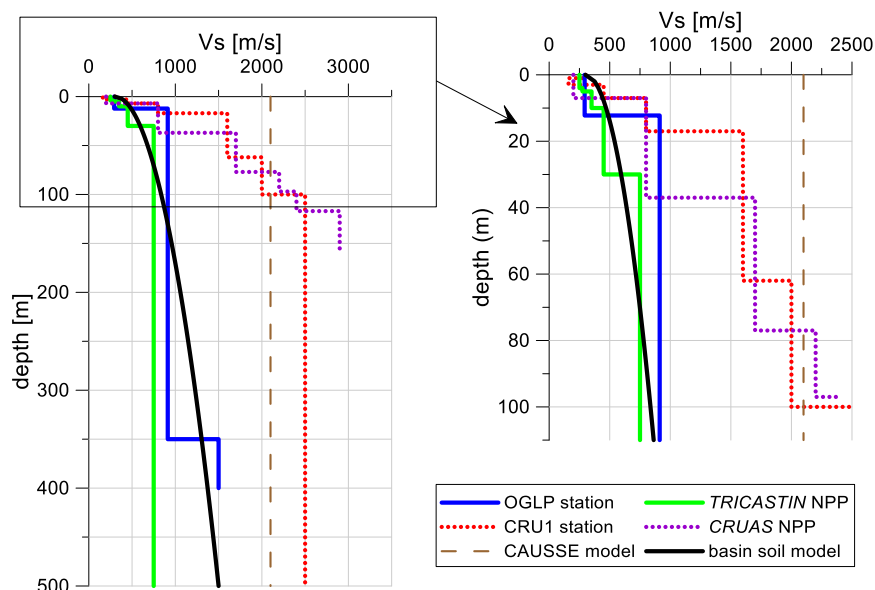


Figure 42: Shear wave velocity profiles available at different sites along the Rhône River Valley. The implemented model, calibrated on the basis of OGLP and Tricastin NPP profiles, is shown in black. The crustal velocity model of Causse et al. (2020) is denoted by dashed brown line. Profiles at the border of the basin, at CRU1 and CRUAS site, to the north of the epicenter, are shown in dotted lines.

The equation adopted for both P and S waves velocity profiles as a function of the depth from the topographic surface is the following:

$$Vel(z) = Vel_{ini} + (Vel_{fin} - Vel_{ini}) * \sqrt{\frac{z - z_{ini}}{z_{fin} - z_{ini}}} \quad 4.2.1$$

The parameters used to describe the model for Vs and Vp ( $Vel_{ini}$  and  $Vel_{fin}$ ) are shown in Table 10. For mass density, a constant value of  $1950 \text{ kg/m}^3$  has been chosen, in agreement with available data. Note that a common profile is used for any site inside the basin.

Table 10: Parameters of the P- and S-wave velocity profiles of equation (4.2.1).

Velocity Profile	$Z_{ini}$ (m)	$Z_{fin}$ (m)	$Vel_{ini}$ (m/s)	$Vel_{fin}$ (m/s)
P-waves	0	500	550	2300
S-waves	0	500	300	1500

Concerning anelastic attenuation properties, for all soil layers, a frequency-dependent quality factor ( $Q=Q_0*f/f_0$ ) has been adopted with  $Q_0 = VS/10$  and a reference frequency  $f_0 = 1 \text{ Hz}$ .

### 4.2.3 Features of 3D numerical mesh model and computational features

The numerical domain extends over a volume of  $45 \text{ km} \times 70 \text{ km} \times 8.5 \text{ km}$  and it is discretized using a structured conforming hexahedral mesh with characteristic element volume of about  $120 \text{ m} \times 120 \text{ m} \times 200 \text{ m}$  at ground surface, with a side of about  $550 \text{ m}$  at the bottom of the model. The mesh discretization was tested in order to verify the maximum frequency at which propagation was correctly simulated; this frequency resulted to be at about  $8 \text{ Hz}$  (see further section). For verification purposes against independent numerical codes dealing with 1D soil media, a simpler numerical mesh of  $45 \text{ km} \times 70 \text{ km} \times 3 \text{ km}$  was also built (SPEED-1D, see below). Therefore, two computational models have been built, as shown in Figure 43, with the following features:

- 'SPEED-1D model' (for verification tests): size =  $45 \text{ km} \times 70 \text{ km} \times 3 \text{ km}$ , with flat topography and crustal structure only (the basin is not included);
- 'SPEED-3D model' (full 3D model, used for final computations): size =  $45 \text{ km} \times 70 \text{ km} \times 8.5 \text{ km}$ , with the actual topography, crustal structure and the 3D basin structure.

The so called 1D model has been extensively used for the calibration of the numerical mesh, both with a layered and a homogenous crustal structure, checking the solution against an analytical, independent method (the Hisada code, as discussed in next Section) using point sources as well as extended faults.

Table 11 summarizes the main computational features of the two models, in terms of number of spectral elements, nodes, resolution frequency and time step.

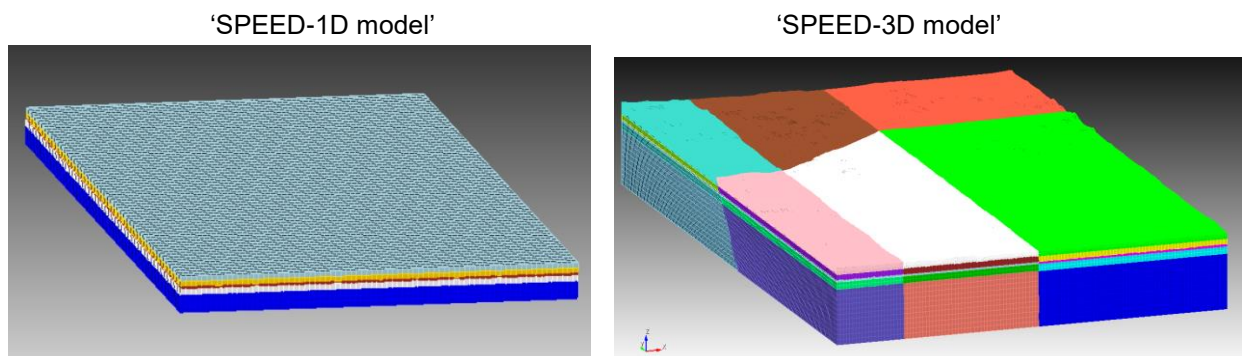


Figure 43: Numerical models built for simulations: 'SPEED-1D' model (left), 'SPEED-3D model' (right).

Table 11: Main computational features of the two numerical models adopted.

	elements	nodes	Spectral Degree (SD)	Max frequency (Hz)	Time step (s)	Time window (s)
SPEED-1D model	64'141	4274397	4	2.5	0.01	35
SPEED-3D model	1'254'000	34964554	4	2.5	0.01	35

Numerical simulations were performed exploiting the parallel computing capabilities of SPEED. For this project, they were carried out on the Marconi 100 Cluster at CINECA, the largest high-performance computing center in Italy ([www.cineca.it](http://www.cineca.it)), under the ISCRA C HP10CK5R9W project. The walltime for each numerical simulation (3D model) is around 3 hours on 128 cores of the Marconi 100 cluster.

Table 12 presents an overview of the different numerical simulations performed using both SPEED models to check the sensitivity of results.

Table 12: Summary of performed simulations.

Subsoil structure	Crustal model	Source model
SPEED-1D (flat-no basin)	Homogeneous	Point source
		Extended fault
	Layered	Point source
SPEED-3D (topo+basin)	Layered	Point source
	Layered	Extended fault

#### 4.2.4 Convergence tests in the high-frequency range

Among the various approaches for numerical integration of the linear-elastodynamic wave equations, the spectral element approach enjoys a high accuracy, that was estimated to ensure an accurate wave propagation with slightly more than the Nyquist limit of 2 points per minimum wavelength (ppmw) for homogeneous soil conditions, up to about 4 points per minimum wavelength in strongly heterogeneous materials (Faccioli et al., 1997). These estimates were based on verification tests on closed-form and/or reference solutions from literature. For a practical application, a proper check of the number of ppmw should be made on the specific case study, depending on the desired accuracy. For this purpose, a convergence test was performed considering the SPEED-3D numerical model described in previous section, with an extended fault source, where, with the same discretization in terms of spectral elements, the spectral degree (SD) of each element was increased from SD=1 (i.e., no internal node is present in the spectral element) up to SD=5. In this way, the accuracy of the solution for SD<sub>j</sub> can be checked by verifying at which frequency it departs significantly from the solution obtained with SD<sub>j+1</sub>. Results of this test are illustrated in Figure 44, showing that, taking as a reference SD<sub>5</sub>, the solution with SD<sub>4</sub> keeps close to SD<sub>5</sub> up to about 7.5 Hz on outcropping bedrock and up to about 5 Hz on outcropping basin. These should be considered as the reference accuracy limits of our numerical results when comparing them with records.

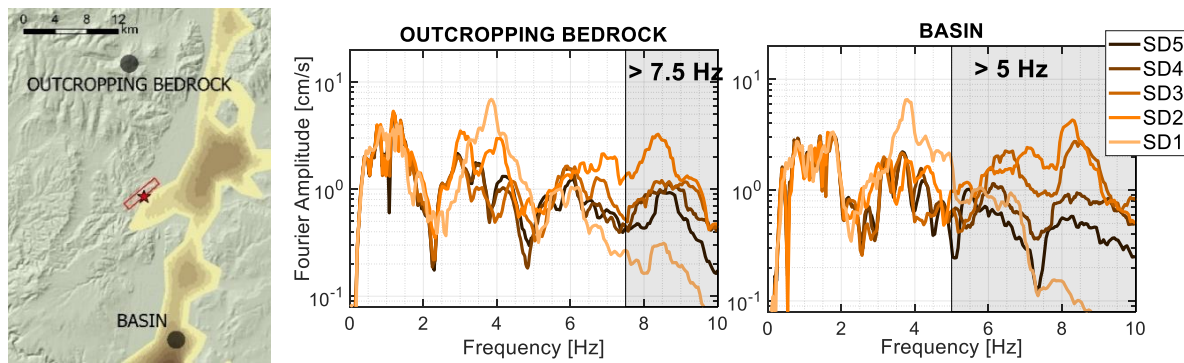


Figure 44: Fourier amplitude spectra simulated for varying Spectral Degrees (SD from 1 to 5) at two positions at about 17 km from epicenter: on outcropping bedrock (to the North) and on soil (to the South), inside the basin.

However it should also be pointed out that neither the input slip function nor the numerical model are detailed enough at high frequencies, that are dominated by small-scale effects of stochastic nature. As it will be shown by comparison of numerical results with records, the high-frequency decaying trend of simulated Fourier spectra is consistent with that of records, in spite of obvious relatively small differences. Because of such good agreement, we discarded the standard option to produce broadband results by hybrid approaches, the high-frequency part of which is determined by stochastic approaches (e.g., using as a target the spectral ordinates produced by an Artificial Neural Network, such as proposed by Paolucci et al., 2018). Indeed, such approaches are neither theoretically well constrained for very shallow events, as it is the case of Le Teil earthquake, nor a sufficient amount of records is available to reliably train an ANN. For this reason, we considered more physically sound to retain the numerical content of the signal up to about 8 Hz (i.e., signals were LP filtered below 10 Hz), because, even if affected by a moderate dispersion, the resulting wavefield retains the realistic characteristics in terms of amplitude, duration and spatial correlation, that would be lost by LP filtering and by using hybrid approaches.

#### 4.2.5 Verification analyses with Hisada code

As a preliminary step of the modeling process, simulations were performed using the Hisada code, based on the analytical integration of Green's functions (Hisada and Bielak 2003). This code allows for the computation of the ground motions in a horizontally layered half-space originated by a finite-fault kinematic source model.

Hisada's solution has been used in a preliminary phase to calibrate and validate the crustal model profile, the assumptions on the quality factor adopted, the slip model on the extended fault and the source time function.

Simulation of ground motions has been performed for the reference accelerometric stations within a 30 km distance from the epicenter (shown in Figure 41), respectively: CRU1 and ADHE (within 18 km from the source), TRI1 and OGLP (at about 24 km from the source), and the nearest one A192B (at about 8 km).

Figure 45 shows simulated velocity time histories and corresponding Fourier amplitude spectra, for station CRU1 and for a receiver very near the source (at about 1 km), using a simple point source model. For CRU1, recorded motion is shown as well. Results obtained with Speed '1D model' and Hisada are compared, using in both cases the layered crustal model, and a flat, 1D structure (with no basin). Agreement between simulations is quite good, especially in near source, showing excellent performance of numerical mesh. Agreement with recorded time series is good, both in amplitudes, frequency content and arrival times.

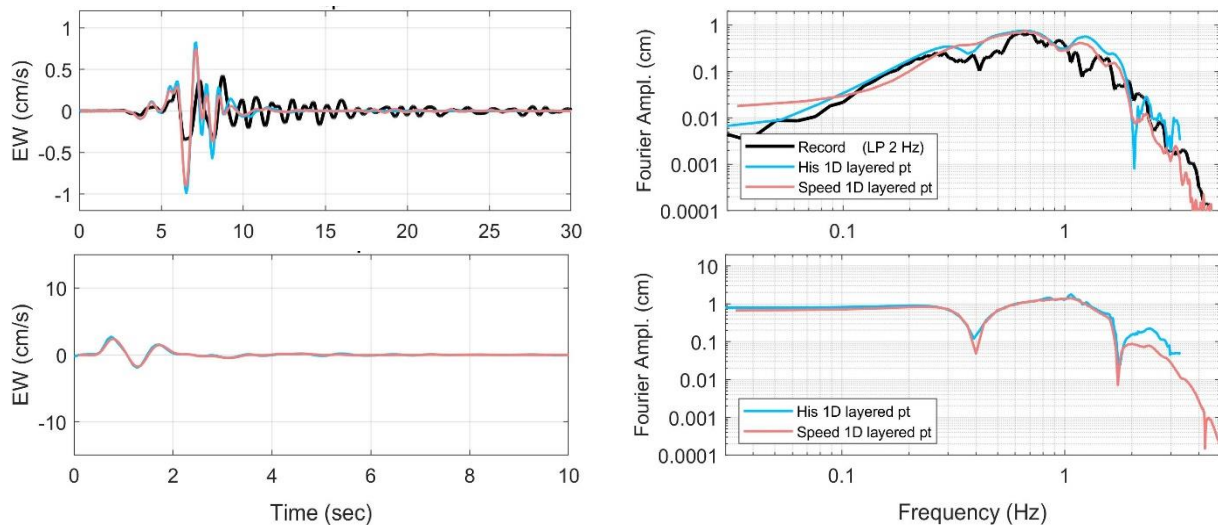


Figure 45: CRU1 station ( $R_{epi}=15$  km, top) and near field receiver ( $R_{epi}=1$  km, bottom). Simulated (and recorded, where available) velocity time histories and corresponding Fourier Amplitude spectra for EW component. Point source model. All time histories are low-pass filtered at 2 Hz. An exponential-type velocity slip function was used for this verification test, with a rise time of 1.2 s.

#### 4.2.6 1D and 3D point-source SPEED solutions

As remarked, two numerical models have been built, a 1D one (with flat topography and no basin inside) and a 3D one (with topography and basin interface). In this section we show the impact of the 3D model with reference to the case of the point source (and an exponential description of the source type velocity function).

Figure 46, Figure 47 and Figure 48 show comparisons between the 1D and 3D simulations, for the case of a point source. As noticeable, in the case of a station on a flat bedrock, such as ADHE (see Figure 41), the two simulations show limited differences, while in the case of a receiver inside the basin, such as OGLP, remarkable effects mainly due to the basin can be seen. The 3D simulation clearly improves in terms of amplitudes, durations and complexity, enhancing agreement with records.

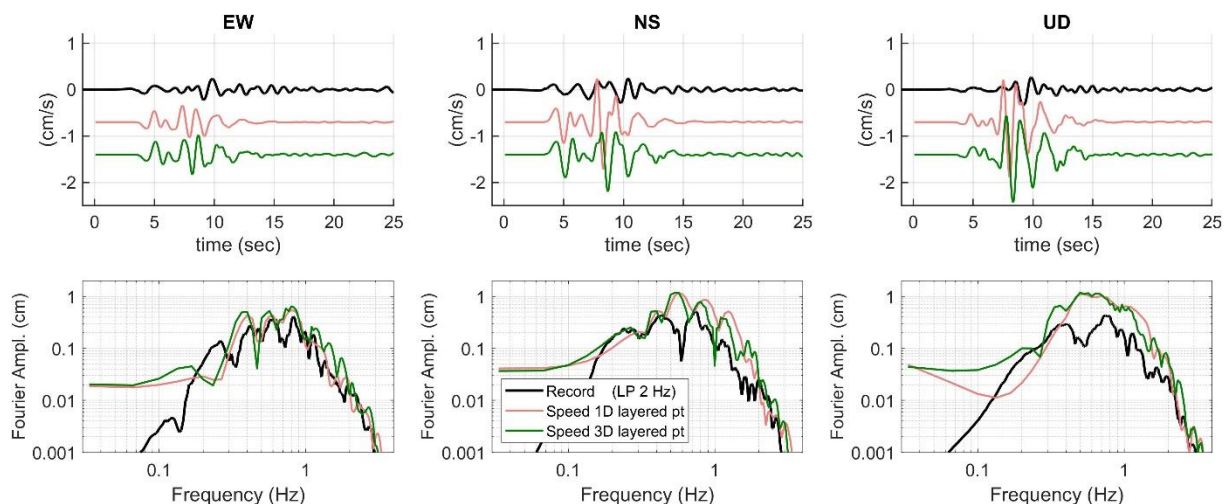


Figure 46: ADHE station ( $R_{epi}=18$  km). Simulated 1D and 3D and recorded velocity time histories, with corresponding Fourier Amplitude spectra. Point source model. All time histories are low-pass filtered at 2 Hz.

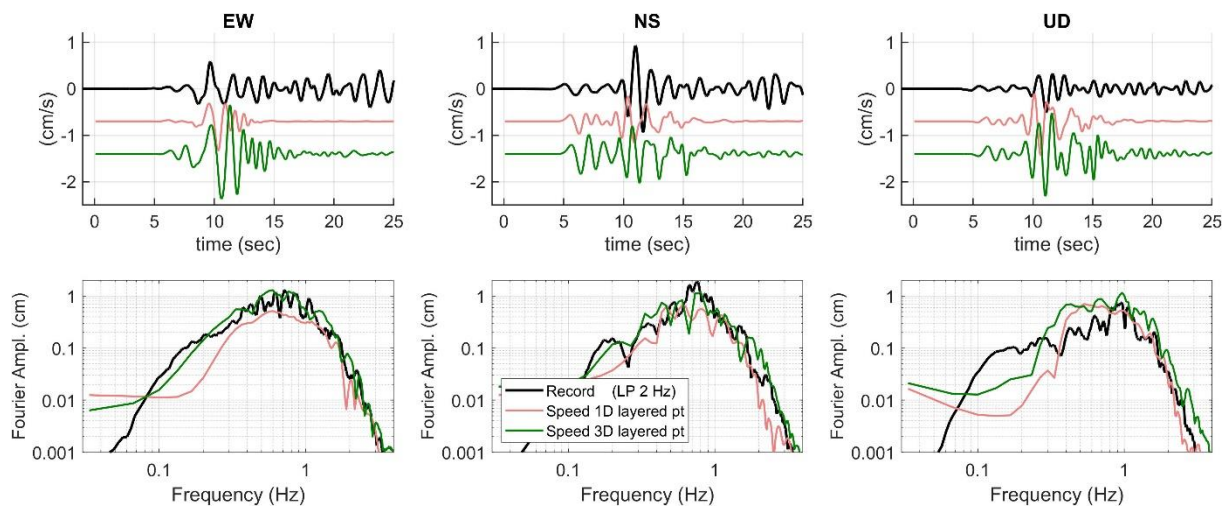


Figure 47: OGLP station ( $R_{ep}=24$  km). Simulated 1D and 3D and recorded velocity time histories, with corresponding Fourier Amplitude spectra. Point source model. All time histories are low-pass filtered at 2 Hz.

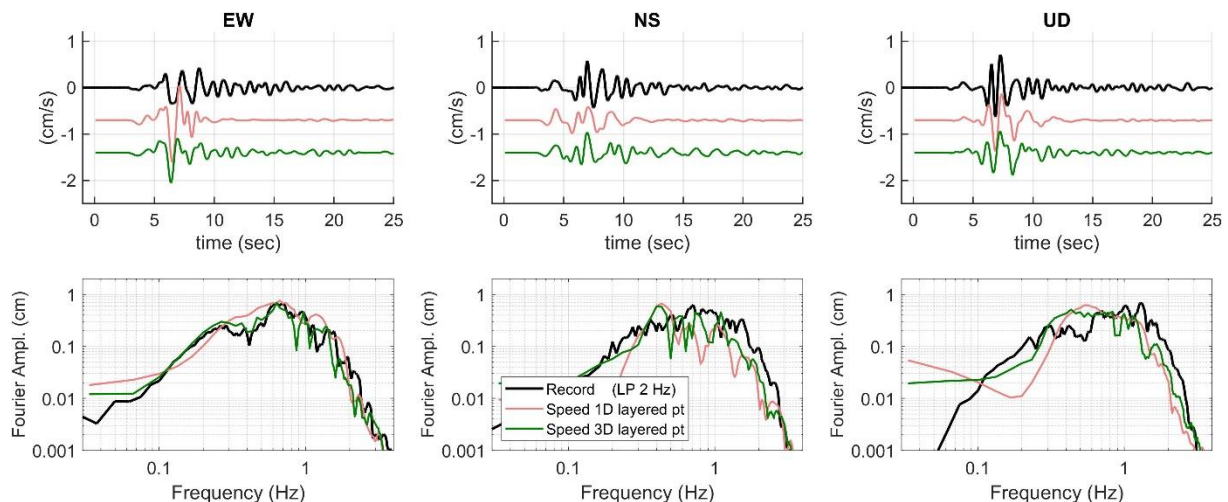


Figure 48: CRU1 station ( $R_{ep}=15$  km). Simulated 1D and 3D and recorded velocity time histories, with corresponding Fourier Amplitude spectra. Point source model. All time histories are low-pass filtered at 2 Hz.

#### 4.2.7 Finite-fault SPEED solutions with different slip distribution models

The influence of different kinematic slip distributions on simulated ground motion has been tested using two additional slip distribution models, modified respectively from Cornou et al. 2021, and from DeNovellis et al. 2020. These models are shown in Figure 49, together with the reference model of the benchmark (a). The two additional models were enhanced in the range of high frequencies, as described in Section 3.2 of this deliverable, and they are named respectively as Cornou HF (b), and DeNovellis HF (c).

Note that the modified model after De Novellis et al. was obtained using the single fault plane slip distribution generated by the authors from inversion of observed DInSAR displacement data. The resulting fault plane is slightly wider than the Cornou et al fault, being  $L=5025$  m and  $W=1925$  m. The hypocenter position is similar, while strike, dip and rake angles are respectively:  $50^\circ$ ,  $62.3^\circ$  and  $116.5^\circ$ .

The slip time function adopted in these simulations (and in final results as well) is the one proposed by Crempien and Archuleta (2014), with a rise time of 0.5 s (see details in the bottom of Figure 49).

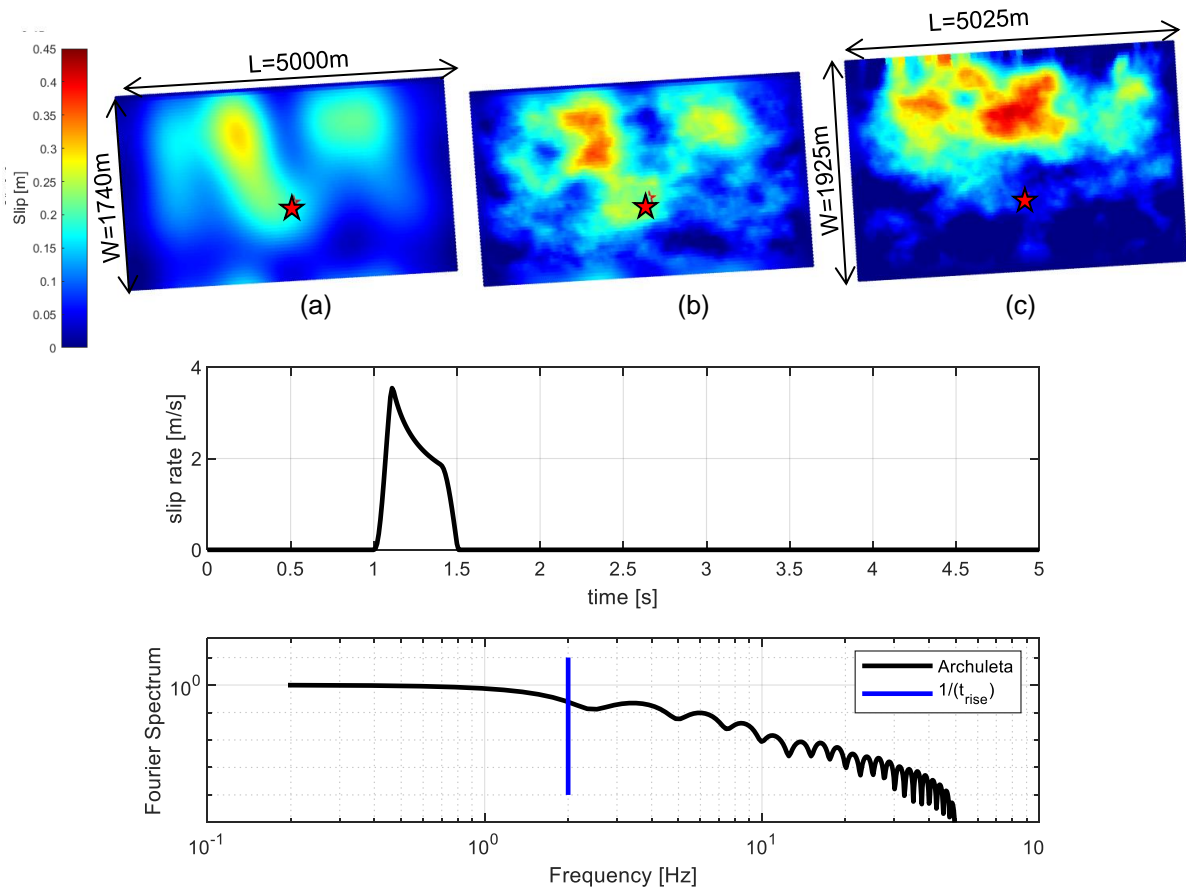


Figure 49: Top: Slip distribution models used in the sensitivity tests. Slip is shown in meters. (a) Slip model from Cornou et al. (2021) and Causse et al. (2020). (b) Same as (a), improved in the High Frequency content (see Figure 3 of this deliverable); (c) Modified slip model from De Novellis et al. (2020), improved as well in the High Frequency range. Bottom: adopted slip function, in time and frequency domain, with a rise time of 0.5 s.

Figure 50 compares the simulations obtained with the slip models of Figure 49, in the time and frequency domain, for stations OGLP and CRU1 (at respectively 24 and 15 km from the epicenter) and for a position very near the source (at about 1 km from the epicenter, shown Figure 41). EW horizontal components (LP filtered at 10 Hz) are shown in the figure, together with recordings, when available. It turns out that improving source irradiation at high frequency in Cornou et al. model does not significantly alter results: almost identical ground motion is simulated both at short and long distance from the source, most likely because variations occur at frequencies larger than the ones solved by the PBS. The use of the De Novellis slip distribution, on the other hand, affects both lower and higher frequency content near the source, while it becomes irrelevant far from the fault, as expected.

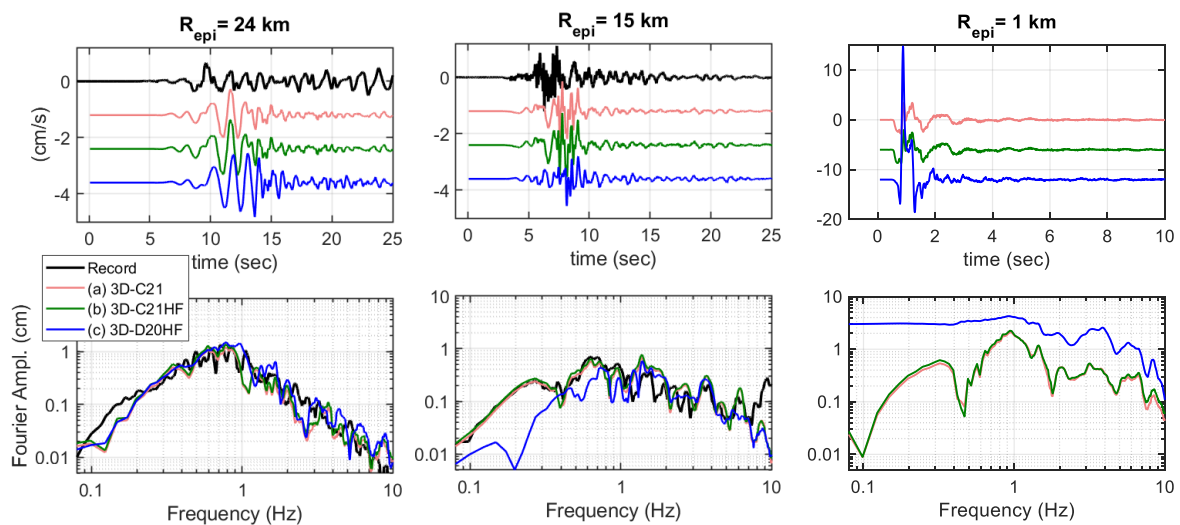


Figure 50: OGLP ( $R_{epi}=24$  km), CRU1 ( $R_{epi}=15$  km) and a near site station ( $R_{epi}=1$  km). Simulated and recorded (where available) EW velocity time histories, with corresponding Fourier amplitude spectra, for the different slip models of Figure 49: a) and b) for Cornou et al. and c) for De Novellis et al. models. All time histories have been low-passed filtered at 10 Hz.

#### 4.2.8 Overview of results

In this section a summary of the final simulations of the benchmark is given. The final simulations refer to the 'full' 3D SPEED model, i.e., the model including soil topography as well as the basin and the extended fault model (shown in Figure 51). The kinematic source parameters of the finite-fault model are the reference ones of the benchmark (see Section 2.2). The slip time function is the one shown in Figure 49, with a rise time of 0.5 s. Results for all five reference stations are shown in the Annexes, in both time and spectral domains.

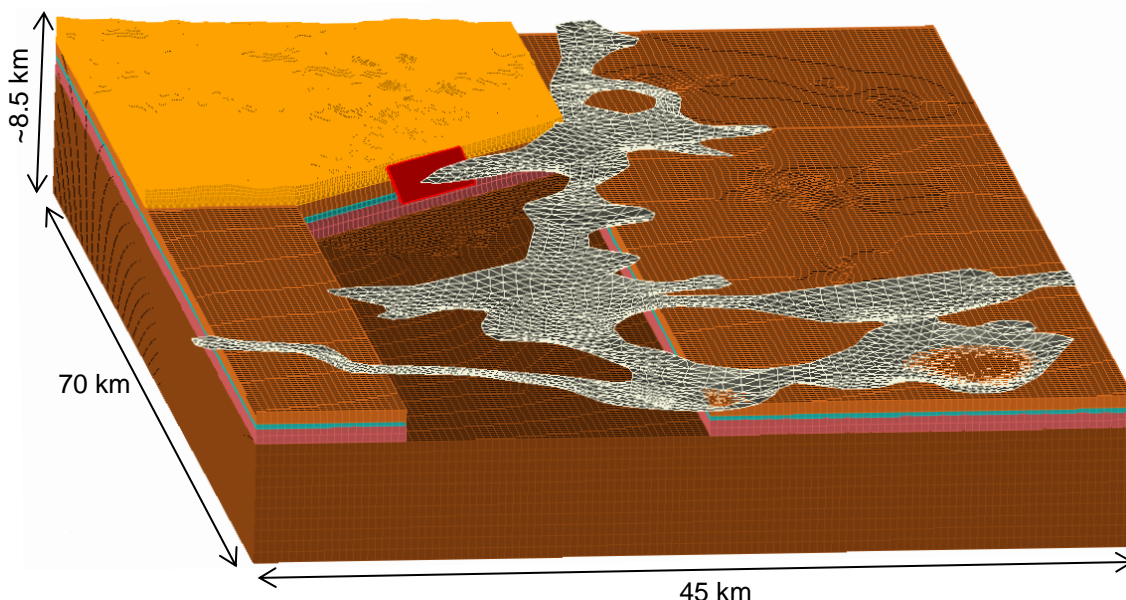


Figure 51: Overview of the final 3D numerical model: view of basin structure, crustal layering and numerical fault (in red).

Figure 52 shows ground shaking maps of peak ground displacement (PGD), velocity (PGV) and acceleration (PGA) for both horizontal and vertical components of motion. Observations are shown as well, at reference stations, using the same palette. The influence of the basin sediments on ground motion is clearly noticeable, in all maps, although limited in amplitude. In general, the maps indicate a realistic spatial correlation structure of peak ground motion values, in a wide frequency range (from

PGD, at low frequency, to PGA, at larger frequencies): as expected, PGA shows a more significant contribution of small-scale spatial variability than PGV and PGD. Agreement with peak values of recorded motion is considerable, mostly in the horizontal directions.

Although not shown herein for sake of brevity, the simulated permanent vertical displacement on the surface projection of the fault plane (see, as a proxy for the spatial distribution of permanent ground uplift, the PGD -UD map in Figure 52, bottom-right) reaches maximum values of about 10 cm, consistently with the maximum uplift from InSAR measurements (Ritz et al. 2020).

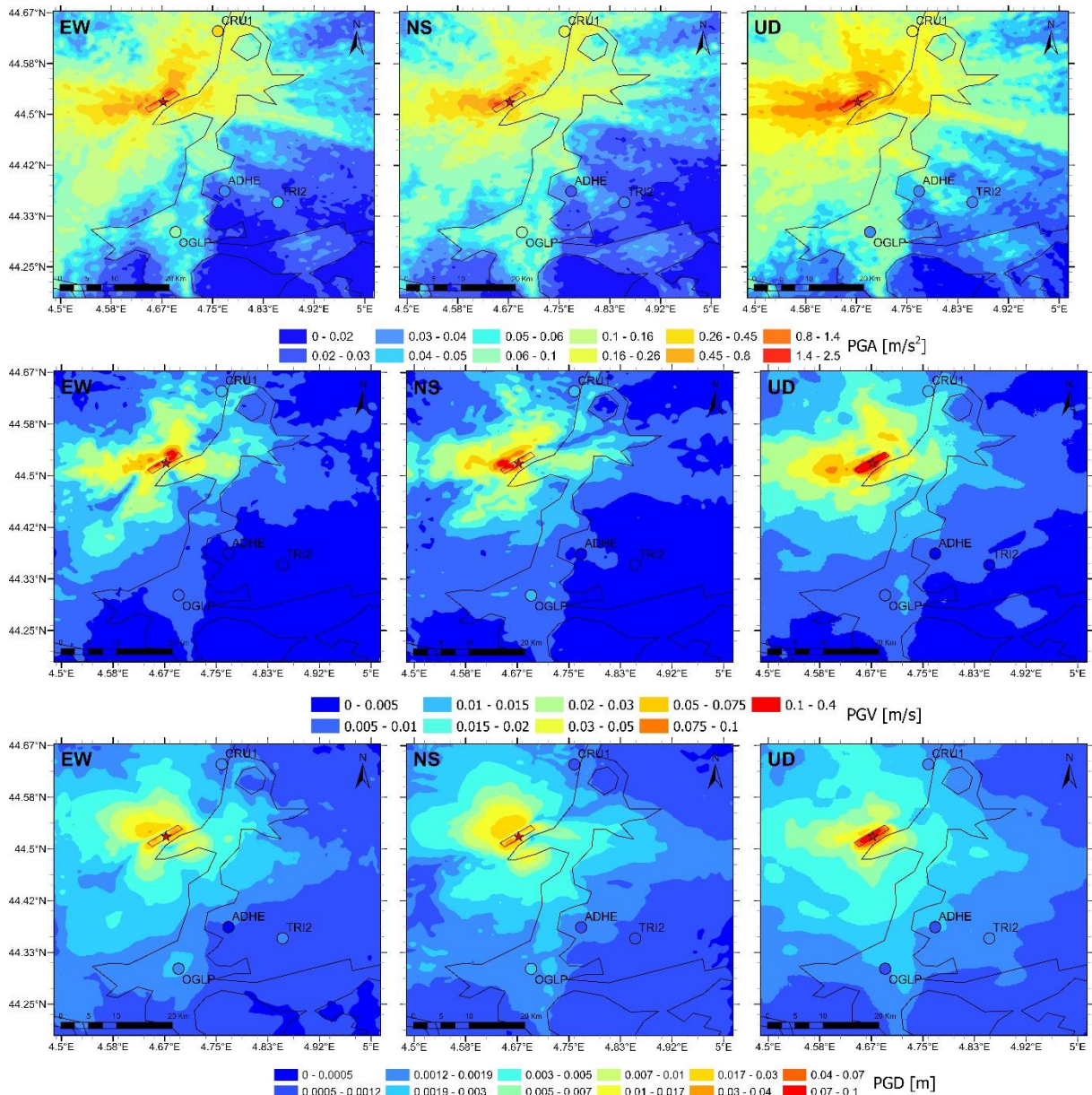


Figure 52: PGA (top), PGV (middle) and PGD (bottom) maps from numerical simulation. Observations are shown with colored circles, in same palette. Le Teil earthquake fault (red rectangle) and epicenter (red star) are shown as well. (all data in maps are low-pass filtered at 10 Hz).

## 5 Simulation's methods and Ground motion variability

### 5.1 Comparison for different ground motion intensity measures

In this section, the results of the four simulation techniques introduced in the sections 3 and 4 of this study are compared.

Figure 53 compares the Fourier Amplitude Spectra of unfiltered acceleration time histories computed through the different simulations at the five benchmark stations (ADHE, CRU1, OGLP, TRI2 and A192B). Recordings at station A192B have been omitted from these plots since they are not reliable owing to saturation issues. Knowing that a perfect match between simulations and recordings is an out of reach objective, in general, the FAS simulated using the different techniques approach the observed ground motion features with different accuracy levels, depending on the frequency band and the considered technique. Empirical Green's function techniques are particularly good at reproducing specific features of site response (i.e. the 8-9 Hz amplification peak observed on ground motion recorded at CRU1 station), because site-response features are included in the recordings used as EGF. Physics-based simulations, allow to well reproduce lower frequency patterns of observed ground motion (below 1 Hz), where EGF-based simulations perform worse due to the poor signal-over-noise ratios of the aftershocks. It is worth to notice, for future investigation, that the FAS calculated using the two empirical Green's function simulation techniques (Irikura and Dujardin modified) show significant differences, especially at low frequencies, despite the fact that they use similar input parameters and share the same simulation concept. For ADHE station, the 1D physics-based simulation seems to overestimate the Fourier amplitude for frequencies larger than 1Hz. Except for the Z component, the physics-based simulations show good agreement with the FAS at OGLP station.

Figure 54 represents the comparison for the time domain ground motion intensity measures of both instantaneous and integral type (PGA, PGV, Arias Intensity and Duration), calculated for the simulated and recorded data after applying a band-pass filter between 1 and 10 Hz (frequency range where all the simulation techniques are considered reliable). For the comparison on a broad frequency range, the results obtained for the frequency range 0-10 Hz are shown in Appendix 4. As for the FAS, the variability of these intensity measures across the simulation approaches is high and it is sensitive to the station and epicenter-to-station direction. As for the frequency domain, the results depend on the analyzed direction and station. In addition, these results depend also on the analyzed ground motion intensity measure. The Arias Intensity and PGA seem to have similar behavior: the relative performance of the simulated values versus observed data for PGA and AI are not drastically different. In fact, Arias Intensity (AI) is generally highly correlated with high-frequency characteristics of motion like PGA (see, e.g., Campbell and Bozorgnia, 2012, 2019). Thus, the behavior of PGA and AI should be conceptually close to each other.

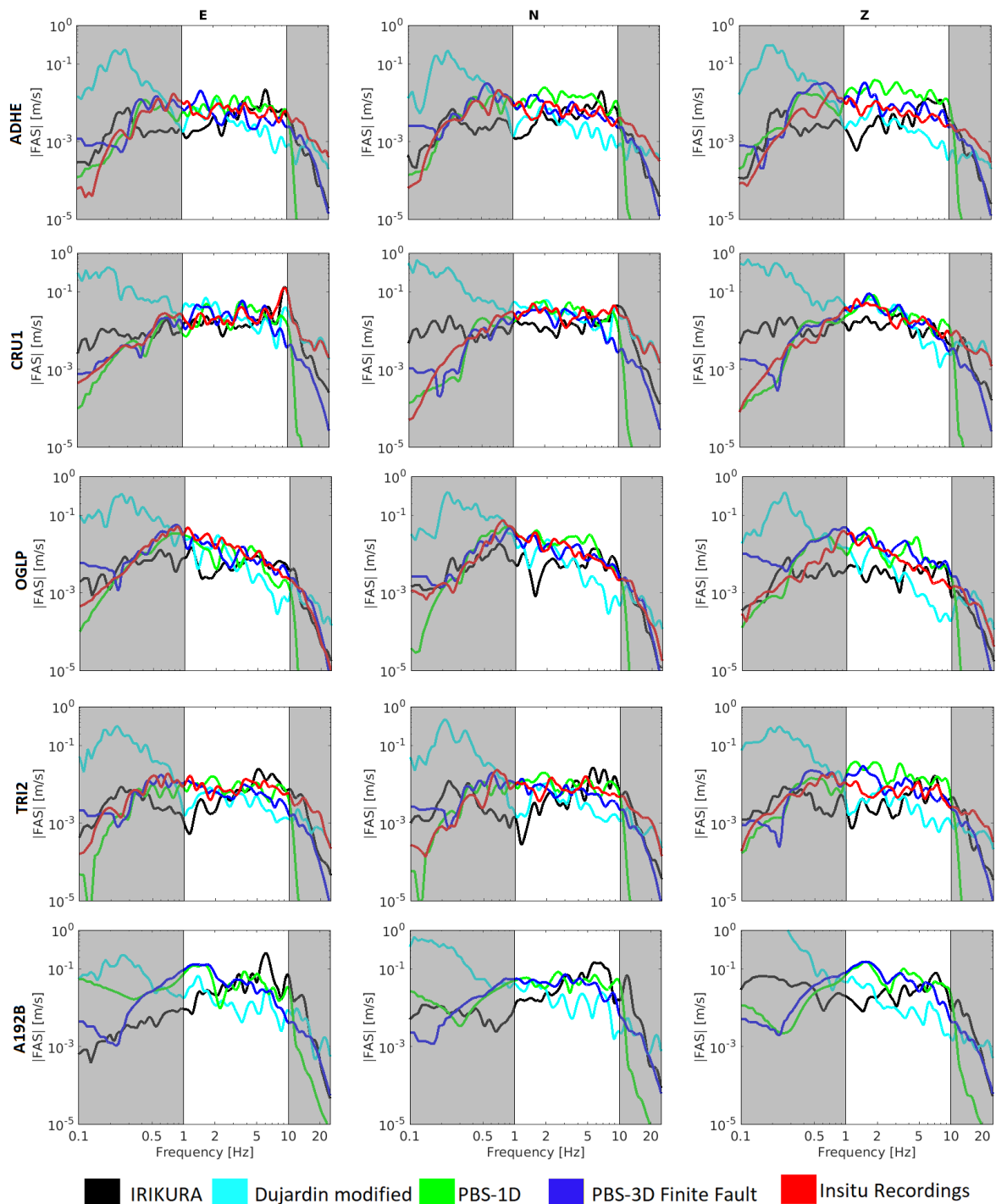


Figure 53: The Fourier Amplitude Spectrum (FAS) of three-component (E: East-West; N: North-South; Z: Up-Down) unfiltered acceleration time histories calculated by the five different simulations (Irikura in black, Dujardin modified in cyan, PBS-1D in green and PBS-3D with finite fault in blue) and smoothed with the Konno and Ohmachi ( $b=40$ ; Konno and Ohmachi, 1998), at five stations (from top to bottom, ADHE, CRU1, OGLP, TRI2 and A192B). The red color corresponds to the recordings.

Compared to other stations, results at CRU1 station show relatively small variability across the simulation techniques. This station is the only one located to the north side of the rupture and may be less sensitive to the shadow effect of the basin.

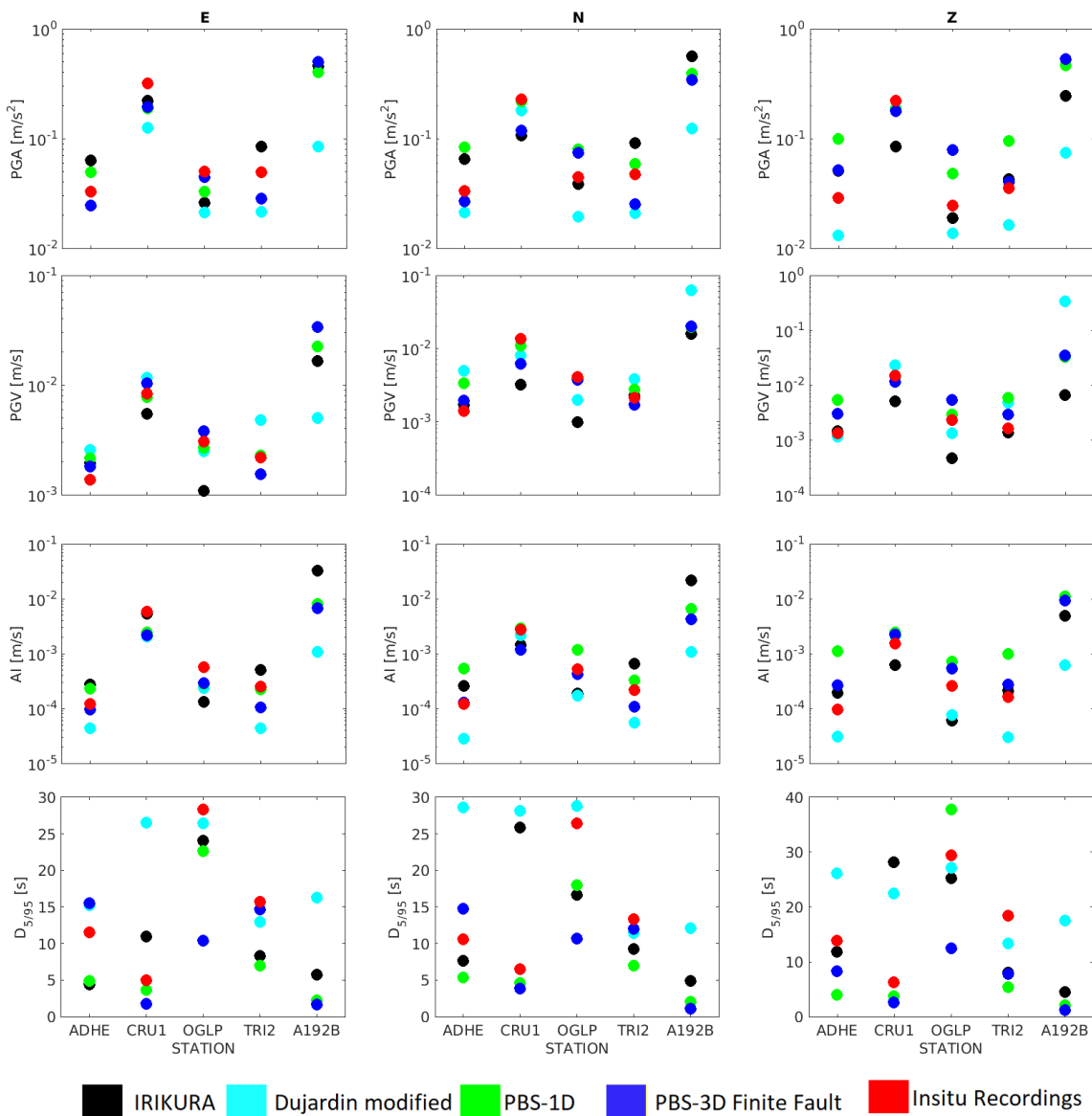


Figure 54: The ground motion intensity measures (PGA, PGV, Arias Intensity and Duration) calculated within a frequency range between 1 and 10 Hz, by using the five different simulations (Irikura in black, Dujardin modified in cyan, PBS-1D in green, PBS-3D with a point source in magenta and PBS-3D with finite fault in yellow) for the three components (E: East-West; N: North-South; Z: Up-Down), at five stations (ADHE, CRU1, OGLP, TRI2 and A192B). The red color corresponds to the recordings.

Table 13 represents the Goodness of Fit ( $GoF$ ) between simulated and recorded data, filtered between 1 and 10 Hz and calculated for the five ground motion intensity measures, for the three components of the four stations (ADHE, CRU1, OGLP and TRI2). For the FAS, the calculated  $GoF$  corresponds to the average of the values estimated between 1 and 10 Hz.

Table 13: The Goodness of Fit (GoF) between simulated and recorded accelerograms filtered between 1 and 10 Hz and calculated for the five ground motion intensity measures (PGA, PGV, Arias Intensity, Duration and FAS) estimated by using the five simulation results. The results are sorted by station and by calculation direction.

Goodness of Fit							
GM Indicator	Station	Direction	Simulation's technique				
			Irikura	Dujardin Modified	PBS - 1D	PBS - 3D Finite Fault	
PGA	ADHE	E	0.2880	-0.1262	0.1804	-0.1264	
		N	0.2909	-0.1978	0.3988	-0.0976	
		Z	0.2473	-0.3457	0.5349	0.2525	
	CRU1	E	-0.1565	-0.4079	-0.2260	-0.2180	
		N	-0.3303	-0.1015	-0.0155	-0.2853	
		Z	-0.4175	-0.0682	-0.0713	-0.0940	
	OGLP	E	-0.2852	-0.3713	-0.1876	-0.0517	
		N	-0.0617	-0.3569	0.2520	0.2215	
		Z	-0.1180	-0.2584	0.2902	0.5043	
	TRI2	E	0.2350	-0.3623	-0.0036	-0.2421	
		N	0.2857	-0.3537	0.0909	-0.2742	
		Z	0.0794	-0.3375	0.4313	0.0566	
PGV	ADHE	E	0.1558	0.2754	0.1982	0.1205	
		N	0.0857	0.5507	0.3776	0.1423	
		Z	0.0368	-0.0586	0.6050	0.3524	
	CRU1	E	-0.1844	0.1469	-0.0266	0.0953	
		N	-0.6292	-0.2287	-0.0943	-0.3366	
		Z	-0.4603	0.1950	-0.0250	-0.1103	
	OGLP	E	-0.4512	-0.0923	-0.0611	0.0927	
		N	-0.6147	-0.3140	-0.0159	-0.0393	
		Z	-0.6995	-0.2383	0.0975	0.3743	
	TRI2	E	0.0101	0.3418	0.0156	-0.1537	
		N	0.0296	0.2572	0.1138	-0.0947	
		Z	-0.0808	0.4703	0.5630	0.2528	
AI	ADHE	E	0.3520	-0.4400	0.2850	-0.0961	
		N	0.3278	-0.6374	0.6366	0.0268	
		Z	0.3099	-0.4898	1.0655	0.4509	
	CRU1	E	-0.0380	-0.4547	-0.3829	-0.4249	
		N	-0.2778	-0.0989	0.0364	-0.3637	
		Z	-0.3897	0.1378	0.2050	0.1628	
	OGLP	E	-0.6236	-0.3764	-0.3028	-0.2915	
		N	-0.4430	-0.4770	0.3512	-0.0912	
		Z	-0.6222	-0.5254	0.4425	0.3210	
	TRI2	E	0.3040	-0.7512	-0.0503	-0.3777	
		N	0.4843	-0.6000	0.1764	-0.3114	
		Z	0.1182	-0.7312	0.7818	0.2326	
D95	ADHE	E	-0.4114	0.1211	-0.3705	0.1297	
		N	-0.1419	0.4336	-0.2901	0.1462	
		Z	-0.0671	0.2773	-0.5377	-0.2194	
	CRU1	E	0.3407	0.7229	-0.1372	-0.4645	
		N	0.5961	0.6328	-0.1573	-0.2329	
		Z	0.6508	0.5519	-0.2230	-0.3756	
	OGLP	E	-0.0721	-0.0300	-0.0974	-0.4371	
		N	-0.2003	0.0376	-0.1680	-0.3932	
		Z	-0.0659	-0.0353	0.1080	-0.3753	
	TRI2	E	-0.2777	-0.0840	-0.3553	-0.0308	
		N	-0.1593	-0.0674	-0.2835	-0.0456	
		Z	-0.3588	-0.1372	-0.5338	-0.3702	
FAS	ADHE	E	0.0225	-0.4575	0.1216	-0.1556	
		N	0.0712	-0.4440	0.3273	-0.0076	
		Z	0.0693	-0.4718	0.5573	0.1532	
	CRU1	E	-0.1363	-0.2501	-0.1244	-0.2435	
		N	-0.2141	-0.1747	-0.0209	-0.3200	
		Z	-0.1648	-0.2865	0.1048	-0.0395	
	OGLP	E	-0.1138	-0.5333	-0.1832	-0.0488	
		N	-0.0996	-0.5517	0.1777	0.0331	
		Z	-0.0693	-0.6228	0.3114	0.3269	
	TRI2	E	0.0050	-0.4955	-0.0256	-0.2217	
		N	0.0464	-0.4827	0.1106	-0.1608	
		Z	-0.0934	-0.5273	0.3955	0.0385	

As commented previously, the estimated  $GoF$  are sensitive to the GM intensity measure, the station and the azimuth. For selected stations, a non-negligible variability is found also between approaches belonging to the same class of methods (i.e. the two EGFs and the two PBSs), because of the assumptions and constraints at the basis of the approaches. For horizontal PGA, a lower variability of  $GoF$  scores across the different techniques is found; on the other hand, as expected, integral measures show larger uncertainties. The Fourier amplitude spectrum can be predicted with reasonable accuracy by the EGF techniques (especially Irikura), at least in this specific frequency range (1-10 Hz). However, these techniques are sensitive to the signal-to-noise ratio of aftershocks recordings, which may limit strongly its accuracy in the low frequency range, and, at high frequencies, to the source input parameters and thus the PGA variability may be larger than other simulation's techniques. However, it should be stressed that this comparison is limited to a rather limited frequency band, so that a partial picture of ground response is provided.

The results shown in this section for the Dujardin modified technique correspond to the slip distribution A (estimated by Cornou et al. (2020)). The results obtained by using the slip distribution B (distribution that fits better a Brune (1970) model) are presented in Appendix 5 for a frequency range between 1 and 10 Hz. The difference between the two slip distributions is shown in section 3.2.2. Since the Dujardin et al. (2020) technique has been developed for a  $k^{-2}$  source mode, it is more relevant, for the Le Teil earthquake benchmark, to apply this technique using the slip distribution in B. With this new slip distribution, the results show a much better  $GoF$  than the one with the benchmark slip distribution. Knowing that the new slip distribution may not affect the results at low frequencies, it should be used for future comparison between the different techniques to evaluate its impact on the results especially at high frequencies.

Finally, the results obtained for the Le Teil earthquake cannot be generalized. In fact, the empirical Green's function simulation techniques in this case benefit from the fact that the aftershocks occurred at the same place of the target event and have the same rupture mechanism than the main event, which leads to a smaller uncertainty in the input parameters.

## 5.2 Advantages and disadvantages

Table 14 summarizes the advantages and disadvantages of the different techniques used in this study. Between the time consuming problem of the 3D simulations and the limitation in frequency for the empirical simulations, this table shows the importance of combining different techniques in the ground motion broadband prediction studies.

Table 14: Comparison table between the different simulation's techniques.

Simulation method	EGF techniques		Physics-based simulations	
	Irikura recipe	Dujardin modified method	1D simulations	3D simulations
Frequency range	Depends on SNR for low-frequency : generally from 1 Hz to 25 Hz	Depends on the SNR but usually above 1 Hz.	0-10Hz	0-8 Hz
Approximate calculation time (per simulation)	Intel(R) Core(TM) i7-6820HQ CPU @ 2.70GHz – 5 stations with 2 EGF (10 simulations) = 30 min	For five stations: 10 mins on a i7 processor with a 2.4 Hz CPU.	- 10 min to prepare unscaled seismograms - 15 seconds to scale them with source effects (one realization)	~3 hours on 128 cores of the Marconi100 cluster at CINECA computing center <sup>1</sup>
Advantages	Easy to apply No need for 3D soil model Applicable for high frequencies	Easy to apply No need for 3D soil model Applicable for high frequencies	- Velocity - Easy to perform sensitivity analysis Cover a range of frequencies useful for engineering analysis	-3D features of topography, extended fault rupture and geology are simultaneously accounted for -insight into the wave propagation physics -spatial correlation of earthquake ground motion -suitable to explore virtually the parameter space -suitable to provide waveforms and ground shaking scenarios in future earthquakes for site-specific applications
Disadvantages	Depends on the number of available EGFs EGFs must be well defined Sensitive to the recordings	Depends on the number of available EGFs EGFs must be well defined Sensitive to the recordings	- Needs accurate definition of stratigraphy (deep structure, local structure and attenuation factor); Cannot capture effects related with 3D heterogeneities	-frequency resolution conditioned on the mesh discretization (hardly larger than 10 Hz) -High computational cost (supercomputers needed) -Need of expert users -Hard to construct well-constrained 3D subsoil model -Large epistemic uncertainties

<sup>1</sup> Hardware details on Marconi100 cluster can be found here: <https://www.hpc.cineca.it/hardware/marconi100>

## 6 Conclusions and perspectives

This report summarizes the results of a benchmark carried out using different ground motion simulation techniques in a low-to-moderate seismicity area. The test case is represented by the November 11, 2019 Mw4.9 Le Teil earthquake, occurred near the city of Montélimar, SouthEastern France, on La Rouvière fault that was not considered a potentially active fault in the BDFA (Jomard et al., 2017).

The simulations techniques used in this study belong to the class of Empirical Green Function and to the class of Physics-Based Simulations (PBS) using both 1D or 3D soil models, namely: (1) the Irikura recipe (see Section 3.1), (2) the Dujardin modified technique (Section 3.2), (3) the 1D physics-based-simulation (1D-PBS, Section 4.1), and (4) the 3D physics-based simulation (3D-PBS, Section 4.2). Ground motions are simulated at five stations (ADHE, CRU1, OGLP, TRI2 and A192B) and different ground motion intensity measures are analyzed to assess the general performance of these approaches.

Starting from the literature review on the Le Teil earthquake (Delouis et al., 2019; Causse et al., 2021; Cornou et al., 2020; Ritz et al., 2020; De Novellis et al., 2020; Mordret et al., 2020), a set of common input parameters and assumptions are defined to ensure a consistent comparison of the benchmark results.

The main conclusions of the benchmark can be summarized as follows.

### (1) Empirical Green Function approaches

The results obtained using the two EGF techniques (the Irikura recipe and the Dujardin modified technique), show a good consistency with the recorded data in the frequency range between 1 and 10 Hz. This is somewhat expected: as a matter of fact, the main advantage of the EGF approaches is that they do not require a precise description of the propagation medium, nor of the shallow soil properties at the target site, since this information is carried by the EGF itself. On the other hand, their applicability is conditioned on the availability of high-quality records of small earthquakes at the target site originated by the same seismic source. The main drawback for these techniques is therefore represented by the signal-over-noise ratio (SNR) that characterize the record of the small event used as EGF. As it has been shown in this case study, the SNR was very poor at frequencies lower than 1 Hz. Simulations are therefore not reliable below this frequency. The results also highlighted that earthquakes of significantly smaller magnitude than the target earthquake can be successfully used as EGF. This represent an interesting evolution of the classical use of EGF techniques, claiming that difference in magnitude between the target event and the EGF should not exceed 2 magnitude units in order to produce reliable results.

Another potential drawback of the EGF-based simulations used in low-to-moderate seismicity regions is that, being based on weak ground motion records, the simulated ground motion is representative of linear elastic domain behaviour, while non-linear soil behavior cannot be directly predicted using these techniques.

The records of the two largest aftershocks of Le Teil earthquake are used independently as Empirical Green's Functions (EGFs) and they are found to give similar results. This seems to suggest that the target event does not necessarily have the same focal mechanism as the small earthquake used as EGF, while the location of the small event should still coincide with the location of the target event.

Because of its ease of utilization, EGF approaches may be efficiently used for parametric analyses regarding the source model. For Le Teil case study, sensitivity studies are performed for both approaches, the Irikura recipe and the Dujardin et al (2020) modified approach. In the first case, stress drop, rupture speed and rise time of the target event were varied. The results show a large variability of the estimated Fourier Amplitude Spectra of surface ground motion. In the second case, the sensitivity study is performed by varying, first, the input source parameters of the target event (stress drop, rupture speed, nucleation position on the rupture zone) and second, the EGFs' properties used to simulate ground motion (EGF's magnitude, stress drop, strike and dip). The results clearly highlight the importance of the target event stress drop and the EGF's magnitude in the variability of the outputs.

Simulation Techniques benchmark, the test case of the November 11, 2019 Mw4.9 Le Teil earthquake

Besides, this study shows that some ground motion parameters, like the Arias Intensity, are more sensitive to the variability of the input parameters than others. Moreover, by using the sensitivity study of the source parameters and varying all the inputs together, a new slip distribution, stress drop, rupture speed and nucleation position are proposed to better fit the recordings of the Le Teil earthquake.

### (2) 1D Physics-Based Simulation

For the specific test-case considered in the benchmark, the use of 1D-PBS techniques shows a quite good consistency between the simulated and recorded ground motions, especially for CRU1 station where the results are good for the three components. The difference observed for the other stations located at the south of the rupture, is likely to be related to the complex 3D geometry of the Rhone paleo-valley that constitute the wave propagation medium. The sensitivity study performed generating five hundred simulations with rupture processes defined by different slip distribution, mean rupture velocity, nucleation point, rupture front evolution, shows significantly large variability of the results, which highlights that source parameters play a key role in ground motion prediction, also for a moderate magnitude earthquake. For this reason, these techniques may be very useful to explore the source model parameters and provide best-estimate solutions, before performing more complex simulations that account for the 3D structure of the medium. We also stress that, within simpler geological contexts, these techniques, less demanding than 3D simulation techniques in terms of computational resources, can provide satisfactory results.

### (3) 3D Physics-Based Simulation

Compared to the previous techniques, the 3D physics-based simulation approach (SPEED code) allows to account for the 3D seismic velocity model of the Rhone River valley, which is a key geological feature in the target area. However, this case study has clearly pointed out the difficulty in constructing and calibrating such large-scale 3D velocity models because of the lack of detailed geological and geophysical data with a sufficient spatial coverage and resolution. As a matter of fact, this work has led to the construction of a preliminary model of the Rhone River valley, using the very limited information available.

Numerical convergence tests, performed on PBS results with varying spectral degree, indicated that the maximum frequency propagated by the model reaches around 8 Hz. At variance with EGF, physics-based numerical modelling is known to be very accurate in the low-frequency range, as confirmed by the consistency between the simulated vertical permanent displacement and the InSAR measurements. This points out one of the main advantages of the approach, i.e. that it can provide accurate predictions of ground motion at very low frequency, including static offsets on the fault, that are hardly retrieved from records.

3D PBS were carried out using both a point source and a finite-fault kinematic source model. The point source simulations were used for verification purposes only. Results obtained with the finite source model have shown a very good agreement with records up to about 8 Hz, both in the time and frequency domain. The Goodness of Fit calculated to compare simulated and recorded accelerograms does not exceed 0.5 for all the stations, components and analysed ground motion intensity measures. The 3D PBS technique shows a very good accuracy particularly at stations OGLP and CRU1. At stations TRI2 and ADHE, results show a lower agreement with observations, probably due to the shadow effect of the basin. In conclusion, this benchmark has highlighted the key role of a well-constrained and accurate modeling of the source in a sufficiently broad frequency range, also for a moderate magnitude earthquake at some 20-25 km distance.

As a further remark, it is recalled that one of the most relevant advantages of large-scale physics-based numerical simulation lies in its capability to predict ground motion waveforms at any point of the model over a vast area and, hence, to be used for generating ground shaking maps preserving the spatial correlation structure. For this reason, in spite of the huge computational burden, the approach appears promising to provide spatially-correlated ground shaking scenarios in future earthquakes for site-specific applications.

In conclusion, it is stressed that the different simulation techniques considered in the benchmark are complementary to each other and each provide a good performance in different frequency ranges, accordingly with the limitations of the technique used: while EGF-based simulations are reliable in the higher frequency range (above 1 Hz), the PBS simulations are suitable especially in the low frequency range (typically below about 2 Hz). However, when the dimensions of the numerical domain are relatively small as in this case, the results obtained by this study proved that a good agreement with records is achieved by PBS up to about 8 Hz, provided the rise time function is rich enough at high frequencies. In summary, while EGFs are limited by the availability and the quality of earthquake records to be used as the empirical Green's functions, but naturally contain the information regarding the propagation path, PBS require a more detailed information on the velocity structure and are typically limited by more stringent computational time and memory constraints. When dealing with simulations of finite fault earthquakes, both approaches require a source slip distribution model. Note that 3D simulations could also be used to generate synthetic Green's functions in regions where no small events are recorded. Moreover, the sensitivity studies realized by the different simulation techniques are very interesting to quantify the uncertainties related to the variability of the input parameters.

Finally, although the approach adopted in this study to analyse the seismic ground motions produced by the Teil earthquake using two EGF techniques and two physics-based simulation techniques seems interesting, the Le Teil earthquake remains an atypical seismic event in southern France, a region of low-to-moderate seismicity. Thus, this benchmark should be applied to other earthquakes occurred in France. The Epagny/Annecy earthquake (1993) could be a good example for this new study. In fact, the Epagny earthquake presents a large number of similarities with the Le Teil earthquake (shallow earthquake, moderate magnitude, potential induced or triggered earthquake due to a natural hydraulic loading mechanism) and the Meythet earthquake (2013) can serve as a well characterize EGF for the empirical techniques. This small event has a magnitude ( $M_w$ ) of 2.9 and was recorded at the same stations as the Annecy Earthquake. This new analysis will allow to validate the applicability of the empirical techniques in a low-to-moderate seismicity.

Moreover, the two empirical techniques (Irikura recipe and Dujardin method) used in this study share the same simulation concept; however, they lead to different results. These differences in the results should be well investigated in a new comparative analysis to provide some physical explanations to the observed results and understand the importance of because of the assumptions and constraints at the basis of the approaches such as the different summation techniques and the slip velocity functions used in these methods.

At last, the four simulation techniques differently consider local (shallow) site effects. Thus, it will be interesting to isolate the contrast among the simulation techniques from the local shallow site effects by removing the impact of the site effect and then comparing the obtained results for a reference (common) site condition. In addition, additional studies may be done by simulating other earthquakes from the same source, with different magnitude and slip distribution, and/or from other sources in the investigated area, with different distances and azimuths. Also, by using the 3D physics-based simulations, more simulations with and without the sedimentary basin, can be realized to investigate the site effects from different aspects, such as: (i) the variability of the site amplification at specific sites with respect to different outcropping bedrock stations; (ii) the spatial variability of the site amplification within the basin; (iii) the comparison of the 3D amplification function with the results from 1D and 2D simulations; (iv) their repeatability and scenario dependence both in the linear and non-linear domains.

## 7 References

- Aki K. (1967), Scaling law of seismic spectrum, *J. Geophys. res.*, 72, 1217-1231.
- Aki, K. and A. A. Papageorgiou (1988). Separation of source and site effects in acceleration power spectrum of major California earthquakes," in *Proc. Ninth World Conf. Earthq. Eng.*, Vol. 8, 163-167.
- Aki, K., & Richards, P. G. (2002). *Quantitative Seismology*. Sausalito.
- Anderson, J. G. and S. Hough (1984), A model for the shape of the Fourier amplitude spectrum of acceleration at high frequencies, *Bull. Seism. Soc. Am.* 74, 1969-1994, 1984.
- Antonietti PF, Mazzieri I, Quarteroni A, Rapetti F (2012) Non-conforming high order approximations of the elastodynamics equation. *Comput Meth Appl Mech Eng* 209–212:212–238
- Antonietti, P. F., I. Mazzieri, L. Melas, R. Paolucci, A. Quarteroni, C. Smerzini, and M. Stupazzini (2020). Three-dimensional physics based earthquake ground motion simulations for seismic risk assessment in densely populated urban areas, *Math. Eng.* 3,no. 2, 1–31, doi: 10.3934/mine.2021012.
- Campbell, K.W., and Bozorgnia, Y. 2019. Ground motion models for the horizontal components of Arias Intensity (AI) and Cumulative Absolute Velocity (CAV) using the NGA-West2 database. *Earthquake Spectra* 35, 1289-1310.
- Campbell, K.W., and Bozorgnia, Y. 2012. A comparison of ground motion prediction equations for Arias intensity and cumulative absolute velocity developed using a consistent database and functional form. *Earthquake Spectra* 28, 931–941.
- Causse, M., Cornou, C., Maufroy, E., Grasso, J. R., Baillet, L., & El Haber, E. (2021). Exceptional ground motion during the shallow M w 4.9 2019 Le Teil earthquake, France. *Communications Earth & Environment*, 2(1), 1-9.
- Cornou C, Ampuero JP, Aubert C, Audin L, Baize S, Billant J, et al. (2021) Rapid response to the Mw 4.9 earthquake of November 11, 2019 in Le Teil, Lower Rhône Valley, France. *Comptes Rendus. Géoscience, Académie des sciences (Paris)*, 2021, 353 (S1), pp.1-23. ff10.5802/crgeos.30ff. fffhal-03089600v2ff DOI: 10.5802/crgeos.30
- Crempien JGF, Archuleta RJ. (2014). UCSB method for simulation of broadband ground motion from kinematic earthquake sources. *Seismol Res Lett.* 86:61. <https://doi.org/10.1785/0220140103>
- Das S., Kostrov B. V. (1986), Fracture of a single asperity on a finite fault, *Earthq Source Mechanics (Geophysical Monograph 37, Maurice Ewing Series, 6, American Geophysical Union)* pp. 91-96.
- Delouis, B., Ampuero, J. P., Audin, L., Bernard, P., Brenguier, F., Grandin, R., ... & Voisin, C. Rapport d'évaluation du groupe de travail (GT) CNRS-INSU sur le séisme du Teil du 11 novembre 2019 et ses causes possibles, 2019 [http://www.cnrs.fr/sites/default/files/press\\_info/2019-12.Rapport\\_GT\\_Teil\\_phase1\\_final\\_171219\\_v3.pdf](http://www.cnrs.fr/sites/default/files/press_info/2019-12.Rapport_GT_Teil_phase1_final_171219_v3.pdf) (35 p., in french).
- Drouet S., Cotton F., Guégen P. (2010), vS30,  $\kappa$ , regional attenuation and Mw from accelerograms: application to magnitude 3–5 French earthquakes, *Geophys. J. Int.* (2010) 182, 880–898.
- Dujardin, A., Hollender, F., Causse, M., Berge-Thierry, C., Delouis, B., Foundotos, L., ... & Shible, H. (2020). Optimization of a simulation code coupling extended source ( $k-2$ ) and empirical green's functions: Application to the case of the middle durance fault. *Pure and Applied Geophysics*, 177(5), 2255-2279.

- Elmi, S., Busnardo, R., Clavel, B., Camus, G., Kieffer, G., Bérard, P., & Michaëly, B. (1996). Notice explicative, Carte Géologique France 1/50000, feuille Aubenas (865). *Orléans: BRGM*.
- Evangelista, L., S. Del Gaudio, C. Smerzini, A. D'Onofrio, G. Festa, I. Iervolino, L. Landolfi, R. Paolucci, A. Santo, and F. Silvestri (2017). Physics-based seismic input for engineering applications: A case study in the Aterno River valley, Central Italy, *Bull. Earthq. Eng.* 15, no. 7, 2645–2671.
- Faccioli E. (1986). A study of strong motions from Italy and Yugoslavia in terms of gross source properties, in *Earthquake Source Mechanics*, S. Das, J. Boatwright, and C. H. Scholz (Editors), American Geophysical Union Monograph 37, 297-309.
- Faccioli E, Maggio F, Paolucci R, Quarteroni A (1997) 2D and 3D elastic wave propagation by a pseudo-spectral domain decomposition method. *Journal of Seismology*, 1, 237–251
- Fasan, M., 2017. *Advanced seismological and engineering analysis for structural seismic design*. Italy: University of Trieste.
- Fasan, M., Magrin, A., Amadio, C., Romanelli, F., Vaccari, F., and Panza, G. F., 2016. A seismological and engineering perspective on the 2016 Central Italy earthquakes. *International Journal of Earthquake and Impact Engineering*, 1(4), 395–420. DOI: 10.1504/IJEIE.2016.10004076
- Fujiwara H., T. Mikoshiba, and S. Kinoshita (1989). Source parameter of earthquake swarms in the east region of Izu Peninsula, *Prog. Abstr. Seism. Soc. Japan* 2, 128.
- Fujiwara H. and Irikura K. (1991) High-frequency seismic wave radiation from antiplane cohesive zone model and  $f_{max}$  as source effect, *Bull. Seism. Soc. Am.* 81, No. 4, pp. 1115-1128, August 1991.
- Gallovič, F., & Brokešová, J. (2004). On strong ground motion synthesis with  $k=2$  slip distributions. *Journal of Seismology*, 8(2), 211-224.
- Graves RW (1996) Simulating seismic wave propagation in 3D elastic media using staggered-grid finite differences. *Bull Seismol Soc Am* 86:1091–1106
- Guidotti, R., M. Stupazzini, C. Smerzini, R. Paolucci, and P. Ramieri (2011). Numerical study on the role of basin geometry and kinematic seismic source in 3D ground motion simulation of the 22 February 2011 Mw6.2 Christchurch earthquake, *Seismol. Res. Lett.* 82, no. 6, 767–782.
- Gusev, A. A., 2011. Broadband Kinematic Stochastic Simulation of an Earthquake Source: a Refined Procedure for Application in Seismic Hazard Studies. *Pure and Applied Geophysics*, 168(1–2), 155–200. DOI: 10.1007/s00024-010-0156-3
- Hanks, T. C. (1979).  $b$  values and  $\omega-\gamma$  seismic source models: Implications for tectonic stress variations along active crustal fault zones and the estimation of high-frequency strong ground motion. *Journal of Geophysical Research: Solid Earth*, 84(B5), 2235-2242.
- Hanks, T. C., & McGuire, R. K. (1981). The character of high-frequency strong ground motion. *Bulletin of the Seismological Society of America*, 71(6), 2071-2095.
- Hanks, T. C. (1982).  $f_{max}$ , *Bull. Seism. Soc. Am.* 72, 1867-1880.
- Hartzell S. (1978) Earthquake aftershocks as Green's Functions, *Geophysical research letters*, Vol. 5, No. 1.
- Haskell, N. A. (1964) Total energy spectral density of elastic wave radiation from propagating faults, Part I, *Bull. Seism. Soc. Am.* Vol. 54, 1811-1841
- Haskell, N. A. (1966) Total energy spectral density of elastic wave radiation from propagating faults, Simulation Techniques benchmark, the test case of the November 11, 2019 Mw4.9 Le Teil earthquake

Part II, Bull. Seism. Soc. Am. Vol. 56, 125-140

- Hassan, H. M., Fasan, M., Sayed, M. A., Romanelli, F., ElGabry, M. N., Vaccari, F., and Hamed, A., 2020. Site-specific ground motion modeling for a historical Cairo site as a step towards computation of seismic input at cultural heritage sites. *Engineering Geology*, **268**(April 2019), 105524. Elsevier. DOI: 10.1016/j.enggeo.2020.105524
- The Headquarters for Earthquake Research Promotion (2017) Strong ground motion prediction method for earthquakes with specified source faults ("Recipe"), April 2017. (in Japanese)
- Heaton, T. H., 1990. Evidence for and implications of self-healing pulses of slip in earthquake rupture. *Physics of the Earth and Planetary Interiors*, **64**(1), 1–20. DOI: 10.1016/0031-9201(90)90002-F
- Herrero, A., & Bernard, P. (1994). A kinematic self-similar rupture process for earthquakes. *Bulletin of the Seismological Society of America*, **84**(4), 1216-1228.
- Hisada, Y. (2001). A theoretical omega-square model considering spatial variation in slip and rupture velocity. Part 2: Case for a two-dimensional source model. *Bulletin of the Seismological Society of America*, **91**(4), 651-666.
- Hisada Y, Bielak J (2003). A Theoretical Method for Computing Near-Fault ground Motions in Layered Half-Spaces Considering Static Offset Due to Surface Faulting, with a Physical Interpretation of Fling Step and Rupture Directivity, *Bulletin of the Seismological Society of America*, **93**(3), 1154-1168
- Infantino, M., I. Mazzieri, A. G. Özcebe, R. Paolucci, and M. Stupazzini (2021). 3D physics-based numerical simulations of ground motion in Istanbul from earthquakes along the Marmara segment of the north Anatolian fault, *Bull. Seismol. Soc. Am.* **110**, no. 6, 2559–2576, doi: 10.1785/0120190235
- Irikura K. (1983) Semi-Empirical Estimation of Strong Ground Motions during large earthquakes, *Bull. Disas. Prev. Res. Inst., Kyoto Univ.*, Vol. 33, Part 2, No.298.
- Irikura K. (1986) Prediction of strong acceleration motions using empirical Green's Function. *Proceedings of the 7th Japan Earthq. Eng symposium.*
- Irikura K., Kagawa T., and Sekiguchi H. (1997) Revision of the empirical Green's function method, *Seismological Society of Japan*, Vol. 2.
- Irikura K., Miyake H. (2011) Recipe for predicting strong ground motion from crustal earthquake scenarios, *Pure Appl. Geophys*, DOI: 10.1007/s00024-010-0150-9.
- Jomard, H., Cushing, E. M., Palumbo, L., Baize, S., David, C., & Chartier, T. (2017). Transposing an active fault database into a seismic hazard fault model for nuclear facilities—Part 1: Building a database of potentially active faults (BDFa) for metropolitan France. *Natural Hazards and Earth System Sciences*, **17**(9), 1573-1584.
- Kanamori H., Anderson L. (1975) Theoretical basis of some empirical relations in seismology, *Bull. Seismol. Soc. Am.*, Vol. 65, No. 5, pp. 1073-1095.
- Komatitsch D, Vilotte JP (1998) The spectral-element method: an efficient tool to simulate the seismic response of 2D and 3D geological structures. *Bull Seismol Soc Am* **88**:368–392
- Konno, K., & Ohmachi, T. (1998). Ground-motion characteristics estimated from spectral ratio between horizontal and vertical components of microtremor. *Bulletin of the Seismological Society of America*, **88**(1), 228-241.

- Madariaga R. (1979) On the relation between seismic moment and stress drop in the presence of stress and strength heterogeneity, *Journal of geophysical research*, Vol. 84, No. B5.
- Magrin, A., 2012. *Multi-scale seismic hazard scenarios*. Italy: University of Trieste.
- Magrin, A., Gusev, A. A., Romanelli, F., Vaccari, F., and Panza, G. F., 2016. Broadband NDSHA computations and earthquake ground motion observations for the Italian territory. *International Journal of Earthquake and Impact Engineering*, **1**(1/2), 28. DOI: 10.1504/IJEIE.2016.10000979
- Mazzieri, I, Stupazzini M, Guidotti R, Smerzini C (2013) SPEED: SPectral Elements in Elastodynamics with Discontinuous Galerkin: a non-conforming approach for 3D multi-scale problems. *Int J Numer Meth Eng* 95(12):991–1010.
- Miyake H., Iwata T., and Irikura, K. (2001), Estimation of rupture propagation direction and strong motion generation area from azimuth and distance dependence of source amplitude spectra, *Geophys Res Lett* 28, 2727–2730.
- Miyake H., Iwata T., Irikura K. (2003), Source characterization for broadband ground-motion simulation: kinematic heterogeneous source model and strong motion generation area. *Bull. Seism. Soc. Am.*, Vol. 93, No. 6, pp 2531-2545.
- Özcebe, A. G., C. Smerzini, R. Paolucci, H. Pourshayegan, R. Rodríguez Plata, C. G. Lai, E. Zuccolo, F. Bozzoni, and M. Villani (2019). On the comparison of 3D, 2D, and 1D numerical approaches to predict seismic site amplification: The case of Norcia basin during the M6.5 2016 October 30 earthquake, *Proc. of the 7th International Conference on Earthquake Geotechnical Engineering*, Rome, Italy, 17–20 June
- Panza, G. F., 2001. SEISMIC WAVE PROPAGATION IN LATERALLY HETEROGENEOUS ANELASTIC MEDIA: THEORY AND APPLICATIONS TO SEISMIC ZONATION Giuliano. *Advances in Geophysics*, **43**, 1–95.
- Panza, G. F., Mura, C. La, Peresan, A., Romanelli, F., and Vaccari, F., 2012. Seismic Hazard Scenarios as Preventive Tools for a Disaster Resilient Society (pp. 93–165). DOI: 10.1016/B978-0-12-380938-4.00003-3
- Paolucci, R, Mazzieri I, Smerzini C (2015). Anatomy of strong ground motion: near-source records and three-dimensional physics-based numerical simulations of the Mw 6.0 2012 May 29 Po Plain earthquake, Italy. *Geophysical Journal International*, 203(3):2001–2020
- Paolucci, R., L. Evangelista, I. Mazzieri, and E. Schiappapietra (2016). The 3D numerical simulation of near-source ground motion during the Marsica earthquake, central Italy, 100 years later, *Soil Dynam. Earthq. Eng.* 91, 39–52.
- Paolucci R, Gatti F, Infantino M, Smerzini C, Özcebe AG, Stupazzini M (2018). Broadband Ground Motions from 3D Physics-Based Numerical Simulations Using Artificial Neural Networks. *Bull Seismol Soc Am*, 108, 1272-1286.
- Paolucci, R., I. Mazzieri, G. Piu'no, C. Smerzini, M. Vanini, and A. G. Özcebe (2021a). Earthquake ground motion modelling of induced seismicity in the Groningen gas field, *Earthq. Eng. Struct. Dynam.* 50, 135–154, doi: 10.1002/eqe.3367.
- Paolucci, R., C. Smerzini, and M. Vanini (2021b). BB-SPEEDset: A Validated Dataset of Broadband Near-Source Earthquake Ground Motions from 3D Physics-Based Numerical Simulations, *Bull. Seismol. Soc. Am.* XX, 1–19, doi: 10.1785/0120210089
- Pavlov, V. M., 2009. Matrix impedance in the problem of the calculation of synthetic seismograms for a layered-homogeneous isotropic elastic medium. *Izvestiya, Physics of the Solid Earth*, **45**(10), 850–860. DOI: 10.1134/S1069351309100036

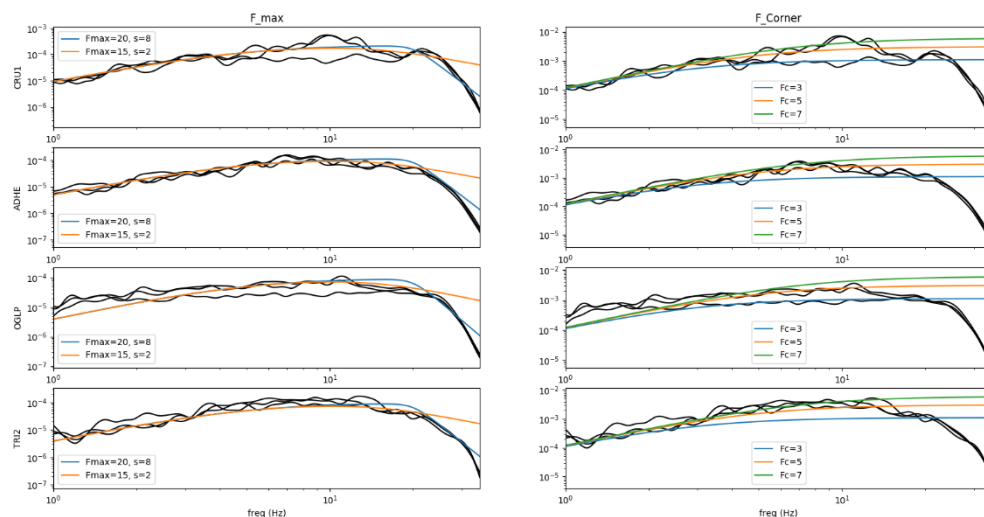
- Pilz, M., S. Parolai, M. Stupazzini, R. Paolucci, and J. Zschau (2011). Modelling basin effects on earthquake ground motion in the Santiago de Chile basin by a spectral element code, *Geophys. J. Int.* 187, 929–945, doi: 10.1111/j.1365-246X.2011.05183.x
- Pitarka, A., Somerville, P., Fukushima, Y., Uetake, T., & Irikura, K. (2000). Simulation of near-fault strong-ground motion using hybrid Green's functions. *Bulletin of the Seismological Society of America*, 90(3), 566-586.
- Ritz, J. F., Baize, S., Ferry, M., Larroque, C., Audin, L., Delouis, B., & Mathot, E. (2020). Surface rupture and shallow fault reactivation during the 2019 Mw 4.9 Le Teil earthquake, France. *Communications Earth & Environment*, 1(1), 1-11.
- Sangaraju, S., R. Paolucci, and C. Smerzini (2021). 3D physics-based ground motion simulation of the 2016 Kumamoto earthquakes, Proc. of the 6th IASPEI/IAEE International Symposium: The Effects of Surface Geology on Seismic Motion (ESG6), Kyoto, Japan, August 2021
- Sato Tonomi, Kawase H., Sato Toshiaki (1994), 表層地盤の影響を取り除いた工学的基盤波の統計的スペクトル特性, 仙台地域のボアホールで観測された多数の中小地震記録を用いた解析, 日本建築学会構造系論文集, 462, 79-89.
- Schmedes, J., R. J. Archuleta, and D. Lavallée (2012). A kinematic rupture model generator incorporating spatial interdependency of earthquake source parameters, *Geophys. J. Int.* 192, 1116–1131
- SIGMA-2013-D2-072: Pacor F., 2013. CALIBRATION OF GMPEs FOR PO PLAIN REGION.
- SIGMA2-2018-D3-015 : Paolucci R., Smerzini C., Mazzieri I., Özcebe A.G., Infantino M., 2018. Progress report on 3D physics-based numerical approaches for earthquake ground motion prediction.
- SIGMA2-2020-D3-051: Bahrapouri M. and Rodriguez-Marek A., 2020. Quantification of Uncertainties for Conducting Non-Ergodic PSHA.
- Sira C. et al. Rapport macrosismique n°4, Séisme du Teil (Ardèche) 11 novembre 2019 à 11 h 52 locale, Magnitude 5,2 ML (RENASS), Intensité communale max VII-VIII (EMS98), BCSF-RENASS-2020-R2. <https://doi.org/10.13140/RG.2.2.27570.84166> (2020).
- Smerzini, C. (2010). The earthquake source in numerical modeling of seismic wave propagation in heterogeneous Earth media, Ph.D. Thesis, University School for Advanced Studies in Pavia.
- Smerzini, C., R. Paolucci, and M. Stupazzini (2011). Comparison of 3D, 2D and 1D numerical approaches to predict long period earthquake ground motion in the Gubbio plain, Central Italy, *Bull. Earthq. Eng.* 9, no. 6, 2007–2029.
- Smerzini, C. (2018). Spatial variability of earthquake ground motion from 3D physics-based numerical simulations, in Proc. of the 16<sup>th</sup> European Conference on Earthquake Engineering, Thessaloniki, Greece, 18–21 June.
- Smerzini, C., K. Pitilakis, and K. Hashemi (2017). Evaluation of earthquake ground motion and site effects in the Thessaloniki urban area by 3D finite-fault numerical simulations, *Bull. Earthq. Eng.* 15, no. 3, 787–812.
- Smerzini, C., and K. Pitilakis (2018). Seismic risk assessment at urban scale from 3D physics-based numerical modeling: The case of Thessaloniki, *Bull. Earthq. Eng.* 16, no. 7, 2609–2631.
- Smerzini, C., and M. Villani (2012). Broadband numerical simulations in complex near-field geological configurations: The case of the 2009 Mw 6.3 L'Aquila earthquake, *Bull. Seismol. Soc. Am.* 102, no. 6, 2436–2451.

- Somerville, P., Irikura, K., Graves, R., Sawada, S., Wald, D., Abrahamson, N., ... & Kowada, A. (1999). Characterizing crustal earthquake slip models for the prediction of strong ground motion. *Seismological Research Letters*, 70(1), 59-80.
- Stupazzini, M, Paolucci R, Igel H (2009) Near-Fault Earthquake Ground-Motion Simulation in the Grenoble Valley by a High-Performance Spectral Element Code," *Bull. Seismol. Soc. Am.*, 99(1): 286–301.
- Stupazzini, M., M. Infantino, A. Allmann, and R. Paolucci (2021). Physics-based probabilistic seismic hazard and loss assessment in large urban areas: A simplified application to Istanbul, *Earthq. Eng. Struct. Dynam.* 50, 99–115, doi: 10.1002/eqe.3365
- Tsurugi M., Kagawa K., Irikura K., Furuwada A. (1997), 近畿地方で発生する地震のfmaxに関する基礎的検討, 地球惑星科学関連学会合同大会予稿集, 103.
- Umeda, Y., Y. Iio, A. Kuroiso, K. Ito, and H. Murakami (1984). Scaling of observed seismic spectra, *J. Seism. Soc. Japan (Zisin)* 37, 559-568 (in Japanese).
- Villani, M., E. Faccioli, M. Ordaz, and M. Stupazzini (2014). Highresolution seismic hazard analysis in a complex geological configuration: The case of the Sulmona basin in Central Italy, *Earthq. Spectra* 30, no. 4, 1801–1824.
- Wells, D. L., and Coppersmith, K. J., 1994. New empirical relationships among magnitude, rupture length, rupture width, rupture area, and surface displacement. *Bulletin - Seismological Society of America*, 84(4), 974–1002.

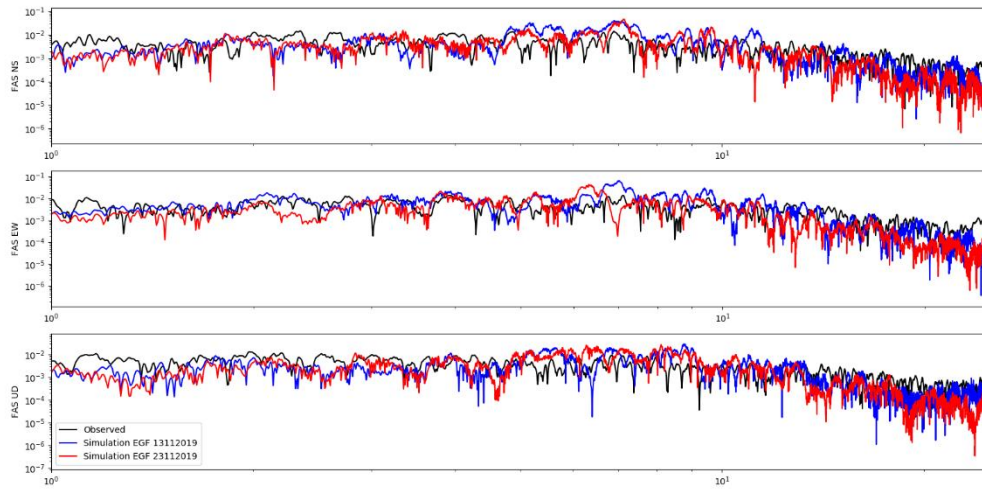
## 8 Appendixes

### 8.1 Appendix 1: Irikura recipe

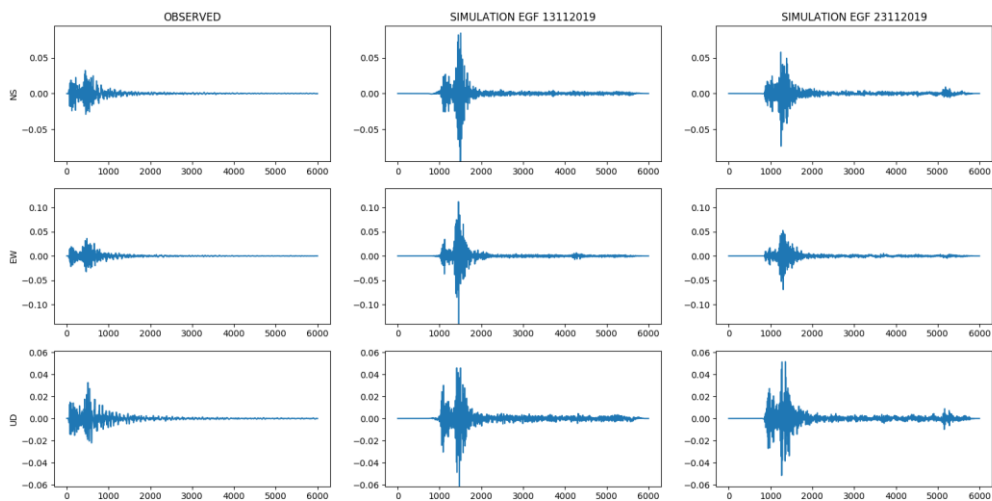
EGF parameters for 2019\_11\_13\_144240


 Determination of  $F_c$  and  $F_{max}$  for EGF\_13112019

ADHE

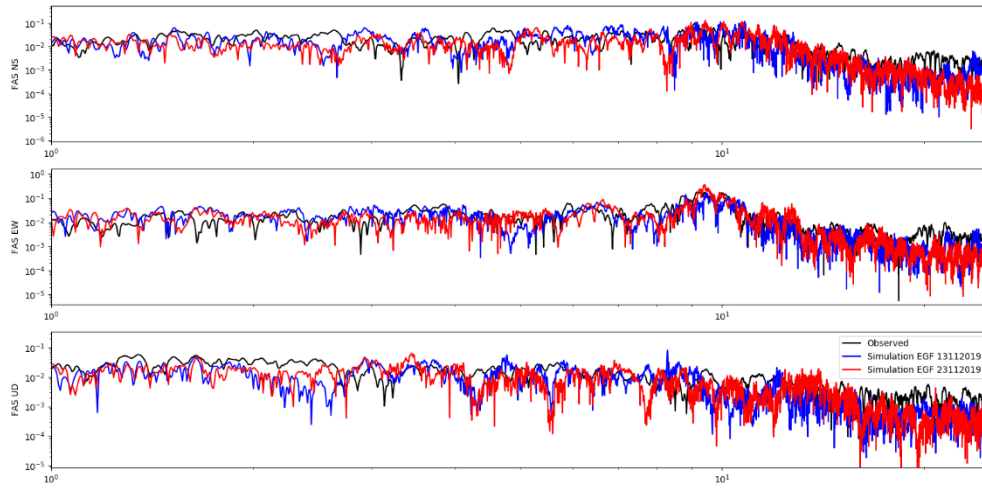


ADHE

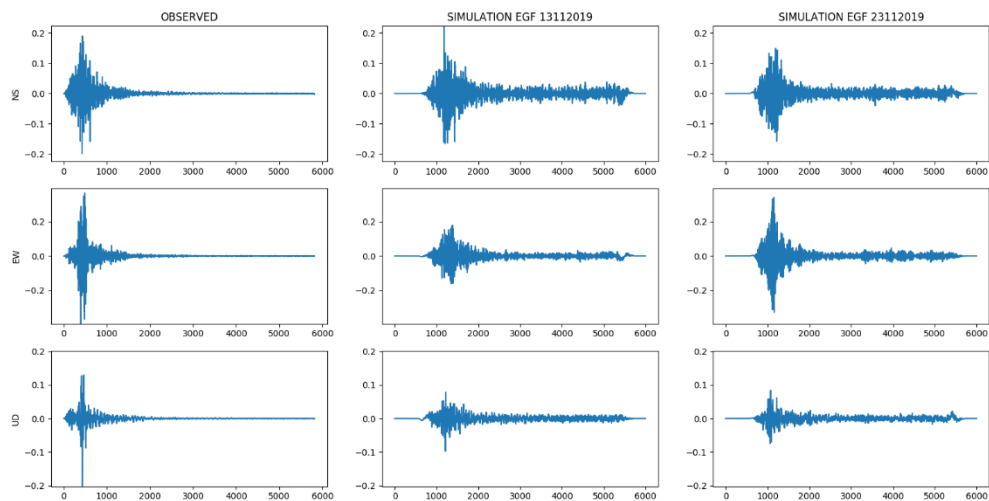


*Comparison for FAS and waveforms between simulations and observed data at station ADHE*

CRU1

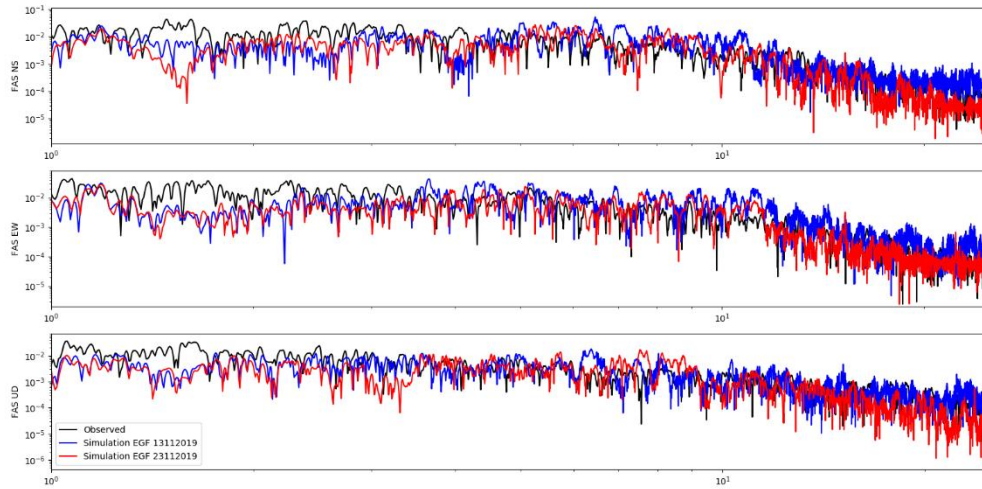


CRU1

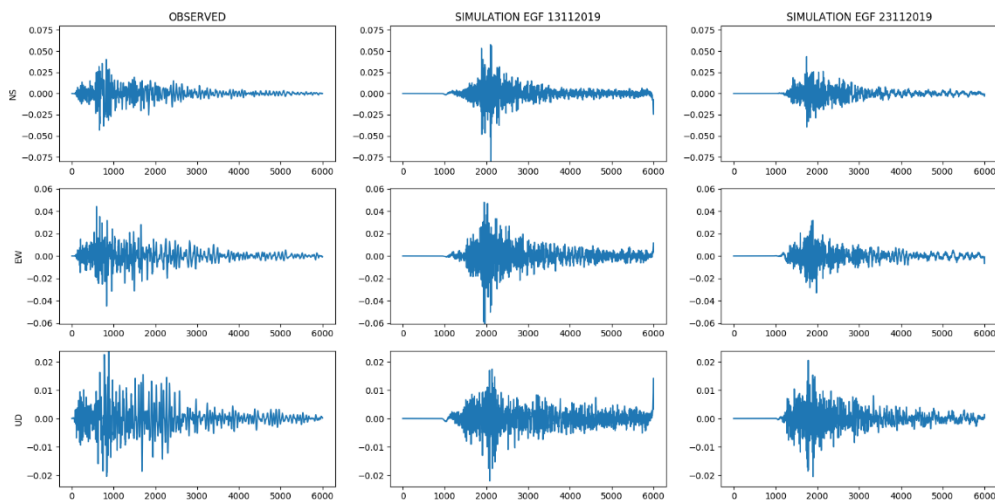


*Comparison for FAS and waveforms between simulations and observed data at station CRU1*

OGLP

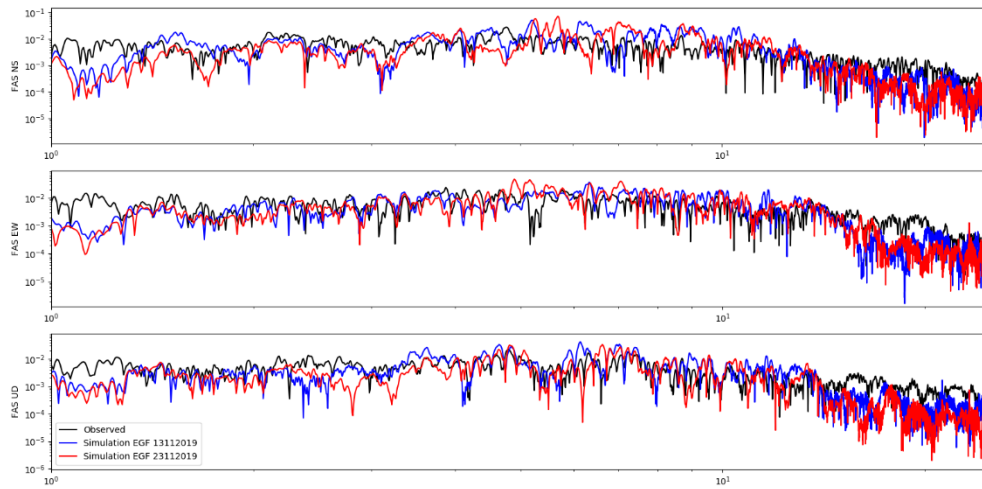


OGLP

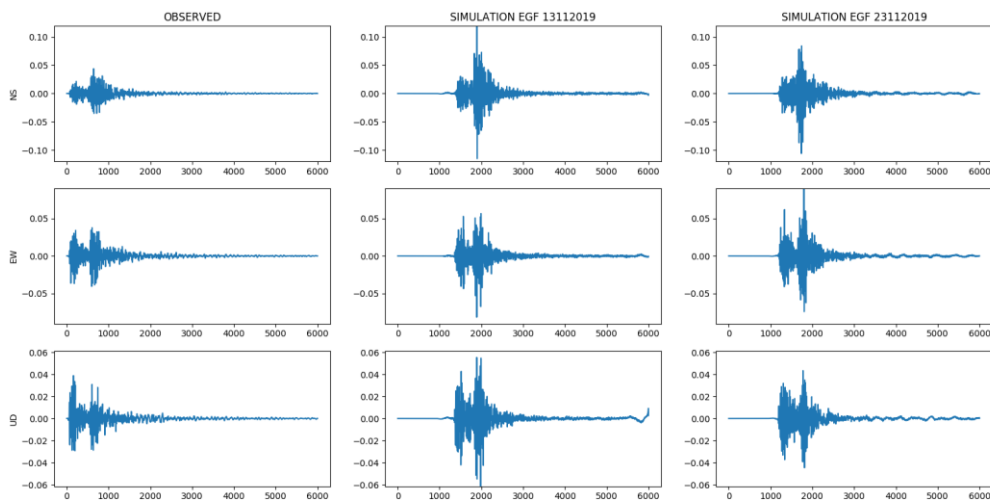


*Comparison for FAS and waveforms between simulations and observed data at station OGLP*

TRI2



TRI2



*Comparison for FAS and waveforms between simulations and observed data at station TRI2*

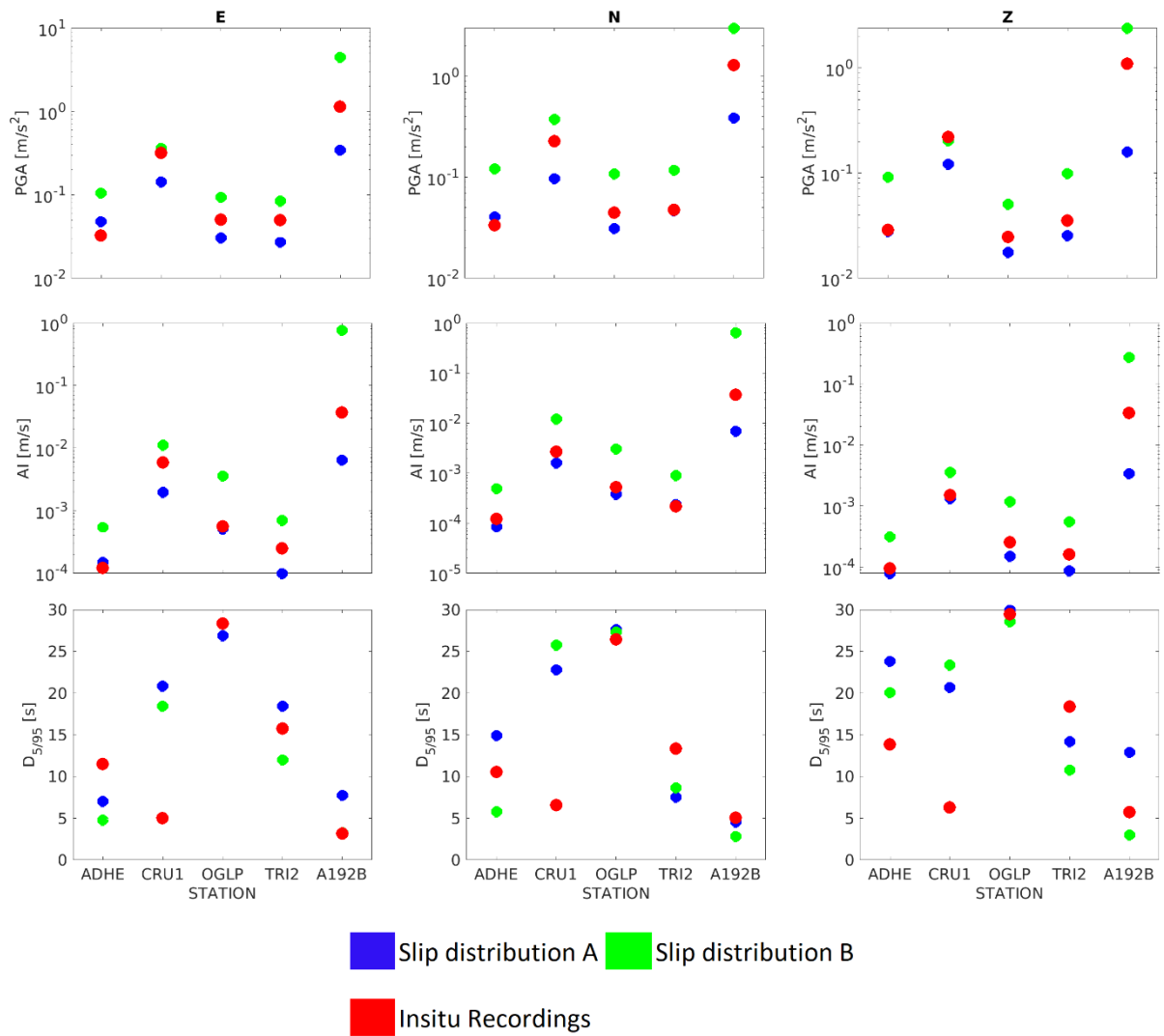
	ADHE		CRU1		OGLP		TRI2	
	131119	231119	131119	231119	131119	231119	131119	231119
<b>GOF_PGA</b>	0.44	0.28	-0.2	-0.18	0.12	-0.06	0.31	0.26
<b>GOF_FAS</b>	-1	-1.39	-1.2	-1.43	0.6	0.13	-0.004	-0.33
<b>GOF_PSA</b>	0.37	0.24	-0.08	-0.09	-0.02	-0.18	0.32	0.26

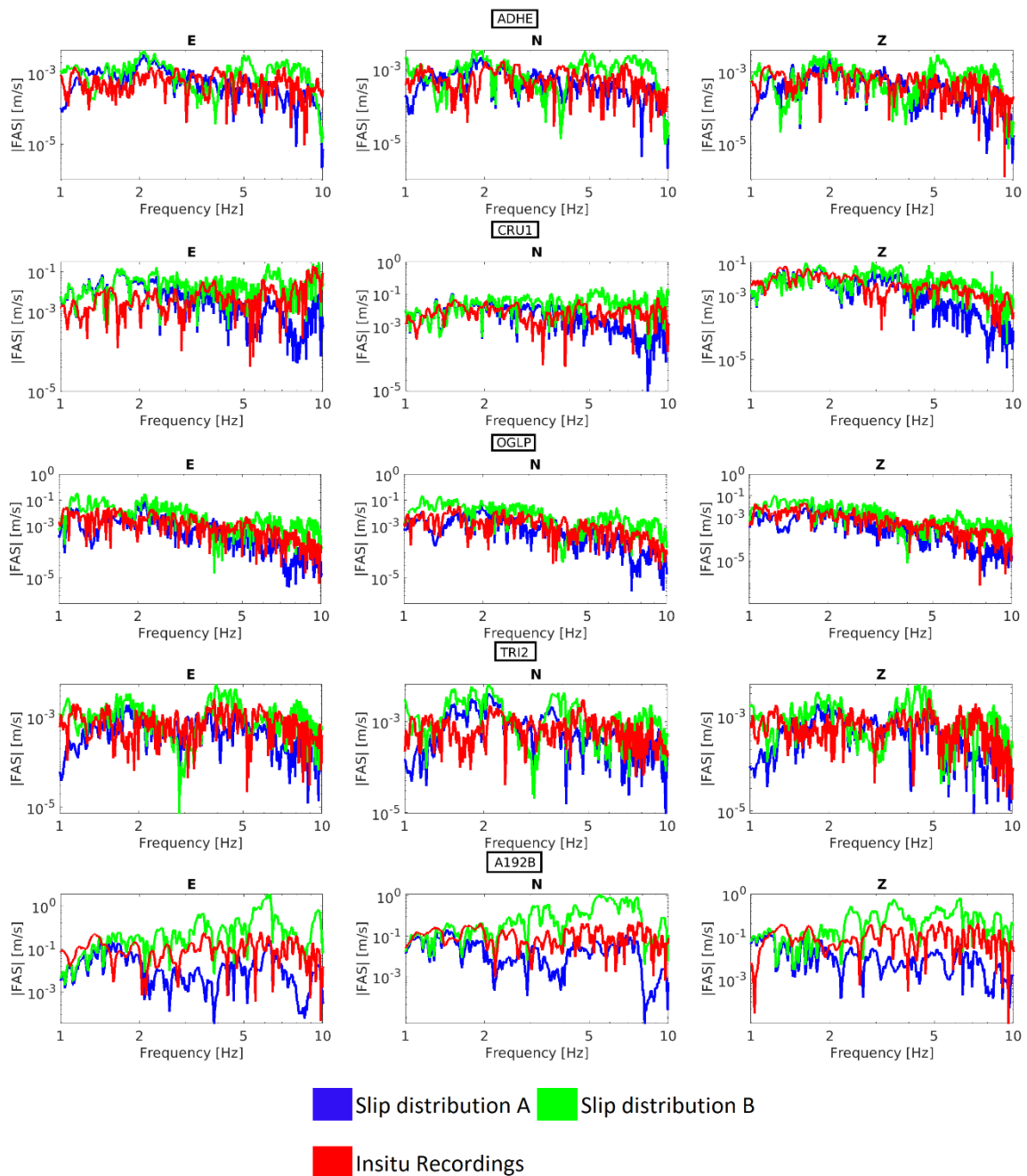
*GOF for each criteria PGA, FAS, PSA averaged on the 3 components, for each station and for both EGF*

EGF	GOF_PGA	GOF_FAS	GOF_PSA	TOTAL
<b>131119</b>	0.28	0.74	0.23	0.418
<b>231119</b>	0.2	0.84	0.21	0.417

*GOF for each criteria PGA, FAS and PSA averaged on the 3 components and on all stations, for both EGF*

## 8.2 Appendix 2: Dujardin modified method

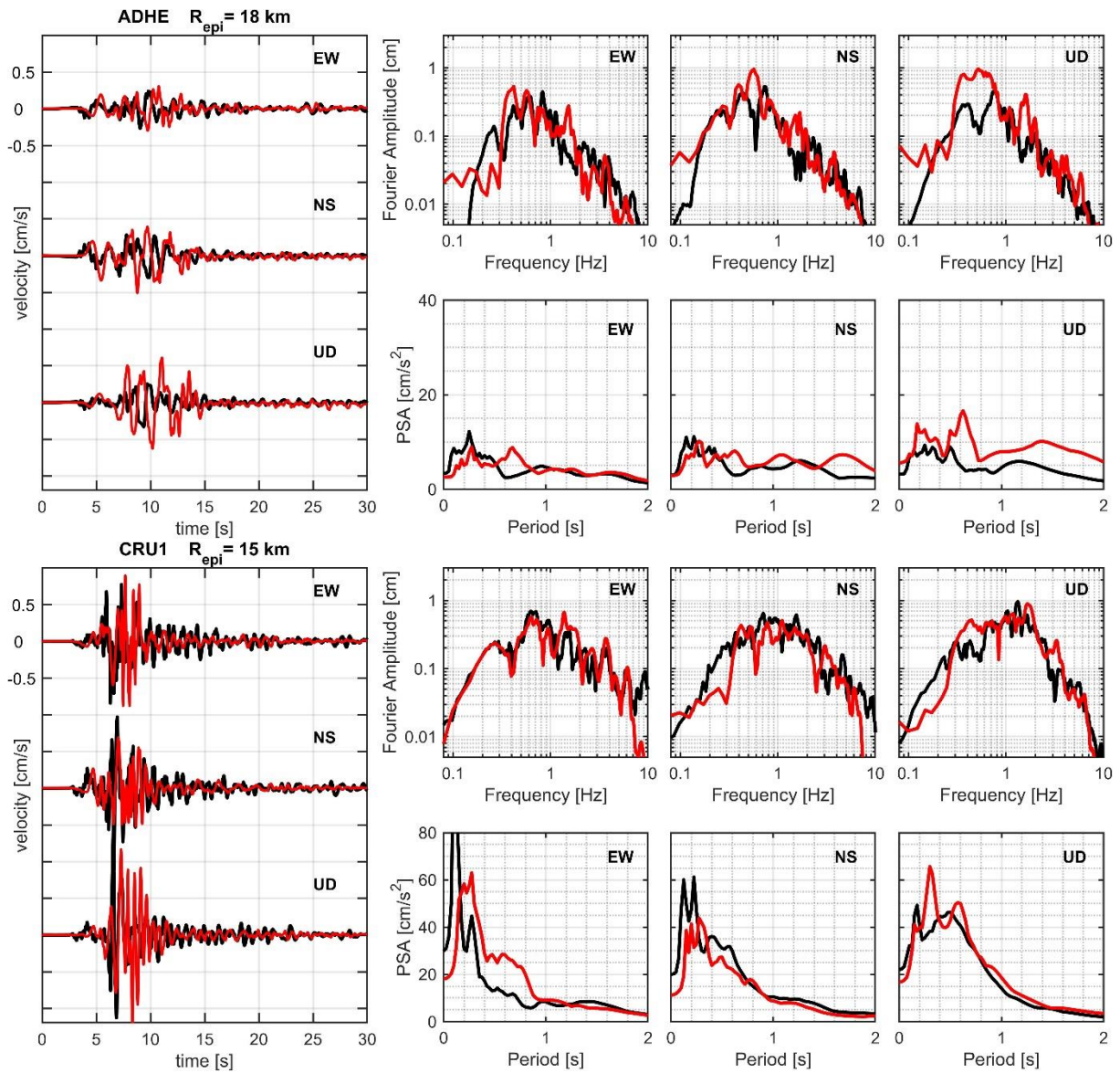


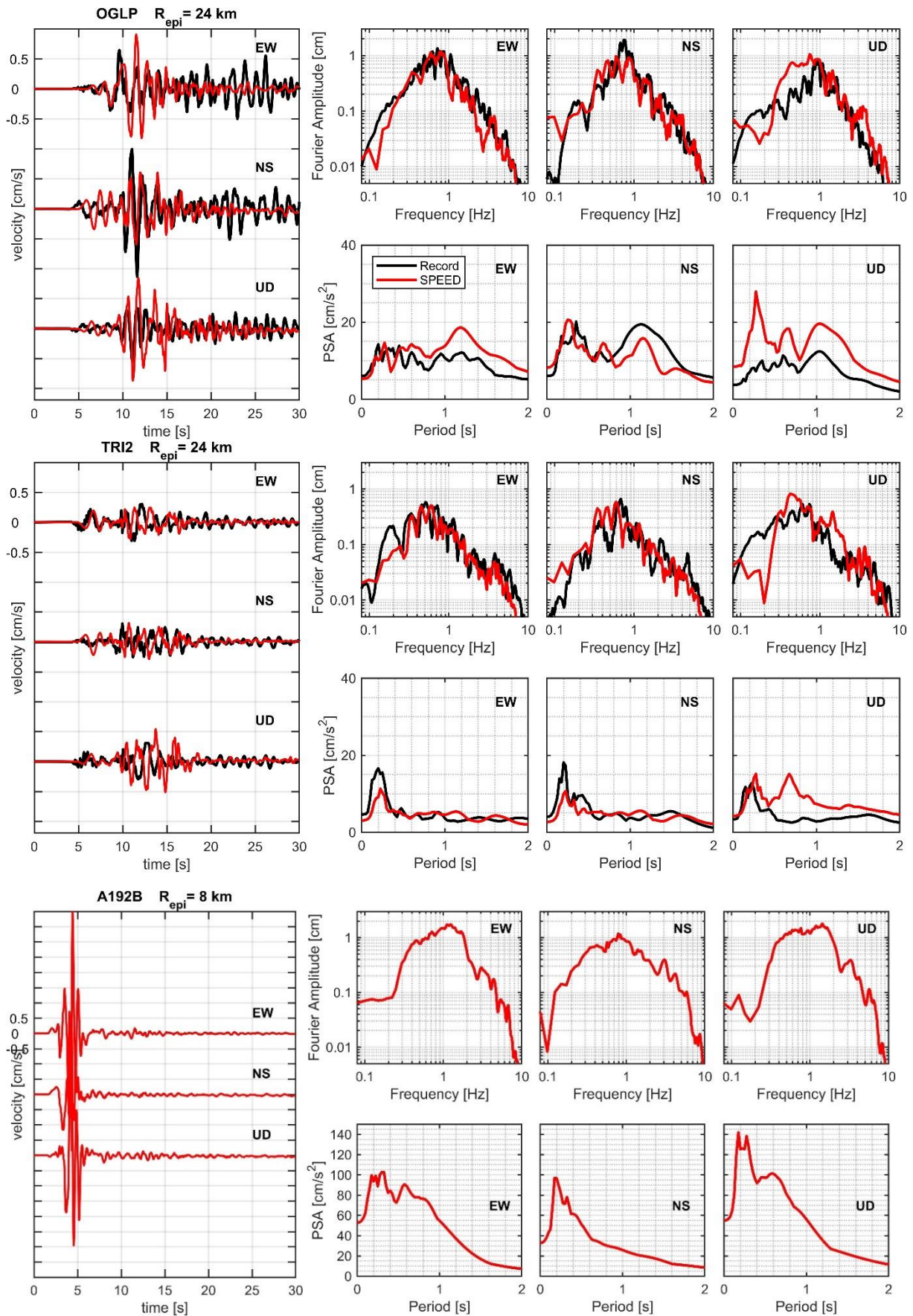


### 8.3 Appendix 3: 3D simulations

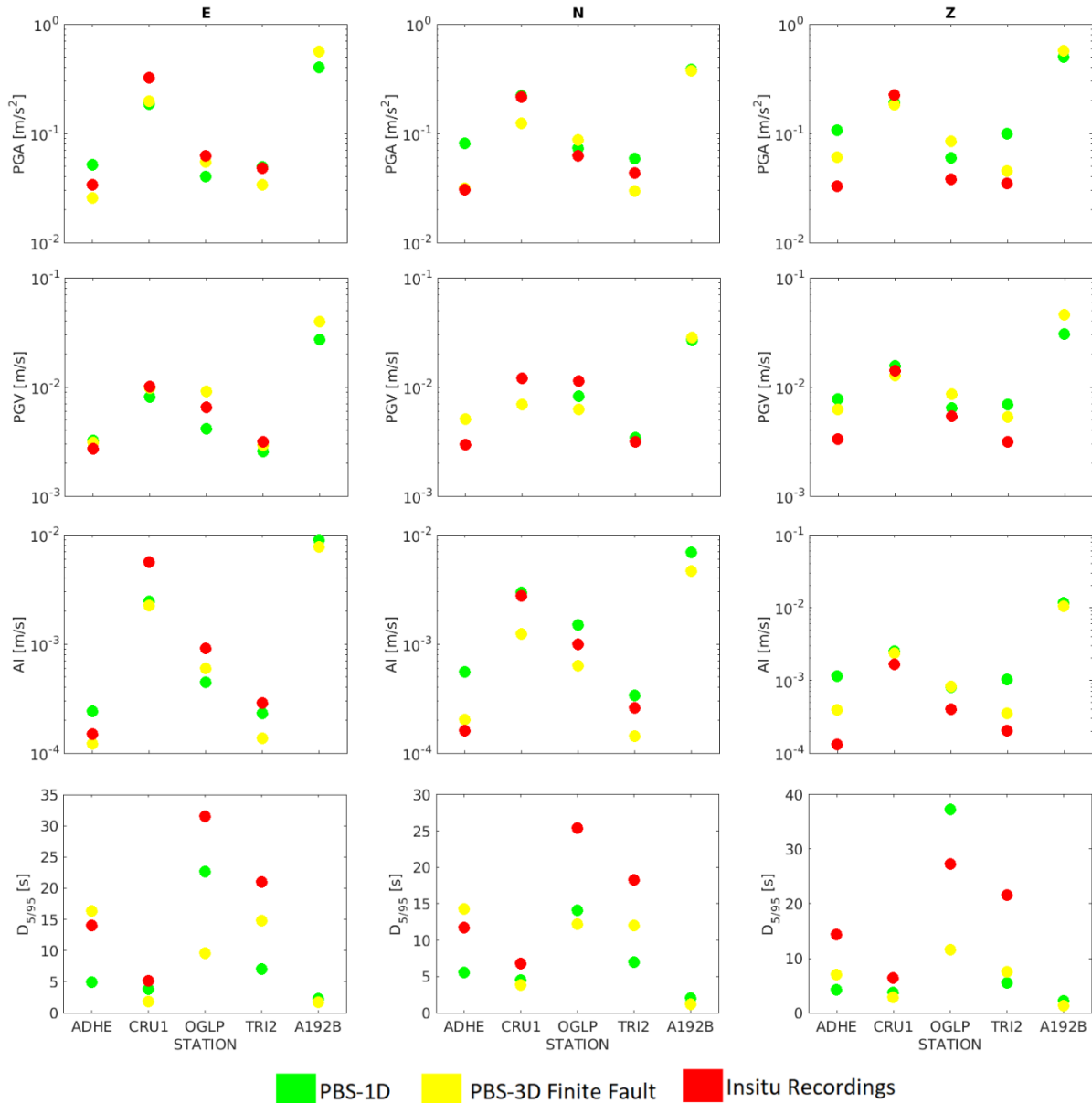
#### Results of 3D simulations (POLIMI)

In the following, results of numerical simulations are shown for all selected stations, in terms of velocity time histories, Fourier and Response Spectra.





### 8.4 Appendix 4: Comparison of simulation techniques between 0 and 10 Hz

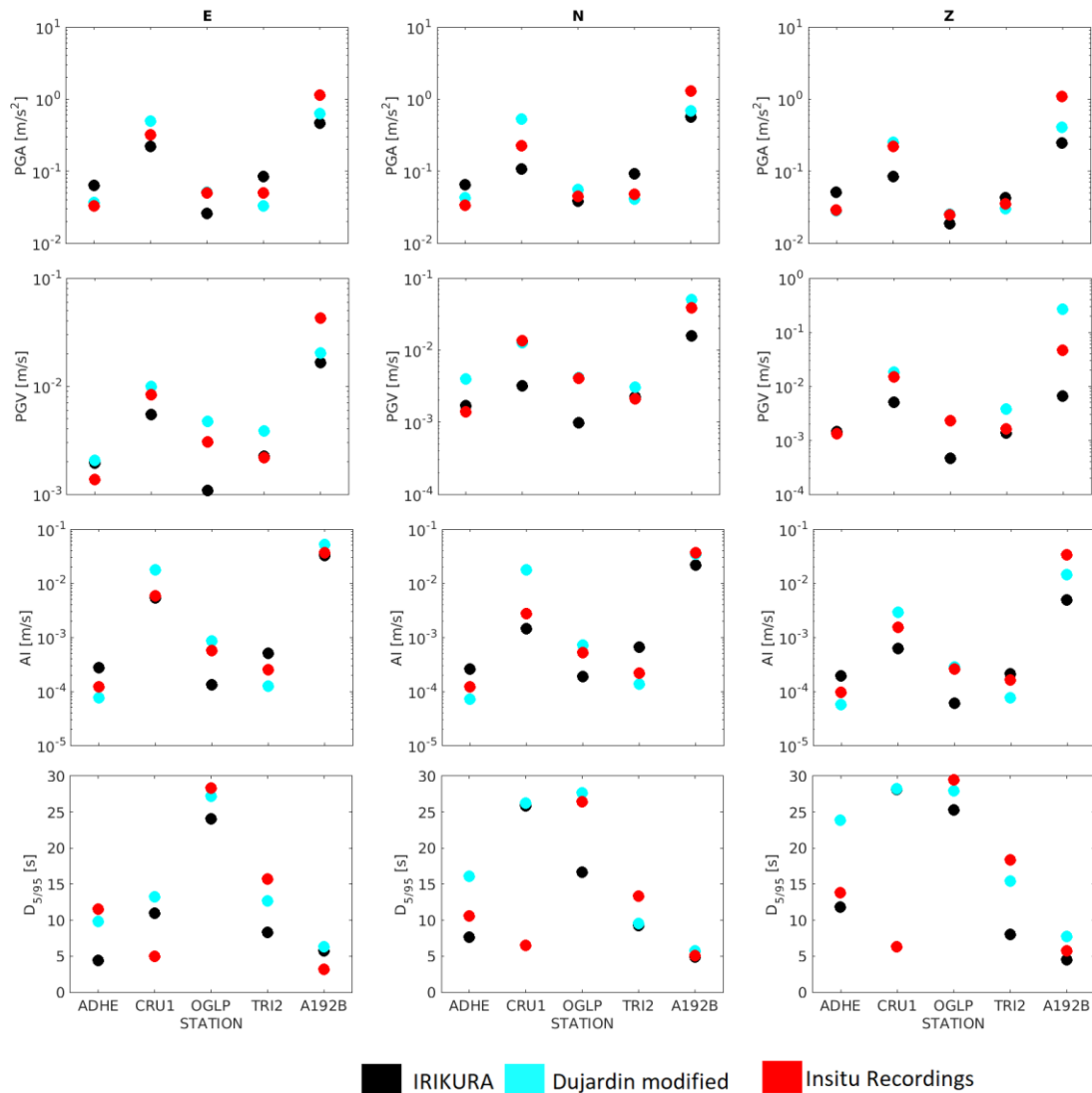


The ground motion intensity measures (PGA, PGV, Arias Intensity and Duration) calculated within a frequency range between 0 and 10 Hz, by using the two PBS's techniques (PBS-1D in green and PBS-3D with finite fault in yellow) for the three components of the five stations (ADHE, CRU1, OGLP, TRI2 and A192B). The red color corresponds to the FAS calculated for the recorded accelerograms.

For a frequency range between 0 and 10 Hz, the Misfit between simulated and recorded accelerograms calculated for the five ground motion intensity measures (PGA, PGV, Arias Intensity, Duration and FAS) estimated by using the five simulation's techniques. The results are sorted by station and by calculation direction.

Goodness of Fit (Anderson, 2004)						
GM Indicator	Station	Direction	Simulation's technique			
			Irikura	Dujardin Modified	PBS 1D	PBS 3D Finite Fault
PGA	ADHE	E			0.1835	-0.1220
		N			0.4271	0.0155
		Z			0.5138	0.2661
	CRU1	E			-0.2422	-0.2156
		N			0.0134	-0.2430
		Z			-0.0675	-0.0881
	OGLP	E			-0.1874	-0.0573
		N			0.0755	0.1468
		Z			0.1964	0.3502
	TRI2	E			0.0137	-0.1557
		N			0.1338	-0.1635
		Z			0.4545	0.1139
PGV	ADHE	E			0.0743	0.0581
		N			0.2315	0.2317
		Z			0.3697	0.2723
	CRU1	E			-0.0991	-0.0162
		N			0.0026	-0.2387
		Z			0.0414	-0.0487
	OGLP	E			-0.1966	0.1509
		N			-0.1392	-0.2605
		Z			0.0728	0.1995
	TRI2	E			-0.0896	-0.0352
		N			0.0344	-0.0039
		Z			0.3456	0.2323
AI	ADHE	E			0.2115	-0.0844
		N			0.5376	0.0982
		Z			0.9375	0.4750
	CRU1	E			-0.3627	-0.3983
		N			0.0368	-0.3466
		Z			0.1796	0.1502
	OGLP	E			-0.3110	-0.1852
		N			0.1723	-0.2018
		Z			0.3033	0.3152
	TRI2	E			-0.0985	-0.3256
		N			0.1161	-0.2612
		Z			0.7087	0.2421
D95	ADHE	E			-0.4492	0.0656
		N			-0.3281	0.0844
		Z			-0.5303	-0.3112
	CRU1	E			-0.1312	-0.4482
		N			-0.1745	-0.2469
		Z			-0.2296	-0.3457
	OGLP	E			-0.1435	-0.5180
		N			-0.2546	-0.3183
		Z			0.1361	-0.3718
	TRI2	E			-0.4769	-0.1502
		N			-0.4168	-0.1807
		Z			-0.5987	-0.4569
FAS	ADHE	E			0.1213	-0.1563
		N			0.3272	-0.0080
		Z			0.5567	0.1526
	CRU1	E			-0.1247	-0.2439
		N			-0.0213	-0.3202
		Z			0.1044	-0.0397
	OGLP	E			-0.1833	-0.0485
		N			0.1775	0.0328
		Z			0.3105	0.3269
	TRI2	E			-0.0261	-0.2220
		N			0.1101	-0.1610
		Z			0.3945	0.0381

### 8.5 Appendix 5: Comparison of simulations by using the slip distribution B (see section 3.2.2 for details)



The ground motion intensity measures (PGA, PGV, Arias Intensity and Duration) calculated within a frequency range between 1 and 10 Hz, by using the two empirical simulation's techniques (Irikura in black, Dujardin modified in cyan) for the three components of the five stations (ADHE, CRU1, OGLP, TRI2 and A192B). The red color corresponds to the FAS calculated for the recorded accelerograms.

For a frequency range between 1 and 10 Hz and the slip distribution B, the Misfit between simulated and recorded accelerograms calculated for the five ground motion intensity measures (PGA, PGV, Arias Intensity, Duration and FAS) estimated by using the five simulation's techniques. The results are sorted by station and by calculation direction.

Goodness of Fit						
GM Indicator	Station	Direction	Simulation's technique			
			Irikura	Dujardin	Modified	PBS - 1D
PGA	ADHE	E	0.2880		0.0531	
		N	0.2909		0.1084	
		Z	0.2473		-0.0139	
	CRU1	E	-0.1565		0.1872	
		N	-0.3303		0.3668	
		Z	-0.4175		0.0569	
	OGLP	E	-0.2852		0.0061	
		N	-0.0617		0.0988	
		Z	-0.1180		0.0149	
	TRI2	E	0.2350		-0.1771	
		N	0.2857		-0.0623	
		Z	0.0794		-0.0731	
PGV	ADHE	E	0.1558		0.1762	
		N	0.0857		0.4525	
		Z	0.0368		0.0026	
	CRU1	E	-0.1844		0.0762	
		N	-0.6292		-0.0267	
		Z	-0.4603		0.0968	
	OGLP	E	-0.4512		0.1882	
		N	-0.6147		0.0105	
		Z	-0.6995		-0.0034	
	TRI2	E	0.0101		0.2444	
		N	0.0296		0.1580	
		Z	-0.0808		0.3732	
AI	ADHE	E	0.3520		-0.2063	
		N	0.3278		-0.2321	
		Z	0.3099		-0.2245	
	CRU1	E	-0.0380		0.4848	
		N	-0.2778		0.8134	
		Z	-0.3897		0.2824	
	OGLP	E	-0.6236		0.1859	
		N	-0.4430		0.1352	
		Z	-0.6222		0.0388	
	TRI2	E	0.3040		-0.2965	
		N	0.4843		-0.2067	
		Z	0.1182		-0.3304	
D95	ADHE	E	-0.4114		-0.0681	
		N	-0.1419		0.1838	
		Z	-0.0671		0.2374	
	CRU1	E	0.3407		0.4228	
		N	0.5961		0.6034	
		Z	0.6508		0.6521	
	OGLP	E	-0.0721		-0.0181	
		N	-0.2003		0.0197	
		Z	-0.0659		-0.0230	
	TRI2	E	-0.2777		-0.0952	
		N	-0.1593		-0.1459	
		Z	-0.3588		-0.0765	
FAS	ADHE	E	0.0225		-0.2181	
		N	0.0712		-0.1967	
		Z	0.0693		-0.2153	
	CRU1	E	-0.1363		0.2115	
		N	-0.2141		0.2962	
		Z	-0.1648		0.1803	
	OGLP	E	-0.1138		0.0514	
		N	-0.0996		0.0396	
		Z	-0.0693		-0.0315	
	TRI2	E	0.0050		-0.2354	
		N	0.0464		-0.2244	
		Z	-0.0934		-0.2742	